A Szilikátipari Tudományos Egyesület lapja

építőanyag

Journal of Silicate Based and Composite Materials

A TARTALOMBÓL:

2018/6


TUNGSRAM
Innovation is our heritage
EST.1896
INNOVATUNGSRAM
Tungsram returns to the market as an innovative, premium brand with design, development and manufacturing in Europe and a commitment to continue and expand its outreach.
tungsram.com

építőanyag
Journal of Silicate Based and Composite Materials
2018/6

TARTALOM

CONTENT

A finomkerámia-, üveg-, cement-, mész-, beton-, tégla- és cserép-, kő- és kavics-, tűzállóanyag-, szigetelőanyag-iparágak szakmai lapja
Scientific journal of ceramics, glass, cement, concrete, clay products, stone and gravel, insulating and fireproof materials and composites

A folyóiratot referálja · The journal is referred by:
Cambridge Scientific Abstracts
ProQuest

A folyóiratban lektorált cikkek jelennek meg.
All published papers are peer-reviewed.
Kiadó · Publisher: Szilikátipari Tudományos Egyesület (SZTE)
Elnök · President: ASZTALOS István
1034 Budapest, Bécsi út 122–124.
Tel.: +36-1/201-9360 ▪ E-mail: epitoanyag@szte.org.hu
Tördelő szerkesztő · Layout editor: NÉMETH Hajnalka

Címlapfotó · Cover photo: KÓSA Luca Kornélia

WWW.EPITOANYAG.ORG.HU
EN.EPITOANYAG.ORG.HU

Online ISSN: 2064-4477
Print ISSN: 0013-970x
INDEX: 2 52 50 ▪ 70 (2018) 175–214

Bányaföldtani megfigyelések a Szarvaskő tardosi gabbróbányában

KLESPITZ JÁNOS

Érkezett: 2018. 06. 09. ▪ Received: 09. 06. 2018. ▪ https://doi.org/10.14382/epitoanyag-jsbcm.2018.31

Mining geology observations in the gabbro quarry at Szarvaskő Tardos

The gabbro quarry at Szarvaskő Tardos is located in the western part of Bükk Mountain, part of the North Central Mountains, in the valley of the Eger stream, 2.5 km from Szarvaskő village. The rock material of the quarry was known earlier as Western Bükk diabase, however, according to the current nomenclature the gabbro is referred as Tardos Gabbro Formation and Szarvaskő Basalt Formation. The basic magmatic rock formations are results of the undersea magmatic activity during the Jurassic period, Callovian stage. The total length of the pit wall in the gabbro quarry at Szarvaskő Tardos is 679 m in two mining operations levels. Volume of gabbro blocks is generally between 0.5-1.0 m^3, sometimes 2-3 m^3, and occasionally 8-10 m^3. The gabbro is dark grey in colour with greenish shade, dense, grained, hard and brittle fracturing. The paper describes the exploratory mining geology research of the quarry, the mineral composition of the gabbro together with its physical properties and utilization possibilities. The high quality gabbro of the quarry was utilized as crushed stone products for road construction and as construction blocks. The paper calls the attention to the need of more detailed, complex exploratory mining geology research for future utilization.

Kulcsszavak: gabbróbánya, bányafal, bányaföldtan
Keywords: gabbro quarry, pit wall, mining geology

KLESPITZ János
Aranyokleveles geológus. Munkahelyei: Jókai bánya, Alföldi Kőolajfúrási Üzem, AGROTERV, üzemi, ill. kutató geológus (1956-1970). 1970-től a Kő és Kavicsipari Egyesülésben földtani szolgálatvezető. Kiváló ifjú mérnök (1969). A földtani kutatás kiváló dolgozója (1976). A Magyar Népköztársaság által Kiváló Munkáért kitüntetésben részesült (1985). Az Eötvös Lóránd Tudományegyetem Tanácsa által aranyoklevél adományozásában részesült (2000). A Szilikátipari Tudományos Egyesület örökös tagja. Publikációinak száma: 53

1. Bevezetés

A tardosi gabbróbányával kapcsolatos bányaföldtani ismereteim a kőbányaipar földtani szolgálatának több évtizedes ellátása folyamán összegyűlt szakmai tapasztalatokon alapulnak.

A tardosi gabbróbánya az Északi Középhegység vonulatában húzódó Bükk hegység nyugati részén az Eger-patak völgyében, Szarvaskő községtől északra mintegy 2,5 km távolságra található (*1. ábra*). A déli folyásirányú Eger-patak a vizsgált területünk mellett húzódó hegység szerkezetileg előre jelzett eróziós völgyben kialakult medrében szállítja a vízgyűjtő területe felszíni vizeit Eger város, majd a Tisza irányába. A patak völgyének keleti oldalán levő gabbróbánya feletti területen és vele szemben, a völgy nyugati felén is, a felszíni alakzatokat 400-500 m tengerszintfeletti magasságú kiemelkedések képezik.

Tardosbánya alsó bányaművelési szintjének tengerszintfeletti magassága 264mAf. A cikk tárgyát képező bányaüzem erdős környezete a dombvidéki gyertyános, bükkös flóraövezet része.

1. ábra A tardosi gabbróbánya 1971-ben
Fig. 1. The gabbro quarry at Tardos in 1971

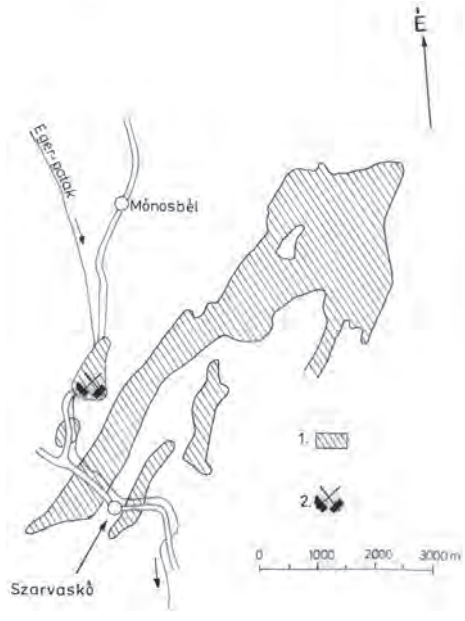

2. ábra A Tardosbánya helye és a Tardosi Gabbró valamint a Szarvaskői Bazalt Formációk elterjedése a Bükk hegység nyugati részén (MÁFI adatok alapján)
1- Tardosi Gabbró és Szarvaskői Bazalt Formációk
2- Tardosbánya
Fig. 2. Location of the quarry and the spread of Tardos Gabbro and Szarvaskő Basalt Formations in the western part of the Bükk mountain (based on MÁFI data)
1- Tardos Gabbro and Szarvaskő Basalt Formations
2- Tardosbánya

2. A bánya kőzetanyaga

A korábban diabázbányaként nyilvántartott Tardosbánya kőzetanyaga a Nyugati Bükki diabáz, gabbró előfordulás a jelenlegi nevezéktan alapján a Tardosi Gabbró és Szarvaskői Bazalt Formáció (*2. ábra*). A bázisos magmás kőzetek alkotta

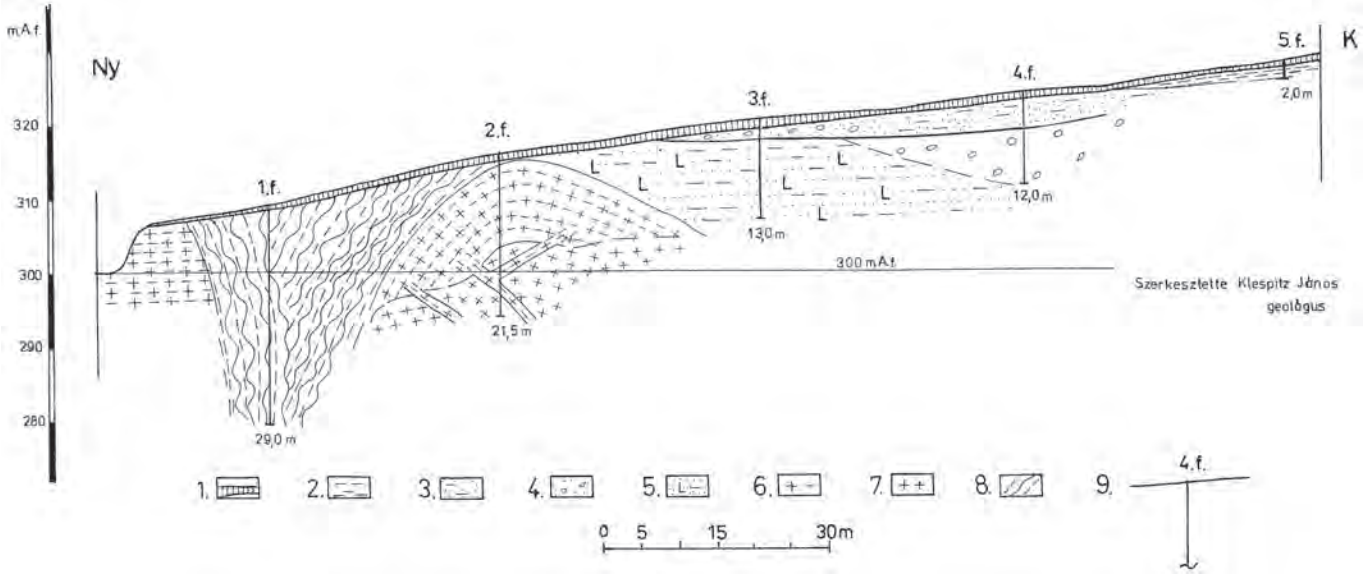

3. ábra *A tardosi gabbróbánya délkeleti nyersanyagterületének Ny-K-i irányú földtani szelvénye*
1- holocén humuszos termőtalaj
2- pleisztocén agyag
3- pleisztocén agyagos homok
4- pleisztocén kavicsos homok
5- pleisztocén agyagos homokliszt
6- jura, kallovi változóan bontott gabbró. Tardosi Gabbró Formáció
7- jura, kallovi üde megtartású gabbró. Tardosi Gabbró Formáció
8- jura, agyagpala. Tengeralatti lejtőüledék. Mónosbéli Formációcsoport
9- porfúrás

Fig. 3. *Location of the quarry and the spread of Tardos Gabbro and Szarvaskő Basalt Formations in the western part of the Bükk mountain (based on MÁFI data)*
1- Holocene humus soil
2- Pleistocene clay
3- Pleistocene clayey sand
4- Pleistocene pebbly sand
5- Pleistocene clayey powdery sand
6- Jurassic, Callovian Tardos Gabbro Formation, various levels of disintegration
7- Jurassic, Callovian Tardos Gabbro Formation, fresh condition
8- Jurassic shale, undersea slope sediment, Mónosbél Formation Group
9- powder drilling

előfordulás a jura kallovi emeletében lezajlott tengeralatti vulkánosság terméke. Az idősebb üledékes kőzeteken áttört, vagy abban megmerevedett magma a kontakt zónában az idősebb üledékes kőzetekben palásodást okozott (*3. ábra*).

Az egykori, jelenleg már nem üzemelő tardosi kőbánya nyugati irányból nyitotta meg a kelet felé emelkedő, maximálisan 550 m magasságú Tardos hegyet. A bánya mérete nyugat-kelet irányban 130 m, északkelet-délnyugat irányban eléri a 240 m-t (*4. ábra*).

A bányaüzem művelési szintjei 264 és 300 m Adria felett. A domináló kőjövesztés a 264 m-s szinten történt. A felső, 300 m-s szint részben lefedési szintként is szolgált.

3. A bánya létesítése

A tardosi gabbróbánya haszonkövét a földtani szakirodalom, térképek, területbejárások, földtani geofizikai vizsgálatok és legrészletesebben a bányászati feltárások (bányafalak) alapján ismerjük.

A tardosbányai gabbró térbeli helyzetének feltárására, a szükséges kőbányaipari ismeretek bővítése érdekében (a további bányaművelési irány meghatározása céljából) bányaüzemi földtani kutatást végeztünk, mely során felszíni geofizikai mérések, majd porfúrások mélyültek. A felszíni geofizikai méréseket az Országos Földtani Kutató és Fúró Vállalat Északmagyarországi Üzemvezetősége végezte. Nyugat-keleti irányú szelvények mentén 25×25 m-s hálóban mágneses mérések és minden második mérési ponton sekély elektromos szondázás is történt. A geofizikai mérések (izoohm térkép AB-80m) a bányafaltól déldélkeletre 30-70 m-s sávban nagy-

4. ábra *A tardosi gabbróbánya vázlatos térképe a földtani szelvény nyomvonalával*
1- bányafal
2- bányaudvar szint
3- kutató porfúrás
4- a földtani szelvény nyomvonala
5- a terepfelszín szintvonala

Fig. 4. *Schematic map of the gabbro quarry at Tardos with the track of the geological section*
1- Pit wall
2- Mining operations level
3- exploratory powder drilling
4- track of the geological section
5- terrain surface level line

ellenállású kőzetelőfordulást jeleztek. Majd tovább délkeleti irányba ezt a nagyellenállású kőzetet alacsony ellenállású (laza üledékes kőzetre, vagy agyagpalára utaló) anomália váltja fel.

A Kőbányaipar Földtani Szolgálata által kivitelezett üzemi földtani kutatás porfúrásait a felszíni geofizikai vizsgálatok információi alapján telepítettük úgy, hogy a nyugat-keleti irányú geofizikai szelvények mentén mért különböző ellenállású kőzetekről a fúrások alapján is nyerjünk ismereteket. A porfúrások lemélyítését követően immár komplex ismeretek alapján lehetővé vált az adatok bányaföldtani, majd bányaművelési kiértékelése (*3. ábra*). A bányaüzem haszonkövének értékeléséhez a legrészletesebb földtani ismereteket a nagy kőzetfelületek közvetlen vizsgálatát lehetővé tevő bányafalak szolgáltatták. A bányafalak előrehaladása folyamán szeletenként feltáruló falsíkok falszelvényeinek földtani értelmezésével a belső meddők betelepüléseinek térbeli alakulása is ismertté válik. Ezen új földtani információk a későbbi kutatásoknál és a bányaművelés tekintetében is meghatározó tényezők. Ez teszi feladatává a kőbányaipar földtani szolgálatának a bányafalak –esetenként nélkülözhetetlenné váló – földtani szelvényezését és dokumentálását.

4. Bányaföldtani és kőzettani elemzés

A tardosi gabbróbányában a bányafalak két szinten 679 m összhosszúságban teszik lehetővé a feltárult kőzetek közvetlen tanulmányozását, a felső szinten 262, az alsó termelési szinten 435 m hosszan. A tardosi bányaüzem mintegy 42 m vertikális kiterjedésben teszi lehetővé a Tardosi Gabbró Formáció közvetlen tanulmányozását.

A haszonkövet képező gabbró sötétszürke, zöldes árnyalatú, szemcsés szövetű, tömött, szilánkosan törő, kemény kőzet. A friss törési felületén világos, zöldesszürke és fekete ásványszemcsék mutatkoznak (*5. ábra*).

5. ábra A gabbró friss törési felülete
Fig. 5. Fresh fracture surface of gabbro

A gabbrót alkotó ásványok a szürke, zöldes árnyalatú plagioklász földpátok az anortit túlsúlyával, valamint általában sötét színű piroxén, gyakori a palackzöld áttetsző, üvegfényű olivin. A savanyú plagioklászokban az albit dominál, a bázikusokban az aniortit van túlsúlyban. A bázikus plagioklászok hajlamosabbak a mállásra.

Az olivin könnyen vesz fel vizet – pl. a hidrotermás folyamatok, vagy a mállás következtében – miközben szerpentinné alakul át.

A gabbró csiszolt kőzetfelületén mutatkozott egy éles kontúr mentén érintkező durvább ás finomabb szemcséjű kőzettípus. Jelezve hogy a bányaüzemmel feltárt bázikus magmás kőzet változó időben több fázisban képződött. A durvaszemcsés gabbró keletkezését követő későbbi magmafeláramlások folyamán az idősebb kőzet töréseiben, hasadékaiban, a gyorsabb lehűlés következtében már finomabb szemcséjű, diabáz típusú vulkanit jött létre (*6. ábra*).

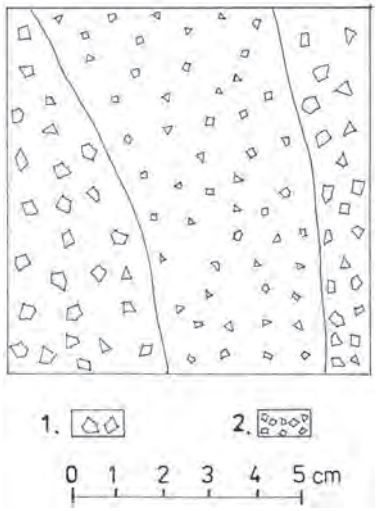

6. ábra A durva és finomabb szemcsés bázikus magmás kőzet kontaktusa
1- gabbró
2- finomabb szemcséjű diabáz típusú vulkanit
Fig. 6. Contact of the fine and coarser grained basic magmatic rocks
1- gabbro
2- finer grained diabase type vulcanite

A bányaudvarban a letermelt kőzethalmaz gabbrótömbjeinek kőzetlapjain 1-2 cm vastagságú kalcit erek mutatkoznak. A kalcit a gabbró hasadék és kőzetrés hálózatában áramló meszes oldatokból csapódott ki, melyek a tömbök kőzetfelületein kalcit erekként jelennek meg.

A kőzettömbök hasadékaiban elvétve pirit (FeS_2) hintés is előfordul, ami a haszonkő időállósága tekintetében nem kedvező. A levegőn a pirit vízoldható vasszulfátokká és limonittá alakul át. Így jön létre például a szulfidos érctelepek mállott zónája a „vaskalap" öve. Ugyanezen okból fontos az építőiparban felhasznált kőzetek piritmentessége is, mert az elbomló pirit nagyon lecsökkenti a kőzet élettartamát. A piritet a vegyiparban kénsav (H_2SO_4) előállítására is felhasználják.

A bányafalakkal feltárt tömeges megjelenésű gabbrót változó mértékben törések járják át. A közel függőleges, változó erősségű törések m-ként, máshol 4-5 m-ként fordulnak elő a bányafal síkjában (*7. ábra*).

A lerobbantott kőzethalmaz gabbrótömbjein mutatkozó csúszási felületek (vetőtükrök) a geotektonikus folyamatok eredményeként létrejött intenzív kőzetelmozdulásokat jelzik (*8. ábra*). A bányaföldtani felvételek alapján a bányafalakon mért törésirányok az É-D és ÉK-DNy. Az Eger-patak völgye is egy É-D orientációjú törési zóna mentén alakult ki.

A hegység szerkezetileg előre jelzett eróziós völgye által is egyre jobban felszínre került gabbró a bányaüzem telepítéséhez kedvező lehetőséget biztosított. A Bükk hegység déli völgyvonulatainál és az ezzel összefüggő vízhálózatainál is uralkodó az É-D orientációjú törésirány.

7. ábra Változó sűrűségű és erősségű törések a bányaüzem délkeleti bányafalán
Fig. 7. Various density and intensity fractures on the southeast pit wall of the quarry

8. ábra A lerobbantott kőzethalmaz gabbrótömbjein mutatkozó vetőtükör
Fig. 8. Fault plane showing on the gabbro blocks in the debris after explosive extraction

9. ábra Gabbrótömbök a lerobbantott kőzethalmazban
Fig. 9. Gabbro blocks in the debris after explosive extraction

A bányászati tapasztalatok alapján a kőzetelváltozásoktól mentes, üde, tömött szövetű gabbró zúzott és építőkő előállítására kiválóan alkalmas. A gabbró térfogatsúlya: 2,8-3,1 g/cm^3, nyomószilárdsága: 3000 kp/cm^2, fagyálló, csiszolható és jól fényezhető.

Az egykor még üzemelő Tardosbánya 1971. éves termelési terve: 30.000 t építő és zúzottkő volt.

A mintegy 36 m függőleges kiterjedésű bányafal törési hálózatának helyenkénti kedvező alakulása – ritkább töredezettség – (*7. ábra*) tette lehetővé a lerobbantott halmazban mutatkozó jelentős kőzettömb előfordulást. A gabbrótömbök mérete változó (*9. ábra*). A leggyakoribb a 0,5-1,0 m^3 ritkábban 2-3, de esetenként a 8-10 m^3-es is előfordul (*10. ábra*).

10. ábra Tetemes méretű gabbrótömb a bányaudvarban
Fig. 10. Large size gabbro block at the mining operations level

11. ábra Hasítással szabályosra formált gabbrótömb
Fig. 11. Regular shape gabbro block after split processing

A kőzettömbök felületén helyenként ún. bőrösödés – sárgásbarna elszíneződés – mutatkozik, ami a gabbró kőzetréseiben, töréseiben áramló oldatok vasas kicsapódása. A kőzettömbök hosszabb idejű felszíni tárolása folyamán is kialakul egy oxidációs felületi elszíneződés. A bőrösödés a kőzet felhasználhatóságát nem befolyásolja, mivel az elszíneződés a gabbró felületén csak néhány tizedmilliméter. A haszonkő minőségét a bőrösödés alatti üde kőzet kőzetfikai paraméterei határozzák meg.

Az üde gabbrótömbök kőzetanyagának kellemes színhatása, textúrája és jó megművelhetősége, díszítő és burkolókőként felhasználás tekintetében is kedvező. A 90-es évek elején díszítőkőlapok előállítása céljából Tardosbányáról gabbrótömböket szállítottak az Almásneszmélyi kőfeldolgozó üzembe. Mivel a tömbök szabálytalan alakúak ezért gépi feldolgozáshoz (lapvágás) azokat még a bányában elszállítás előtt, hasítással megfelelő szabályos formára kellett átalakítani (*11. ábra*). Általában egy 2-3 m^3-es szabálytalan tömbből egy 1,5 m^3-es gépi vágásra alkalmas tömb alakítható ki. Bár ezt a kinyerési arányt a tömb eredeti alakja is befolyásolja.

5. A bánya jelenlegi állapota és javaslatok

Az egykori bányaüzem 2017-ben történt bejárása folyamán (*12. ábra*) tapasztaltak alapján a bányaudvarban évtizedeken át tárolt tömbökön már mutatkozik a felszíni mállás következménye, a kőzetélek lekerekedése, némelyeknél a gömbölyded forma kialakulása (*13-14. ábra*). A kőzettömbök erózióval szembeni egyenlőtlen reagálása, a változatos ásványos összetétel természetes következménye.

A tardosi gabbróbánya művelése folyamán a fedőmeddőn kívül a haszonkő genetikájából adódóan igen változatos belső meddővel is számolni kell. Ugyanis s felnyomuló magmafeltörések között becsípődött agyagpala (*3. ábra*) a kőbányászat részére belső meddőnek minősül. Az agyagpala horizontális kiterjedése igen változatos. Például a közeli egerbaktai gabbróbányában a kivitelezett üzemi földtani kutatás feltárásai alapján meghaladta a több tíz m-t, ami miatt ott a bányaművelést mélység irányába lehetett tovább folytatni.

12. ábra A felhagyott gabbróbánya 2017-ben
Fig. 12. The abandoned quarry in 2017

13. ábra Gabbrótömbök a felhagyott bánya udvarán
Fig. 13. Gabbro blocks at the mining operations level in the abandoned quarry

Az eddigi bányászati és bányaföldtani ismeretek alapján a Bükk hegységi gabbró előfordulásokon bányanyitás céljából indítandó ipari földtani kutatások esetén a gabbróban a várható belső meddők helyeinek és kiterjedésének szükséges mértékű megismerése érdekében körültekintően, a célnak megfelelő komplex, részletes vizsgálatokat kell alkalmazni.

14. ábra A több évtizedes felszíni mállás hatása a gabbrótömbökön
Fig. 14. Influence of several decades' weathering on the gabbro blocks

6. Összefoglalás

A tardosi gabbróbánya kőzetanyagának, megjelenési módjának és települési helyzetének részletes megismerését a kőbányaipar földtani szolgálatának több évtizedes ellátása folyamán tapasztaltak tették lehetővé.

A tardosi kőbányaütem korábban diabázként nyilvántartott haszonköve, a jelenlegi nevezéktan alapján a Tardosi Gabbró Formáció a jura időszak kallovi emeletében lezajlott tengeralatti vulkánosság terméke.

A cikk bemutatta a gabbró bányaföldtani kutatását, anyagi összetételét, kőzetfizikai paramétereivel és felhasználási lehetőségeivel. A tardosi gabbró zúzott és építőkő előállítására kiválóan alkalmas. A bányafalon mutatkozó törések, kőzetrések gyakorisága adta lehetőségek függvényében mutatkozó tömbös megjelenés díszítőkőipari tekintetben is perspektivikussá teszi.

A bányaföldtani tapasztalatok alapján a gabbró genetikájából adódó agyagpala belső meddő térbeli helyzetének részletesebb feltárására, az esetleges későbbi kőkutatásoknál célszerű az eddiginél részletesebb, megfelelő komplex vizsgálatokat alkalmazni.

Irodalom

[1] Balogh, K. (1964): A Bükk hegység földtani képződményei. *MÁFI Évkönyv* XL VIII. Bp. 1964.
[2] Klespitz, J. (1976): A Kőbányászati Egyesülés bányáinak fekü és belső meddő viszonyai. *Szilikáttechnika*. 1976/2. sz. 52-57. oldal.
[3] Klespitz, J. (1982): Bányaföldtani tapasztalatok a kőbányaiparban. *Földtani Kutatás*, XXV. évf. 1982/3-4.sz.
[4] Klespitz, J. (1984): Próbatermeléssel végzett díszítő tömbkő kutatás az Erdősmecskei Gránitbányában. Építőanyag XXXVI. évf. 1984/5.sz. 151-155. oldal.
[5] Klespitz, J. (1977): Földtani kutatások porfurások alkalmazásával. *Mérnökgeológiai Szemle*. 1977. IV. 59-62 oldal.
[6] Koch, S. (1985): Magyarország ásványai. *Akadémiai Kiadó*, Budapest 1985.
[7] Vadász, E. (1960): Magyarország földtana. *Akadémia Kiadó*, Budapest 1960.
[8] Vitális, Gy. (1984): Szilikátipari nyersanyagok. *Szilikátipar-Építőipar* 3. ETK, Budapest 1984. 1-207. oldal.

Ref.:
Klespitz, János: *Bányaföldtani megfigyelések a Szarvaskő tardosi gabbróbányában*
Építőanyag – Journal of Silicate Based and Composite Materials, Vol. 70, No. 6 (2018), 176–180. p.
https://doi.org/10.14382/epitoanyag-jsbcm.2018.31

Microstructural evaluation of Re particle reinforced composite on aluminium surface by friction stir processing

Marek Stanisław WĘGLOWSKI ▪ Department of the Testing of Materials Weldability and Welded Construction, Institute of Welding ▪ marek.weglowski@is.gliwice.pl

Adriana WRONA ▪ The Department of Material Science and Powder Metallurgy, Institute of Non Ferrous Metals ▪ adrianaw@imn.gliwice.pl

Ilona NEJMAN ▪ Department of Materials Science and Non-Ferrous Metals Engineering, Faculty of Non Ferrous Metals, AGH University of Science and Technology ▪ Inejman@agh.edu.pl

Maria RICHERT ▪ Faculty of Management, AGH University of Science and Technology ▪ mricher@agh.edu.pl

Érkezett: 2018. 07. 31. ▪ Received: 31. 07. 2018. ▪ https://doi.org/10.14382/epitoanyag-jsbcm.2018.32

Abstract

The paper presents the results of friction stir processing (FSP) process of cast aluminium alloy AlSi9Mg. The studies included a modification of the microstructure in the grain refinement, elimination of voids and the production of composite material AlSi9Mg + Re. Rhenium is famous for its refractory character, high density as well as high hardness. It is well known as alloying element for improvement of strength, plasticity, weldability, reduction of the degree of recrystallization embrittlement mainly in W, Mo and Ni based alloys. Re is used in superalloys as a solid-solution strengthening alloying element and increasing corrosion resistance at high temperatures. Rhenium containing alloys have high electrical resistivity and refractory character. The modification was carried out single-and multiple runs. The results show significant fragmentation in the mixing microstructure, and a metallic continuity. Fragmentation in the mixing microstructure was confirmed by SEM research. The study revealed that mechanical alloying technology FSP allows to increase the hardness of the material. The ability to produce graded materials AlSi9Mg alloy matrix by frictional treatment is also indicated.

Keywords: Friction Stir Processing, rhenium, composite

Kulcsszavak: dörzshegesztési eljárás, rénium, kompozit

Marek St. WĘGLOWSKI

He received his Ph.D. degree in AGH in Krakow in 2010. He is currently working at the Institute of Welding University of Science and Technology in Gliwice (Poland) as Associate Professor. Author of 148 scientific publications, 6 monographs and 82 presentation (and posters). Area of Interest – surface modification technology, weldability of high strength steel, electron beam technologies.

Adriana WRONA

Doctor of Philosophy in Physics, Since 2006 – Institute of Non-Ferrous Metals in Gliwice in a position of adiunkt, including: since 2013 – Head of Powder and Composite Materials Department, from 2007 to 2012 - head of Laboratory of Metallic Powder and Composite Materials in the Department of Materials Engineering and Powder Metallurgy. She is author or coauthor of 15 inventions applied for patent protection to the Patent Office of the Republic of Poland (UPRP) and 57 scientific publications.

Ilona NEJMAN

is a PhD at the Faculty of Non-Ferrous Metals at the in Krakow. In the AGH University of Science and Technology department related from the beginning of her academic path. She is a co-author of scientific articles on Polish and international scale. Research leads in the field of surface engineering.

Maria RICHERT

is a Prof. D.Sc. Ph.D at AGH University of Science and Technology (Poland , Kraków). She is author and co-author of 168 articles, co-author of two chapters in books in English language and author of scientific book in Polish. She presented of 50 lectures at national and international conferences, and participated in 70 conferences. Prof. Maria Richert participated in 68 different scientific projects, works order by industry as manager or contractor.

1. Introduction

The friction stir processing (FSP) is a solid state process, and therefore the problem related to the liquid phase processing can be eliminated [1]. Friction stir processing was developed based on the concept of friction stir welding (FSW). Conventional FSP is performed with a tool consisting of a shoulder that touches the surface of the modified material, and a smaller pin, which penetrates into the material thickness. The shoulder essentially prevents the escape of softened material as the tool is rotated and forced along the designed path. The pin, commonly threaded, pushes the surrounding material downward, assisting in the retention of material within the modified zone. The downward force applied to the tool to maintain the correct plunge depth also results in a forcible contact between the shoulder and the workpiece surface. The relative motion from the tool rotation results in significant heat generation from friction at the shoulder interface. The pin generates heat by both friction and plastic deformation. A detailed description of the FSP process was described in the previous papers [2].

In addition, the large processing strain results in microstructural refinement and homogenisation. This has led to several applications such as grain refinement for superplasticity, modification of casting microstructure as well as composite materials fabrication [3-6]. The FSP in one or multi-run technique can be carry out [7].

To date, a few authors presented interesting results on friction stir processing with filler material. *Gandra* et al. [8] reported the study of producing the functionally graded metal matrix composite (MMC) reinforced by SiC ceramic particles with median size of 118.8, 37.4 and 12.3 μm. AA5083 aluminium alloy plates in the H111 and partially annealed conditions were processed. Several strategies for reinforcement were investigated and its influence on the particle distribution and homogeneity was studied. A square shaped groove packed with reinforcement particles of SiC was studied and it was seen that it was more effective when the groove was placed under the probe. *Mahmoud* et al. [9] revealed that the SiC particles were distributed more homogeneously in the nugget zone, of an A1050-H24 aluminium plate, by using square probe tool than other shapes. *Kurtyka* et al. [10] explained the influence of the plastic deformation generated in friction stir processing on the changing concentration and distribution of SiC reinforcement particles in the cast composite A339/SiC/p, as well as determined its mechanical properties. *Sathiskumar* et al. [11] reported that in Cu/B_4C surface composite, the SZ area with B4C particles was reduced as compared to the SZ area in FSP of copper without particles. The number of the major achievements in the field of FSP technology with additional particles is well presented in the review paper of *Sharma* [12].

Taking advantages of FSP to reinforcement and refinement the grain of alloys has recently attracted attention of researchers [12]. However, no work has been yet reported on mechanical alloying by FSP of cast aluminium alloy with rhenium particle [13].

Rhenium, is famous for its refractory character (melting point 3186°C), high density (21.02 g/cm^3), high hardness (7 in Mohs scale, up to 7850 MPa - Vickers) thermal Conductivity (71.2 W/m·K at 20°C). It is well known as alloying element for improvement of strength, plasticity, weldability, reduction of the degree of recrystallization embrittlement mainly in W, Mo and Ni based alloys. Re is used in superalloys as a solid-solution strengthening alloying element and increasing corrosion resistance at high temperatures. Rhenium containing alloys have high electrical resistivity and refractory character. Due to its properties rhenium is often used in alloys for turbines in aircraft engines or vehicle shields, heating elements, thermocouples, vacuum electrodes and in catalysts (Pt-Re) for high-octane unleaded fuels [14-15]. The second wide range of application is surface engineering application. The previous experiment revealed that the Re can improve hardness as well as wear resistance characteristic of material surface [16-21].

In the present paper, the microstructural evaluation of cast aluminium alloy AlSi9Mg modified by friction stir processing with Re particles was presented. The microstructural analysis by means of light microscopy, scanning electron microscopy, chemical microanalysis by energy dispersive spectroscopy (EDS) analysis were carried out.

2. Materials and experimental procedure

Commercial available AlSi9Mg cast plates 6 mm in thickness for friction stir processing modification and the Rhenium powder (99,8% Re, KGHM Polska Miedź) as additional particles were used. The FSP process was performed at the following parameters: rotational speed ω=560 rpm, travelling speed v=560 mm/min, tilt angle α=1.5° at the Instytut Spawalnictwa (Institute of Welding) using a welding machine built on the base of a conventional, vertical milling machine FYF 32JU2. The FSP Triflute tool (*Fig. 1*) was made of HS6-5-2 high speed steel. The tool was machined to have a shoulder diameter 20 mm, pin diameter 8 mm, and pin depth 4.5 mm. The workpiece was clamped tightly to an 8 mm thick plate made of plain carbon steel which served as a reinforcement and then fixed to the machine table. The surface of plates was not cleaned before processing. The rhenium powder was filled into a groove of 2–3 mm width and 1–2 mm depth. Double passes were applied in order to improve the homogeneity of the Re particle distribution. The first pass was conducted in such way that grove was on the advancing side. In the second pass, the tool was moved along the same line as the axis of the grove at the same travelling direction.

Examination of the microstructure for all of the samples was studied using a light microscope OLYMPUS GX5 and Scanning Electron Microscope Hitachi SU 70. The samples to light microscopy observations were polished mechanically applied Struers equipment and technique. They were grinded, than polished in diamond pastes and in suspension OPS. Microhardness of modification material was performed by using a microhardness types PMT3 at load 100 G.

Fig. 1. FSP Triflute tool
1. ábra FSP Triflute szerszám

3. Results and discussion

Firstly, the microscopic examination of parent material cast aluminium alloy AlSi9Mg were performed by SEM and light microscopies. *Fig. 2* shows LM and SEM micrographs of AlSi9Mg samples in the as-cast condition. The microstructure is mainly composed of α-Al dendrites and Si particle concentrated Al-Si eutectic regions. This type Si particles segregation in the interdendritic regions is the effect of the natural solidification sequence of this alloy, the sizes and morphologies vary depending on the melt chemistry and the cooling rate. The porosity occurs in the base metal (*Fig. 3*). The distribution of Si, Mg particles is not uniform throughout the aluminium matrix [22].

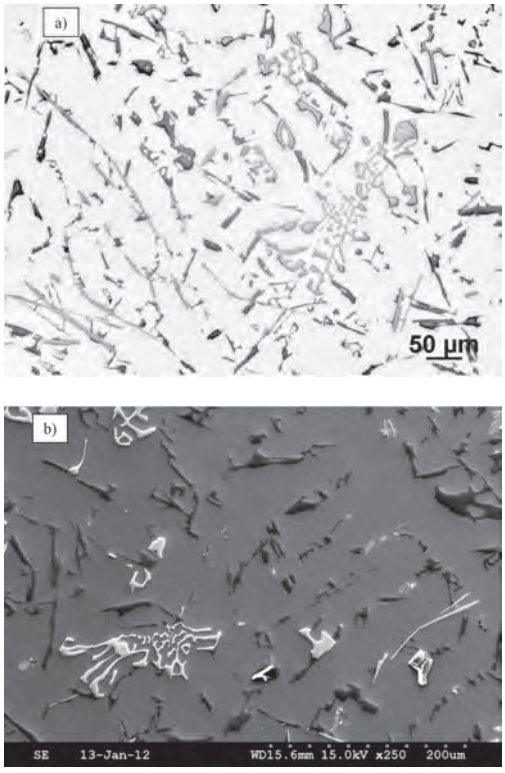

Fig. 2. Microstructure of cast aluminium alloy AlSi9Mg grade, a) light microscopy, b) SEM
2. ábra AlSi9Mg minőségű alumínium ötvözet mikroszerkezete, a) fénymikroszkópia, b) SEM

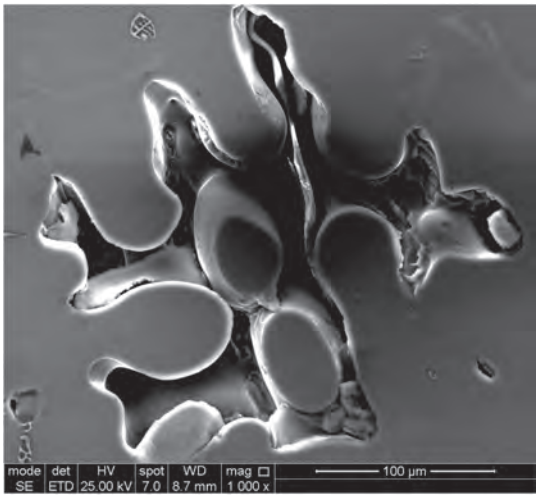

Fig. 3. The porosity of cast aluminium alloy AlSi9Mg grade
3. ábra AlSi9Mg minőségű alumínium ötvözet porozitása

Secondly, the macrostructure and microstructure after FSP process with rhenium were analysed. Particles of Re of 73 µm median diameter were used as the reinforcement as shown in *Figs. 4* and *5*. The single grain of Re powder has no uniform shape and dimension.

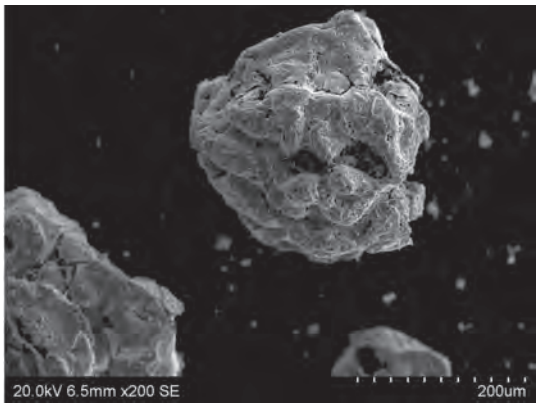

Fig. 4. SEM observation of Re particles
4. ábra Re szemcsék SEM felvétele

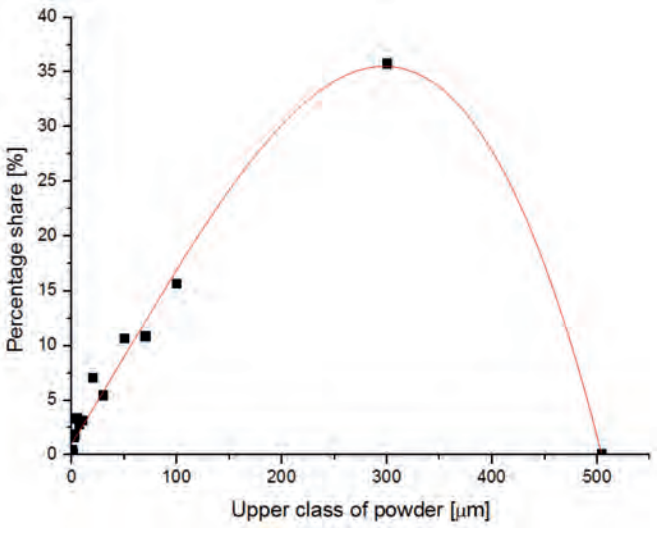

Fig. 5. Percentage share of upper class of powder
5. ábra A por felső osztályának százalékos aránya

Transverse section of the as-received AlSi9Mg after FSP modification on *Fig. 6* is presented. Severe plastic deformation and material flow caused by the stirring action of the tool together with increased temperatures due to friction force are responsible for the grain refinement and dynamic recrystallization in the processed area. FSP also brings about the closure of casting pores and a general homogenization of the microstructure. As a result of FSP the as-cast material is converted into a near-wrought condition. The microstructure of the area subjected to the FSP process with the specific parameters shows a classic asymmetry and macroscopic inhomogeneity. On the strip on the advanced side, where the microstructure is altered by reinforcement, there is a local segregation at the interface between the material flow direction.

Moreover, the FSP resulted in a significant refinement of large Si particles and subsequent uniform distribution in the aluminium matrix as well as porosity in the as cast AlSi9Mg was nearly eliminated by FSP. The structures and analysis of AlSi9Mg alloy after the introduction of rhenium by Friction Stir Processing are compared in *Figs. 7-8*. The chemical analysis by EDS has indicated the presence of rhenium in both the surface layer and the interior of the examined material. On the whole surface of the test material, rhenium was disposed in the form of white "spots" (*Fig. 7a*). On the cross-section of the test material, Vickers microhardness was measured under a load of 100 g. The obtained values differed quite considerably. The places on the sample surface and in the interior where the presence of rhenium has been identified showed an increase of microhardness up to about 100 µHV, while in the remaining areas the values of microhardness ranged from 68 - 75 µHV.

4. Conclusions

The present study has examined the FSP process after modified AlSi9Mg cast aluminium alloy with rhenium. The results were as follows:

- the microstructure of the area subjected to the FSP process shows a classical asymmetry and macroscopic inhomogeneity,
- FSP of the AlSi9Mg aluminum alloy resulted in a significant breakup of coarse acicular Si particles and primary aluminum dendrites, created a homogeneous distribution of Si particles in the aluminum matrix, and nearly eliminated all casting porosity,
- on the whole surface of the test material, rhenium was disposed in the form of white „spots"
- an increase of microhardness up to about 100 µHV is observed while in the remaining areas the values of microhardness ranged from 68 - 75 µHV,
- SEM-EDS analysis revealed concentration of rhenium in the modified material.

5. Acknowledgements

This work has been performed with funding from National Centre for Research and Development and KGHM Polska Miedź in Poland in the frame of the research grant RE-COVER No CuBR2/2982/2014.

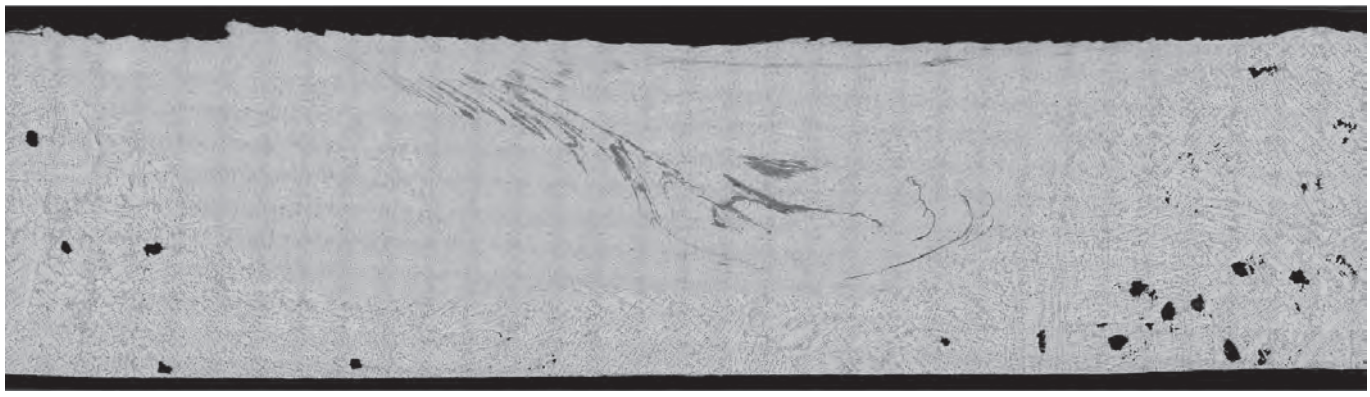

Fig. 6. Macrostructure of the cross-sectional area after FSP modification, advancing side on the left
6. ábra Keresztmetszet makroszerkezete a dörzshegesztést követően, előre oldal a baloldalon

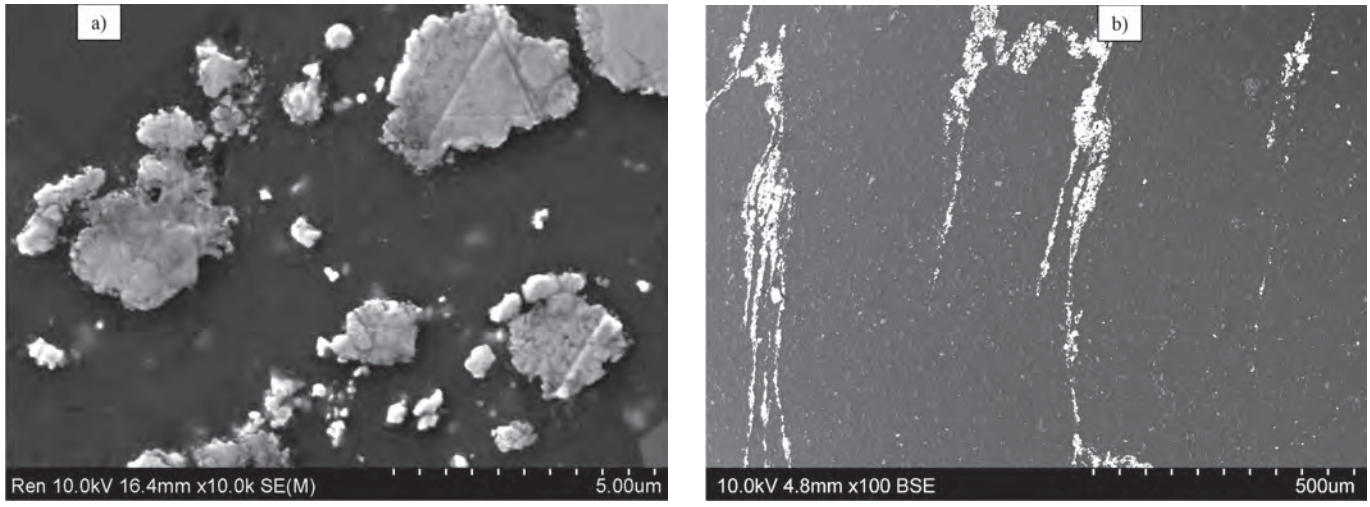

Fig. 7. Macrostructure of the cross-sectional area after FSP modification: a) the upper surface, b) the middle part tested material (SEM)
7. ábra Keresztmetszet makroszerkezete a dörzshegesztést követően: a) felső felület, b) a középső területen vizsgált anyag (SEM)

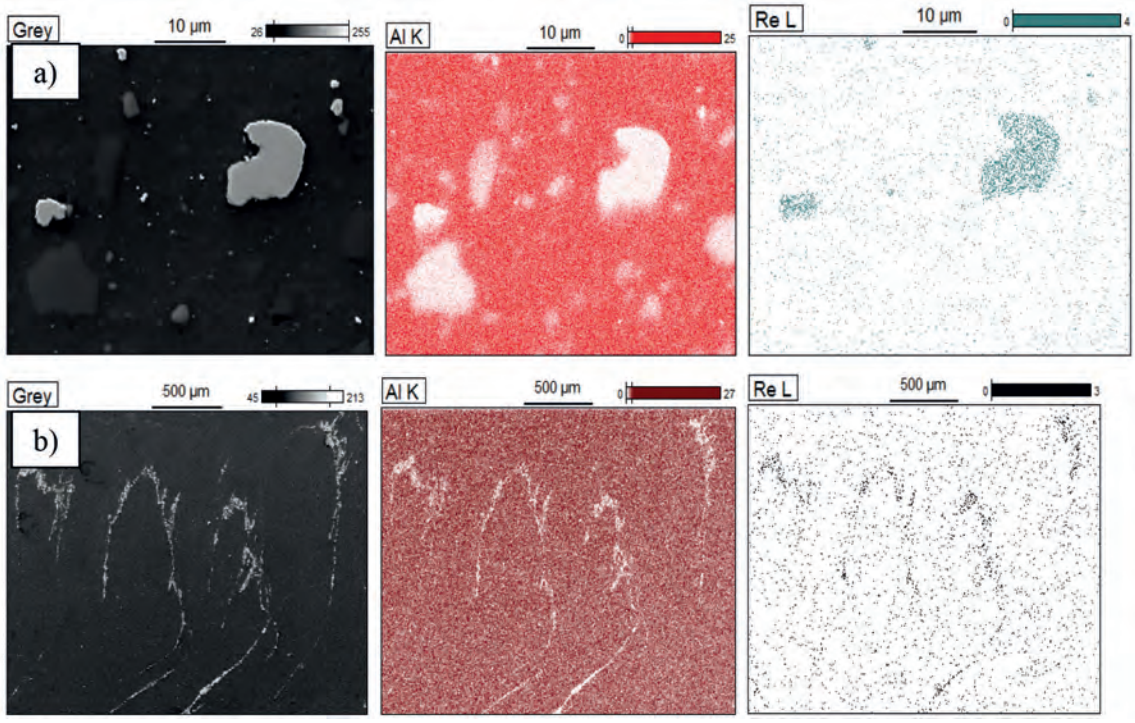

Fig. 8. SEM analysis with corresponding EDS spectra: a) the upper surface, b) the middle part tested material
8. ábra SEM analízis, összetartozó EDS spektrumokkal: a) felső felület, b) a középső területen vizsgált anyag

References

[1] Mahmoud, E. R. I. – Ikeuchi, K. – Takahashi, M. (2008): Fabrication of SiC particle reinforced composite on aluminium surface by friction stir processing. *Science and Technology of Welding and Joining*. Vol. 13, No 7, pp. 607-618, https://doi.org/10.1179/136217108X333327

[2] Węglowski, M. St. – Dymek, S. (2013): Relationship between Friction Stir Processing parameters and torque, temperature and the penetration depth of the tool. *Archives of Civil and Mechanical Engineering*. Vol. 13, No 2, pp. 186-191, https://doi.org/10.1016/j.acme.2013.01.003

[3] Weglowski, M. St. – Pietras, A. – Dymek, S. – Hamilton C. (2012): Characterization of Friction Modified Processing – a Novel Tool for Enhancing Surface Properties in Cast Aluminium Alloys. *Key Engineering Materials*. Vol. 504-506, pp. 1231-1236, https://doi.org/10.4028/www.scientific.net/kem.504-506.1231

[4] Hamilton, C. – Weglowski, M. St. – Dymek, S. (2015): A Simulation of Friction-Stir Processing for Temperature and Material Flow. *Metallurgical and Materials Transactions B. Vol. 46*, No 3, pp. 1409-1418, https://doi.org/10.1007/s11663-015-0340-z

[5] Węglowski, M. St. – Dymek, S. (2012): Microstructural modification of cast aluminium alloy AlSi9Mg via Friction Modified Processing. *Archives of Metallurgy and Materials*. Vol. 57, No 1, pp. 71-78, https://doi.org/10.2478/v10172-011-0155-0

[6] Shafiei-Zarghani, A. – Kashani-Bozorg, S. F. – Zarei-Hanzaki, A. (2009): Microstructures and mechanical properties of Al/Al2O3 surface nano-composite layer produced by friction stir processing. *Materials Science and Engineering A*. Vol. 500, No 1-2, pp. 84-91. https://doi.org/10.1016/j.msea.2008.09.064

[7] Kopyscianski, M. – Weglowski, M. St. – Dziadosz, M. – Malyszko, M. – Dymek, S. (2015): Electron microscopy investigation of a cast AlSi9Mg aluminum alloy subjected to friction stir processing with overlapping passes. *International Journal of Materials Research*. Vol. 106, No 7, pp. 813-817, https://doi.org/10.3139/146.111203

[8] Gandra, J. – Miranda, R. et al. (2011): Functionally graded materials produced by friction stir processing. *Journal of Materials Processing Technology*. Vol. 211, No 11, pp. 1659-1668. https://doi.org/10.1016/j.jmatprotec.2011.04.016

[9] Mahmoud, E. R. I. – Takahashi, M., et al. (2009): Effect of friction stir processing tool probe on fabrication of SiC particle reinforced composite on aluminum surface. *Science and Technology of Welding and Joining*. Vol. 14 No, pp. 413÷425, https://doi.org/10.1179/136217109X406974

[10] Kurtyka, P. – Rylko, N. – Tokarski, T., et al. (2015): Cast aluminium matrix composites modified with using FSP process - Changing of the structure and mechanical properties. *Composite Structures*. Vol. 133, pp. 959-967, https://doi.org/10.1016/j.compstruct.2015.07.122

[11] Sathiskumar, R. – Murugan, N., et al. (2013): Characterization of boron carbide particulate reinforced in situ copper surface composites synthesized using friction stir processing. *Materials Characterization*. Vol. 84, pp. 16–27, https://doi.org/10.1016/j.matchar.2013.07.001

[12] Sharma, V. – Prakash, U. – Kumar, B. V. M. (2015): Surface composites by friction stir processing: A review. *Journal of Materials Processing Technology*. Vol. 224, pp. 117–134, https://doi.org/10.1016/j.jmatprotec.2015.04.019

[13] Węglowski, M. St., (2018): Friction Stir Processing – state of the art. *Archives of Civil and Mechanical Engineering*. Vol. 18, No 1, pp. 114-129, https://doi.org/10.1016/j.acme.2017.06.002

[14] Davis, J. R. (1997): ASM specialty handbook: Heat-resistant materials, *ASM International*, 379-380.

[15] Poole, Jr. Ch. P. (2004): Encyclopedic dictionary of condensed matter physics, Vol. 1 A-M, *Elsevier Inc.*, San Diego, pp. 1142-1143.

[16] Huang, L. – Sun, X. F. – Guan, H. R. – Hu, Z. Q. (2006): Effect of rhenium addition on isothermal oxidation behavior of single-crystal Ni-based superalloy. *Surface and Coatings Technology*. Vol. 200, No 24, pp. 6863-6870, https://doi.org/10.1016/j.surfcoat.2005.10.037

[17] Kolmakov, A. G. – Geminov, V. N., et al. (1995): Effect of rhenium coatings on the mechanical properties of molybdenum wires. *Surface and Coatings Technology*. Vol. 72, No 1-2, pp. 43-50,5 https://doi.org/10.1016/0257-8972(94)02329-O

[18] Chrzanowska, J. – Hoffman, J. (2015): The effect of process parameters on rhenium diboride films deposited by PLD. *Surface and Coatings Technology*. Vol. 277, pp. 15–22, https://doi.org/10.1016/j.surfcoat.2015.07.024

[19] Chmielewski, M. – Piatkowska, A. (2015): Effect of Rhenium Addition on Wear Behavior of Cr-Al2O3 Metal Matrix Composites. *Journal of Materials Engineering and Performance*. Vol. 24, No 5, pp. 1871-188, https://doi.org/10.1007/s11665-015-1462-9

[20] Chmielewski, M. – Pietrzak, K. – Strojny-Nedza, A. – Dubiel, B. – Czyrska-Filemonowicz, A. (2014): Effect of Rhenium Addition on the Strengthening of Chromium-Alumina Composite Materials. *International Journal of Materials Research*. Vol. 105, No 2, pp. 200–207, https://doi.org/10.3139/146.111002

[21] Kurzynowski, T. – Smolina, I., et al. (2017): Wear and corrosion behaviour of Inconel 718 laser surface alloyed with rhenium. Materials & Desing, Vol. 132, pp. 349-359, https://doi.org/10.1016/j.matdes.2017.07.024

[22] Weglowski, M. St., (2014): Microstructural characterisation of friction stir processed cast AlSi9Mg aluminium alloy. *Archives of Foundry Engineering*. Vol. 14, No 3, pp.75-78.

Ref.:

Węglowski, Marek Stanisław – **Wrona,** Adriana – **Nejman,** Ilona – **Richert,** Maria: *Microstructural evaluation of Re particle reinforced composite on aluminium surface by friction stir processing*

Építőanyag – Journal of Silicate Based and Composite Materials, Vol. 70, No. 6 (2018), 181–185. p.

https://doi.org/10.14382/epitoanyag-jsbcm.2018.32

Preparation and characterization of lightweight geopolymer composites using different aluminium precursors

Hisham Mustafa Mohamed KHATER ▪ Housing and Building National Research Center, Cairo ▪ hkhater4@yahoo.com, hkhater4@hbrc.edu.eg

Érkezett: 2018. 07. 02. ▪ Received: 02. 07. 2018. ▪ https://doi.org/10.14382/epitoanyag-jsbcm.2018.33

Abstract

Production of lightweight building materials attract attention of the scientists worldwide with the need for reducing the structures dead-weight, provide better thermal insulation for buildings, and cost less to transport. The current work focuses on production of lightweight geopolymer composites by the incorporation of aluminium powder and aluminium slag in various ratios for water cooled slag/ kaolinite sand composite, the activators used were 6% of equal ratio from sodium hydroxide and sodium silicate. The properties of the produced lightweight geopolymer composites have been studied through measurement of compressive strength, bulk density, water absorption, FTIR, XRD and SEM imaging. Results demonstrate modification for both physico-mechanical and microstructural characteristics by using aluminium powder and aluminium slag forming lightweight composites with density below 2.15 g/cm3 depending on the studied mix composition.

Keywords: lightweight geopolymer, activation, aluminium, slag
Kulcsszavak: könnyű geopolimer, aktiválás, alumínium, kohósalak

Hisham Mustafa Mohamed KHATER
Ph.D. in Physical Chemistry, 2009. Associated Professor in Cement chemistry and Raw Building Materials Technology and Processing since 2015. Researcher in Raw Building Materials Technology and Processing Research Institute, Housing and Building National Research Center (HBRC). Supervisor of XRF laboratory for the chemical analysis of all type of raw building materials, accredited from International American Service IAS 17025 since 2005. Research interest: X-ray fluorescence spectroscopy, X-ray diffraction, Fourier Transformer-IR spectroscopy, differential thermal analysis, chemical analysis of cements, recycling of waste materials, assessment of clay minerals, low cost and environmentally green building materials, nanotechnology in building materials. Author of more than 20 papers.

1. Introduction

Today, the need for production of new ecofriendly building materials from country's natural resources and waste by-products has been increased vastly with an increase of general awareness about environmental issues which led to a growing concern over waste generation and the realization that such materials must be treated, eliminated or re-used. Rising consumption and the concomitant increase in industrial production has occasioned both a rapid decline in natural resources and generation of large volumes of waste or by-products [1]. Recent researches into the economically viable re-use of wastes have given rise to different proposals, including the possibility of its inclusion in building materials [2,3].

These materials categorized under the alkali activated materials and commonly known as geopolymer if their resources are from nature geological origins reach in silicon and aluminium, whilst industrial by-products rich in alumina and silica oxides such as coal fly-ash, silica fume and granulated blast furnace slag considered as alkali activated materials which is the major category, while the geopolymers can be considered as subset from this mother set as coincide with the pioneer scientists *Davidovits* in 1970s [4,5], who discovered and established of the research in geopolymer binders.

The basic binding phase in geopolymers is an amorphous aluminosilicate gel that consists of a three dimensional framework of SiO_4 and AlO_4 tetrahedra linked by corner-shared O atoms [6-8]. Geopolymer binders hold many advanced properties over traditional ones although the most important is their low manufacturing energy consumption and low CO_2 emission [9,10], which can be sorted as a *Green Material* [11]. The important of green materials increased also vastly with the increased ability for producing lightweight building materials in construction sector that can insulate heat and sound, where traditionally, ordinary Portland cement (OPC) has been used as the binder for concrete [12-14], exhibits high thermal transmission and said to be responsible for about 7% of the CO_2 emission worldwide.

The development of lightweight building materials with good mechanical properties can reduce the deadweight of structures, provide better thermal insulation for buildings, and cost less to transport and erect when prefabricated structural components are made in factory, whereas using lightweight aggregates is one of the most common known ways for making lightweight building materials [15,16].

The use of lower densities concrete is beneficial in terms of structural load-bearing, and as acoustic and thermal insulation. The density can be reduced by replacing part of the solids by air voids or lightweight aggregates, several approaches exist for this objective. In the method known as no-fines concrete, the fine aggregate is omitted; whereas in the called lightweight concretes, the normal aggregates are replaced by lightweight to reduce the density. If air voids are introduced into the cement paste to reduce its density, the concrete is known as cellular, aerated, or foamed concrete [17,18], which can reduce the quantity of raw material (sand, cement and lime) of up to 30%, which knocks down the cost of building materials.

There are many types of materials that can be suitable for lightweight thermal insulation and fall under the following basic materials and composites [19, 20]:

1. Inorganic materials

a. Fibrous materials such as glass, rock, and slag wool, fly ash.

b. Cellular materials such as calcium silicate, bonded perlite, vermiculite, ceramic products and geopolymer.

2. Organic materials

a. Fibrous materials such as cellulose, cotton, wood, pulp, cane, or synthetic fibers.

b. Cellular materials such as cork, foamed rubber, polystyrene, polyethylene, polyurethane, poly-isocyanurate and other polymers.

Various routes are available to suit lightweight production, one of such chemicals to generate gas within the mixture is metallic aluminium powder, which is very reactive in alkaline environments, such as calcium hydroxide or alkaline hydroxides; the aluminium dissolves as aluminate Al_2O^- and H_2 gas is liberated and trapped within the cementitious paste or mortar, expanding and increasing the volume. In order to prevent the escape of the gas, the paste must have a proper consistency and fast setting times according to the following reaction [21,22]:

$4Al + OH^- + H_2O \rightarrow 2Al_2O^- + 3/2\ H_2$

Another low cost material for lightweight production and available in greater quantities is aluminium slag (dross) acts which incorporates air into the mixture and can be used in the manufacturing of building blocks (bricks), pre-molded panels, subfloors and other kinds of surfaces. Approximately, up to 4 million tons of white dross and more than a million tons of black dross are reported throughout the world each year, and around 95% of this material is landfilled [23, 24].

This material also can be used raw materials in cement production industry as proved by *Puertas* et al. [25] as well as *Pereira* et al. [26] who explored partial replacement of aluminium dross to cement mortar in certain limits to obtain environmental and economic advantages. Others recommended the usage of aluminium dross as filler in concrete bricks and non-aerated concrete [27].

The objective of this contribution is to investigate the effect of aluminium powder and aluminium slag into the geopolymer composites as gas liberating agent and producing lightweight geopolymer structures. The other target is to study the effect of added materials on the hardened composites by monitoring their impacts on physico-mechanical and microstructural characteristics. X-ray diffraction and FTIR are used for investigation of the resulted composite structure.

2. Experimental procedures

2.1. Materials

Materials used were ground granulated blast furnace slag (GGBFS) sourced from Iron and Steel Factory - Helwan, Egypt, and kaolinite sand material brought from Middle East for Mining Investment Co., Egypt. Materials used for production of lightweight composites were aluminium slag procured from Nagh Hammadi Factory for aluminium production, Egypt, where it produced from recovery of aluminium through scrap recycling, where a great quantity of oxide layer formed on the surface of molten metal and has to be removed from the melt to refine the quality of the final product. This material has dual effect in geopolymer composite formation; one is the participation in the geopolymer formation as it contains both alumina and silicon oxides, the second is the very high active alumina content which acts as initiator for lightweight products.

Aluminium powder (Adwic chemicals, Egypt, 94% of purity) used as hydrogen gas liberating materials for geopolymer composites. Sodium hydroxide (NaOH) with purity 99 % in the form of pellets used as alkali activators, obtained from Piochem Co., Egypt, while liquid sodium silicate (LSS, Na_2SiO_3. $9H_2O$) from Fisher company consists of 32% SiO_2 and 17% Na_2O with Silica modulus SiO_2/Na_2O equal 1.88 and its density is 1.46 g/cm^3.

Chemical compositions of the starting raw materials are illustrated in Table 1, whereas the mineralogical characterization was done using X-ray diffraction analysis as represented in (*Fig. 1*). Blast furnace slag is a rich aluminosilicate material and composed from the dominant content of SiO_2, CaO, Al_2O_3 Fe_2O_3, and MnO as illustrated from *Table 1*, while its mineralogical structure revealed the amorphous nature of this material.

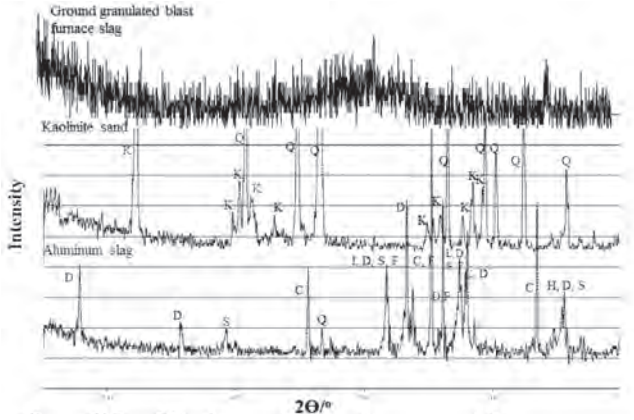

Fig. 1. X-Ray diffraction pattern of the starting raw materials [K=Kaolinite; Q=Quartz; D=Diaoyudaoite, syn ($Na_{1.22}Al_{11}O_{17.11}$); S=Spinel, syn ($Mg_{0.35}Al_{0.65}$)($Al_{1.78}$)$O_4$; C=Corundum ($Al_2O_3$); L=Lime (CaO); F=Fayalite magnesian ($Mg_{0.75}Fe_{1.10}Mn_{0.15}SiO_4$); H=Halite (NaCl)]

1. ábra Alapanyagok röntgendiffraktogramjai [K=Kaolinit; Q=Kvarc; D=Diaoyudaoit ($Na_{1.22}Al_{11}O_{17.11}$); S=Spinell, ($Mg_{0.35}Al_{0.65}$)($Al_{1.78}$)$O_4$; C=Korund ($Al_2O_3$); L=Égetett mész (CaO); F=Fayalit magnézia ($Mg_{0.75}Fe_{1.10}Mn_{0.15}SiO_4$); H=Halit (NaCl)]

Kaolinite sand showed that it has about 27% aluminium oxide as well as 64.5% of silicon oxide, in addition to little amount of calcium and magnesium oxides as presented in *Table 1*, however the mineralogical composition showed that kaolinite sand composed of about 75% quartz in addition to 25% kaolinite as shown in *Fig. 1*, the figure reflected also the crystalline nature of aluminium slag where most of its minerals are reach in alumina as Diaoyudaoite, Fayalite, spinel and corundum.

Material	SiO_2	Al_2O_3	Fe_2O_3	CaO	MgO	SO_3	K_2O	Na_2O	TiO_2	MnO_2	P_2O_5	Cl-	L.O.I.	SrO	BaO	Total
Kaolinitic sand	64.5	26.90	0.28	1.28	0.37	0.34	0.07	0.11	1.11	0.01	0.22	0.07	4.34	-	-	99.60
Ground granulated blast furnace slag (GGBFS)	36.67	10.31	0.50	38.82	1.70	2.17	1.03	0.48	0.57	4.04	0.04	0.05	0.12	0.18	3.28	99.96
Aluminia slag	14.52	76.15	0.60	2.39	3.15	0.19	0.36	2.37	0.02	0.00	0.01	-	-	-	-	99.75

Table 1. Chemical composition of starting materials (m%)

1. táblázat Alapanyagok kémiai összetétele (m%)

Mix no.	Water cooled slag (WCS), %	Kaolinite sand, %	Al-slag, %	Al-powder, %	NaOH, %	Sodium silicate, %	Water/binder
A0	50	50	-	0.0000	3	3	0.25
A1	50	50	-	0.0125	3	3	0.25
A2	50	50	-	0.0250	3	3	0.25
A3	50	50	-	0.0375	3	3	0.25
A4	50	50	-	0.0500	3	3	0.25
A5	50	50	-	0.0625	3	3	0.25
A6	50	50	-	0.0750	3	3	0.25
AS1	50	50	1	-	3	3	0.225
AS2	50	50	2	-	3	3	0.25
AS3	50	50	3	-	3	3	0.275
AS4	50	50	4	-	3	3	0.288

Table 2. Composition of the geopolymer mixes
2. táblázat Geopolimer keverékek összetétele

2.3. Geopolymerization and curing

Geopolymer were set by mixing raw materials (passing 90 μm sieve) of each mixture with the alkaline solution as represented in *Table 2* for 15 min with an electronic mixer. Aluminium powder was added to the binding material in small ratios from 0.0125 up to 0.075% with the increment of 0.0125% from the total weight; whereas aluminium slag was added in the ratio from 1 up to 4% from the total weight. The used aluminium materials mixed well with the total water incorporated the added activators for better production of foaming materials. All mixes were left to cure undisturbed under ambient temperature for 24 hrs, and then subjected to curing temperature of 40 °C with a 100 % relative humidity. At the end of curing regime, specimens were removed from their curing condition, dried well at 80 °C for 24 hrs then subjected to compressive strength measurements whereas the resulted crushed specimens were subjected to stopping of the hydration process by methyl alcohol/acetone method [28, 29] in order to prevent further hydration and then preserved in a well tight container until the time of testing.

2.4. Methods of investigation

Chemical composition of the started raw materials were performed using Axios, WD-XRF Sequential Spectrometer (Panalytical, Netherland, 2009). Compressive strength tests were performed according to ASTM-C109 [30] using German Brüf pressing machine. XRD analysis was carried out using Philips PW3050/60 Diffractometer. Microstructure of hardened materials was examined using FEI-SEM Inspect S equipped with an energy dispersive X-ray analyzer (EDX). Amorphous structure was traced using FTIR using potassium bromide binder, whereas their range from 400 to 4000 cm^{-1}[31, 32].

Water absorption measurements of the bricks were carried out according to ASTM C140 [33]. The percentage absorption was calculated using the equation:

Absorption (%) = [(W2 – W1)/ W1] ×100

whereW1 = weight of specimen after complete drying at 105°C, W2 = final weight of surface dry sample after immersion in water for at least 24 hours.

The bulk density is calculated according to Archimedes, principle as in the following equation [34,35]:

Bulk density = D/ (W-S) g.cm-3

Where;

D = weight of dried specimens

W = weight of soaked specimen suspended in air

S = weight of suspended specimens in water

3. Results and discussion

3.1. Effect of aluminium powder

FTIR spectra of neat geopolymer composite without aluminium powder cured up to 90 days are shown in *Fig. 2*. It can be noticed a decrease in kaolinite peaks beyond 3600 cm^{-1} with time as a results of continuous dissolution and polymerization of residual kaolinite forming additional geopolymer constituents leading to an increased reinforcement of the matrix, this confirmed by an increased intensity of the asymmetric stretching vibration (Ti–O–Si) at about 1000 cm^{-1} where T=Si or Al, as resulted from the increased geopolymerization and precipitation, this occur in conjunction with an increased intensity of symmetric stretching vibration (Al–O–Si) at about 780 cm^{-1} as well as symmetric stretching vibration (Si–O–Si) at about 670-685 cm^{-1}. Also, regions close to 460 cm^{-1} attributed to angular deformations of SiO_4 tetrahedrons (O-Si-O), as well as asymmetric stretching vibration for Si-O-Si (for non-solubilized particles) probably associated with quartz [36], these results are similar to those obtained by *Palomo* et al. [37]. Stretching vibration for Al-OH at about 910 cm^{-1} resulted from free unreacted aluminium species decreased also with time as unreacted free alumina exposed to dissolution and polymerization with time [38].

It can be noticed a shift in the wave number of main asymmetric band to right with an increased intensity up on time reflecting the increase of vitreous content which agrees with the observation that the incorporation of kaolinite within the sand retards polymerization reaction in the very early period of reaction [39, 40], while at later ages an increased dissolution of Al from kaolinite sand leading to an enhancing polymerization and modifying the chemistry of the Si–O–T bonds (giving a decrease in the wavenumber) [39, 40]

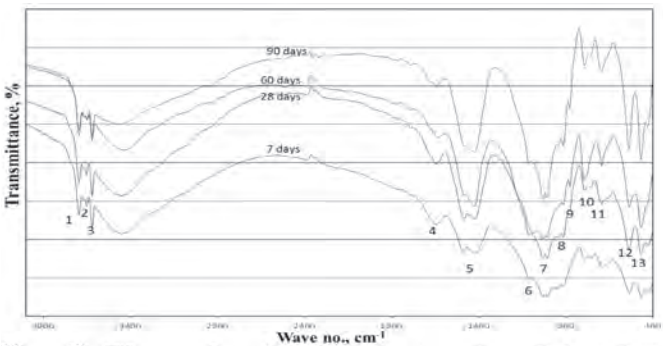

Fig. 2. FTIR spectra of control geopolymer cured up to 90 days in 40 °C with 100% R.H.) [1,2,3: Stretching vibration of O-H bond for kaolin; 4: Bending vibrations of (HOH); 5: Stretching vibration of CO_3; 6: Asymmetric stretching vibration (Si-O-Si); 7: Asymmetric stertching vibration (T-O-Si); 8: Symmetric stretching vibration of Al-OH; 9: Symmetric stretching vibration of CO_3; 10: Symmetric stretching vibration (Al-O-Si); 11: Symmetric stretching vibration (Si-O-Si); 12,13: Bending vibration (Si-O-Si and O-Si-O)]

2. ábra 90 napos korú (40 °C, 100% RH) geopolimer keverékek FTIR spektrumai [1,2,3: Vegyértékrezgés O-H kötés (kaolin); 4: Deformációs rezgés (HOH); 5: Vegyértékrezgés (CO_3); 6: Aszimmetrikus vegyértékrezgés (Si-O-Si); 7: Aszimmetrikus vegyértékrezgés (T-O-Si); 8: Szimmetrikus vegyértékrezgés (Al-OH); 9: Szimmetrikus vegyértékrezgés (CO_3); 10: Szimmetrikus vegyértékrezgés (Al-O-Si); 11: Szimmetrikus vegyértékrezgés (Si-O-Si); 12,13: Deformációs rezgés (Si-O-Si és O-Si-O)]

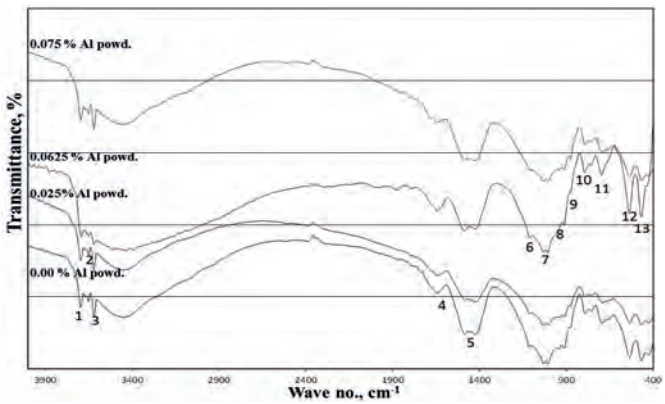

Fig. 3. FTIR spectra of 28 days lightweight geopolymer composite having various doses of aluminium powder [1,2,3: Stretching vibration of O-H bond for kaolin; 4: Bending vibrations of (HOH); 5: Stretching vibration of CO_3; 6: Asymmetric stretching vibration (Si-O-Si); 7: Asymmetric stertching vibration (T-O-Si); 8: Symmetric stretching vibration of Al-OH; 9: Symmetric stretching vibration of CO_3; 10: Symmetric stretching vibration (Al-O-Si); 11: Symmetric stretching vibration (Si-O-Si); 12,13: Bending vibration (Si-O-Si and O-Si-O)]

3. ábra 28 napos korú könnyű geopolimer kompozitok FTIR spektrumai különböző mennyiségű alumínium por adagolás mellett [1,2,3: Vegyértékrezgés O-H kötés (kaolin); 4: Deformációs rezgés (HOH); 5: Vegyértékrezgés (CO_3); 6: Aszimmetrikus vegyértékrezgés (Si-O-Si); 7: Aszimmetrikus vegyértékrezgés (T-O-Si); 8: Szimmetrikus vegyértékrezgés (Al-OH); 9: Szimmetrikus vegyértékrezgés (CO_3); 10: Szimmetrikus vegyértékrezgés (Al-O-Si); 11: Szimmetrikus vegyértékrezgés (Si-O-Si); 12,13: Deformációs rezgés (Si-O-Si és O-Si-O)]

On investigating the effect of addition of various ratios of aluminium powder up to 0.075% cured at 28 days (*Fig. 3*), first there is a slight decrease in the main asymmetric band up on adding 0.025% aluminium as a results of alteration in the Si/Al ratio, however a gradual increase in the band intensity with shifting to right can be recognized with increasing the aluminium powder up to 0.0625% where the added alumina results in enhancing the degree of polymerization by the effect of seeded nucleation results in the formation of nucleation sites for geopolymer formation and precipitation which positively enhance the resulted geopolymer structure [41], also this shift indicating the formation of a new product (the amorphous aluminosilicate gel phase) [31]. However, further increase in the aluminium powder results in an increase of liberated hydrogen gas as mentioned previously up on reacting with alkali, this gas results in an increased porosity as well as hinder interaction between binding materials leading to a lowering in intensity of the main asymmetric band with increased intensity of kaolinite bands reflecting low dissolution rate of the kaolinite precursor as compared with the lower aluminium powder ratio, additionally carbonate bands at about 1440 and 870 cm^{-1}, these bands exposed to an increased intensity with aluminium powder up to 0.0625 % then decreased up on using 0.075% aluminium powders which can be linked by the behaviour of asymmetric vibration of T-O-Si as hydrogen gas which hinder intact between reacting particle leads to lowering in carbonation rate of geopolymer composites at higher aluminium powder ratio.

Fig. 4 shows the XRD pattern of 28 days alkali activated geopolymer composites incorporating various ratios of aluminium powder, where a gradual increase in the amorphous geopolymer constituents with aluminium powder up to 0.0625% as represented by increased broadness with peak distortion between 20-35° 2θ characterizing glassy phase of geopolymer constituents, however this broadness decreased with further aluminium increase as well as up on using lower doses as come in coincide with FTIR. The increased intensity of amorphous constituents by formation of new phases come in alignment with the increased broadness in the range from 6-10° 2θ for aluminosilicate gel, where this increase reflects the increased dissolution of geopolymer precursor [42].

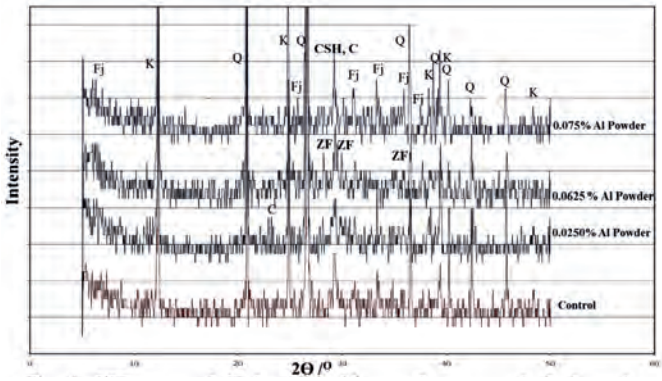

Fig. 4. XRD pattern of 28 days lightweight geopolymer composite having various aluminium powder ratios [K=Kaolinite; Q=Quartz; Fj: Faujasite; CSH: Calcium silicate hydrate; ZF: Zeolite Na-F]

4. ábra 28 napos korú könnyű geopolimer kompozitok röntgendiffraktogramjai különböző mennyiségű alumínium por adagolás mellett [K=Kaolinit; Q=Kvarc; Fj: Faujasit; CSH: Kalcium szilikát hidrát; ZF: Zeolit Na-F]

Another more likely reason is that the unique conditions in the early stages of seeded geopolymer formation by Al substitutes that may have created an environment where zeolite Na–F was able to be directly synthesized by hydrothermal treatment of kaolinite or metakaolin at relatively low temperatures (~80 °C) [43, 44]. These phases his Al-rich gel, which does not occur in the unseeded system, also explains the formation of Na–F [45]. On further increase in alumina powder; there is an intense peak for Faujasite of zeolite favoured the lower geopolymer characteristic as known by their lower branching ability, the

previous notice comes in accordance with Zuhua et al. [46], where the crystalline zeolite phases are destructive to the consistent distribution of geopolymers.

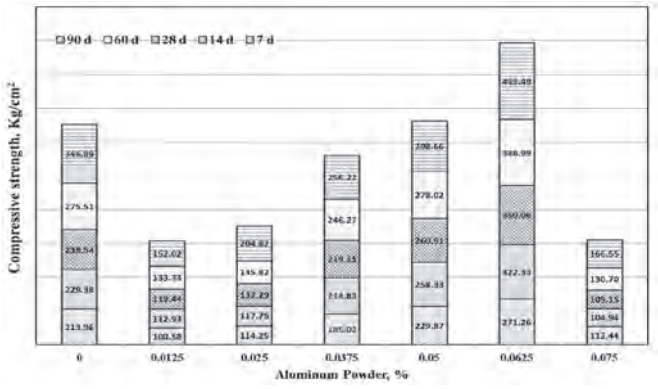

Fig. 5. Compressive strength of lightweight geopolymer composite having various aluminium powder ratios, cured up to 90 days
5. ábra 90 napos korú könnyű geopolimer kompozitok nyomószilárdsága különböző mennyiségű alumínium por adagolás mellett

The results of compressive strength and absorption as well as bulk density for hardened geopolymer composite incorporated various ratio of aluminium powder, cured in 100 % relative humidity at 40°C up to 90 days are shown in *Figs. 5-6*. The results showed an increase in strength for all mixes along with hydration age as attributed to the continuing pozzolanic reaction as well as continuous growth of geopolymer chains forming tightly bound structure. Dissolving aluminium powder with its high reactivity in alkaline environment transforming into aluminate species and giving off free hydrogen gas. The aluminate species can promote the reaction by the effect of seeded nucleation as mentioned latter and enhance propagation as well as precipitation of geopolymer chains, while the liberated gas can facilitate the formation of lightweight composites with lower density as compared with common building materials units.

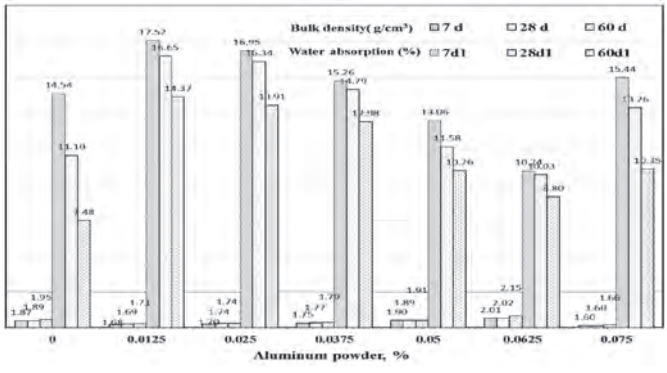

Fig. 6. Bulk density and water absorption of lightweight geopolymer composite having various aluminium powder ratios
6. ábra Könnyű geopolimer kompozitok testsűrűsége és vízfelvétele különböző mennyiségű alumínium por adagolás mellett

There is a sharp strength decrease can be elucidated from the figure with the addition of 0.0125% aluminium, as explained from both FTIR and XRD as the alteration in Si/Al ratio lead to a decrease in strength. Increasing the ratio of the added alumina, results in a gradual increase in strength, reaching the maximum values at 0.0625% followed by rapid decrease with further alumina increase. The strength increase can be explained by the increased asymmetric stretching vibration of amorphous glassy geopolymer phases at about 1000 cm^{-1} where the seeded nucleation effect of the liberated aluminate enhanced the nucleation and geopolymerization of reacting materials, forming zeolite Na-F which known by its ability to strengthen the structure. However, further increase in the aluminium powder results in an extra increase in the liberated hydrogen gas which compensate the activation role of aluminate species by absorption increase and so hinder interaction between the reacting species and so lower the intensity of the formed geopolymer as well as strength

We can notice that the strength values were 214.0, 271.0, 112.4 kg/cm² at 7 days and 239.5, 350.0, 109.1 kg/cm² at 28 days for 0, 0.0625, 0.075 % aluminium powder, respectively, however the density values are 1.874, 2.010,1.599 g/cm³ at 7 days and 1.886, 2.016, 1.598 g/cm³ at 28 days for the same ratios. Strength pattern also shows that values of the formed green composite incorporating 0.0625 % aluminium powder are much harder than OPC cement according to ASTM C150 [47] where its standard strength values are 200 and 294 kg/cm² at 7 and 28 days, whereas the produced lightweight product with the previously mentioned ratio is much harder in addition to its low production cost as most of the used materials are wastes, however cement uses primary raw materials.

It was recognized that lightweight concrete can be classified according to the purpose of utilizing as: 1) structural lightweight concrete with cylinder compressive strength at 28 days equal or more than 17 MPa and the approximate density range 1400-1800 kg/m³ 2) masonry concrete (structural / insulating lightweight concrete) has a compressive strength between 7-14 MPa and density range 500-800 kg/m³ 3) insulating concrete has a compressive strength between 0.7-7 MPa and density lower than 800 kg/m³ [48, 49].

So the produced product can be used effectively in the production of high-strength lightweight concrete with strength values (20 to 35 MPa). On the other hand lightweight structural concrete is required under European standards to have and density of less than 2000 kg/m³ (2.0 g/cm³), where most of the studied composites have density values ≤ 2.0 g/cm³ at all curing ages which reflects the lightweight characteristics of composites.

Fig. 7. a, shows the typical microstructure of 90 days control geopolymer matrix free from aluminium powder, this matrix exhibits dense morphology with spreading unreacted kaolinite laminar in addition to geopolymer networks which come in accordance with kaolinite bands in FTIR chart. On adding 0.0625% Al powder (*Fig. 7. b*), an increased dissolution of kaolinite constituent observed as shown from the matrix nearly free from kaolinite laminas which conform the seeding nucleation effect of added alumina leading to modification of the resulted geopolymer by an increased intensity, this can be illustrated clearly from the cohesion of the formed matrix. Another role of the added alumina is to form lightweight composite by releasing free hydrogen gas by alkaline interaction; this confirmed by the micropores within reacted particles. On increasing aluminium powder to 0.075%

an increased liberation of hydrogen gas noticed from the formation of wide pores within the matrix, this will adversely inhibit the intact between formed geopolymer networks and so lower their mechanical properties (*Fig. 7. c*).

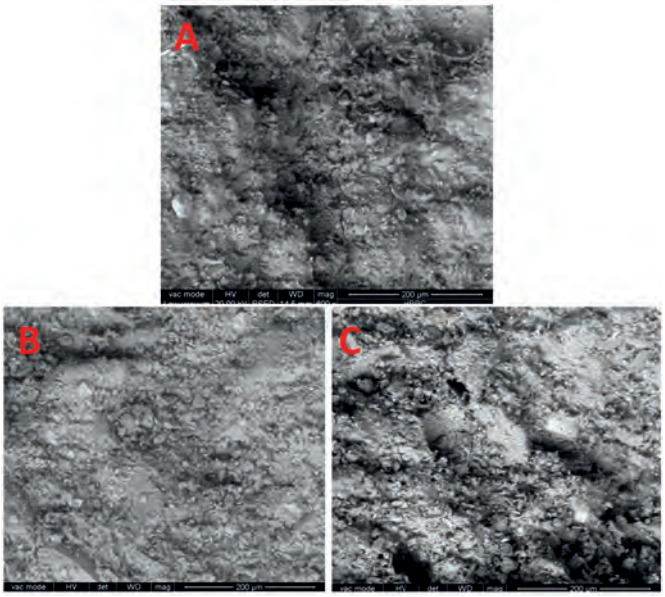

Fig. 7. SEM images of 90 days lightweight geopolymer composite having various aluminium powder ratios [A: 0%; B: 0.0625%; C: 0.075%]

7. ábra 90 napos korú könnyű geopolimer kompozitok elektronmikroszkópos felvételei különböző mennyiségű alumínium por adagolás mellett [A: 0%; B: 0.0625%; C: 0.075%]

3.2. Effect of aluminium slag

On studying the effect of aluminium slag using FTIR for 28 days geopolymer composites incorporating various aluminium slag ratio up to 4% (*Fig. 8*), there is a marked decrease in the main asymmetric band with the addition of 1% aluminium slag as a results of alteration in the Si/Al ratio, whilst there is a progressing increase in the asymmetric band with slight shifting to right by increasing aluminium slag to 3% where the used slag results in modification of the geopolymer structure and formation of vitreous content [41], also shifting of the band to lower wave number favours the increased amorphous gel phase as stated before [31]. On prolonged investigation of the pattern there is a growth in carbonate band with aluminium slag (3%) which can be considered as beneficial in formation of cellular composite as compared with aluminium powder in spite the strength is lower than that of aluminium powder.

Increasing aluminium slag to 4%, results in the increase of crystalline minerals associated with aluminium slag which adversely hinder geopolymerization reaction in addition to diverse effect of hydrogen gas in increased porosity and so hinder the interaction between reacting particles as reflected on the decreased intensity of the main asymmetric band.

The pattern clarified the fixed intensity of kaolinite bands beyond 3600 cm^{-1} which may be due to the lower efficiency of aluminium slag in enhancing geopolymerization reaction as compared with aluminium powder. There is an additional notice about carbonate bands at about 1440 and 870 cm^{-1}, these bands decreased up on using 1 % aluminium slag while increased again with 3 % aluminium slag and then exposed to sharp decrease with further increase in Al-slag. This can be linked by the behaviour of asymmetric vibration of T-O-Si as hydrogen gas which hinder intact between reacting particles leads to lowering in carbonation rate of geopolymer composites at higher aluminium slag (4%).

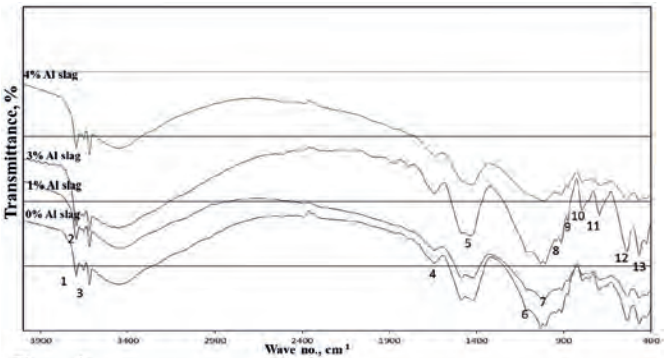

Fig. 8. FTIR spectra of 28 days lightweight geopolymer composite having various doses of aluminium slag [1,2,3: Stretching vibration of O-H bond for kaolin; 4: Bending vibrations of (HOH); 5: Stretching vibration of CO_3; 6: Asymmetric stretching vibration (Si-O-Si); 7: Asymmetric stertching vibration (T-O-Si); 8: Symmetric stretching vibration of Al-OH; 9: Symmetric stretching vibration of CO_3; 10: Symmetric stretching vibration (Al-O-Si); 11: Symmetric stretching vibration (Si-O-Si); 12,13: Bending vibration (Si-O-Si and O-Si-O)]

8. ábra 28 napos korú könnyű geopolimer kompozitok FTIR spektrumai különböző mennyiségű alumínium salak adagolás mellett [1,2,3: Vegyértékrezgés O-H kötés (kaolin); 4: Deformációs rezgés (HOH); 5: Vegyértékrezgés (CO_3); 6: Aszimmetrikus vegyértékrezgés (Si-O-Si); 7: Aszimmetrikus vegyértékrezgés (T-O-Si); 8: Szimmetrikus vegyértékrezgés (Al-OH); 9: Szimmetrikus vegyértékrezgés (CO_3); 10: Szimmetrikus vegyértékrezgés (Al-O-Si); 11: Szimmetrikus vegyértékrezgés (Si-O-Si); 12,13: Deformációs rezgés (Si-O-Si és O-Si-O)]

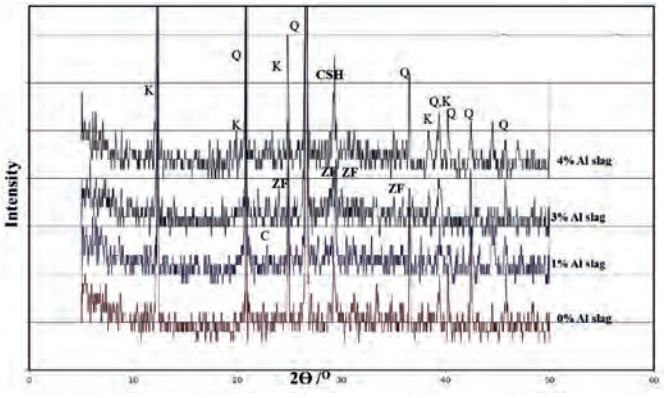

Fig. 9. XRD pattern of 28 days lightweight geopolymer composite having various aluminium slag ratios [K=Kaolinite; Q=Quartz; CSH: Calcium silicate hydrate; ZF: Zeolite Na-F; C: Calcite]

9. ábra 28 napos korú könnyű geopolimer kompozitok röntgendiffraktogramjai különböző mennyiségű alumínium salak adagolás mellett [K=Kaolinit; Q=Kvarc; CSH: Kalcium szilikát hidrát; ZF: Zeolit Na-F; C: Kalcit]

Fig. 9 shows the XRD pattern of 28 days geopolymer composites incorporating various aluminium slag ratio, where there is a similarity between this pattern and those for aluminium powder pattern as a gradual increase in the amorphous geopolymer constituents with increase of aluminium slag up to 3%, observed as well as an increased broadness in the range between 20-35° 2θ for amorphous geopolymer constituents, while the main difference between them is an increased Faujasite up on using higher aluminium powder. However, this is not the case in aluminium slag mixes having higher ratio (4%) where no Faujasite formed as the

increased crystalline phases in slag constituents hinder the reaction and so a lower intensity of both asymmetric stretching as well as Faujasite, this in coincide with the low dissolution rate of kaolinite constituents.

On investigating compressive strength, density and water adsorption results for hardened geopolymer composite incorporated various ratio of aluminium slag, cured up to 90 days (Figs. 10-11), there is an analogous behaviour to that of aluminium powder where a gradual increase with time as well as with aluminium slag up to 3 % but still lower than that of control mix as a results of lower efficiency of aluminium slag in enhancing the reaction.

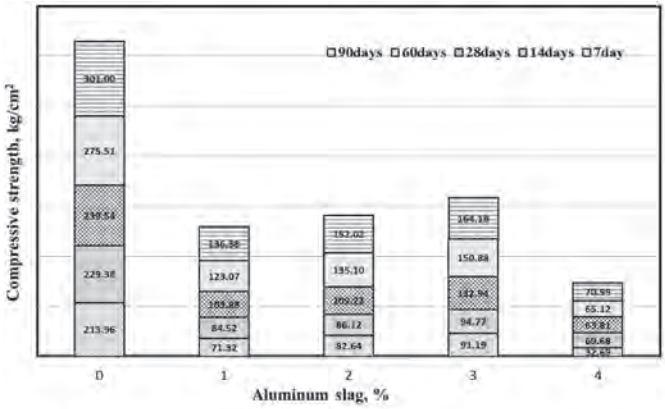

Fig. 10. Compressive strength of lightweight geopolymer composite having various aluminium slag ratios, cured up to 90 days

10. ábra 90 napos korú könnyű geopolimer kompozitok nyomószilárdsága különböző mennyiségű alumínium salak adagolás mellett

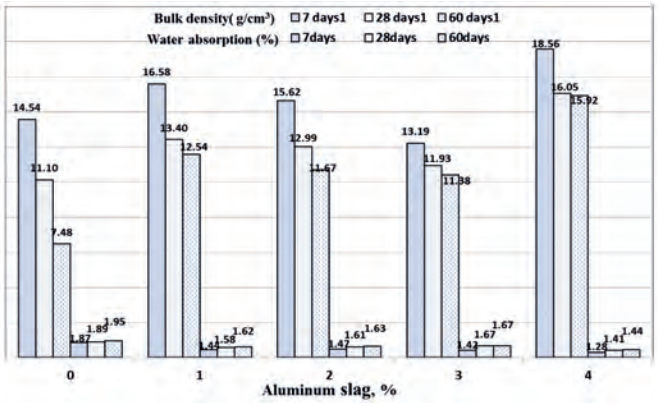

Fig. 11. Bulk density and water absorption of lightweight geopolymer composite having various aluminium slag ratios

11. ábra Könnyű geopolimer kompozitok testsűrűsége és vízfelvétele különböző mennyiségű alumínium salak adagolás mellett

First, strength decreases sharply upon using 1% slag precursor as a results of alteration of silica to alumina ratio, whereas strength increases with further aluminium slag to 3% as illustrated in details before about the efficiency of aluminium species in activating the reaction by seeding nucleation principle, while the liberated gas can facilitate the formation of lightweight composites with lower density as compared with common building materials units. On further increase in aluminium slag to 4%, strength decreases again as the intensity of zeolite F decreased which known by its ability to enhance the formed structure, in addition to decreased intensity of asymmetric geopolymer band in FTIR pattern, where the increased aluminium slag with its crystalline constituents hinder the formation of geopolymer chains as well as increased liberated gases decreased strength sharply by isolation of the interacting particles.

On comparing with strength values of aluminium powder specimens, a lower strength values of Al-slag species as compared with aluminium powder as related to the lower reactivity of aluminium slag and its crystalline structure. The strength values were 214.0, 91.2, 32.7 kg/cm^2 at 7 days and 239.5, 133, 63.8 kg/cm^2 at 28 days for 0, 3, 4 % aluminium slag, respectively, however the density values are 1.874, 1.417,1.275 g/cm^3 at 7 days and 1.886, 1.665, 1.406 g/cm^3 at 28 days for the same ratios. Whereas the absorption values are 14.54, 13.19, 18.56 % at 7 days and 11.10, 11.93, 16.05 % at 28 days as illustrated in Fig. 11.

An important conclusion is that the strength values of the formed geopolymer composite incorporating 0.0625% aluminium powder are much harder than aluminium slag, however from the point of view of lightweight principles; the density of the Al-slag species are lower than that of aluminium powder composites while the water absorption values are higher, which can be considered as a very important from the point of view of lightweight composites as the density is lower by about one third and the absorption higher by about the same ratio.

On classifying aluminium slag composites according to previously mentioned classification [48, 49], they can be suitable for masonry concrete (structural / insulating lightweight concrete) which has a compressive strength between 7-14 MPa and density range 500-800 kg/m^3, as well as insulating concrete has a compressive strength between 0.7-7 kg/m^3 and density lower than 800 kg/m^3.

On comparing the morphology of cellular geopolymer composites incorporating aluminium powder and aluminium slag; a clear difference between their microstructure observed where the 3% aluminium slag (*Fig. 12.a*) enhanced composite shows low cohesion between their matrix as well as spreading of unreacted kaolinite within its morphological structure, this reflecting low enhancing ability of aluminium slag for activation and nucleation of geopolymer precursors as coincided by their low mechanical characteristics as compared with optimum aluminium powder enhanced geopolymer mix (*Fig. 12.b*) which possess dense structure with little evidence of unreacted kaolinite.

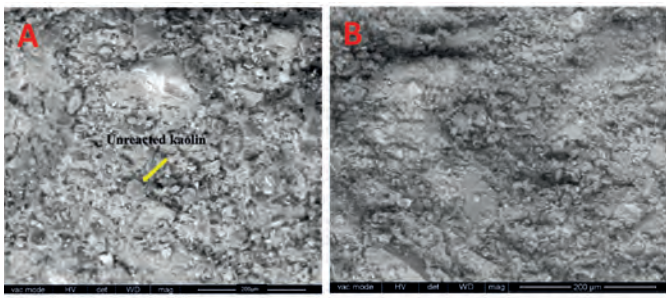

Fig. 12. SEM images of 90 days lightweight geopolymer composite doped with A: 3% Al slag; B: 0.0625% Al powder

12. ábra 90 napos korú könnyű geopolimer kompozitok elektronmikroszkópos felvételei A: 3% Al salak; B: 0.0625% Al por

4. Conclusions

The paper deals with incorporation of aluminium substituents as hydrogen gas emitting materials for lighting the density of the resultant geopolymer composites, while the raw materials for the base geopolymer mixes made from waste materials for lowering the production costs, there are some important findings that can be concluded from the present paper:

Aluminium powder and aluminium slag can be used efficiently in production of lightweight geopolymer materials resulting in low density composites as compared with most common lightweight materials, where density of most cement concrete was 2.2 to 2.60 g/cm^3.

Aluminium powder can be used up to 0.075% with acceptable properties and with density values ≤ 2.0 g/cm^3 and decreased with aluminium substituents increase, while 0.0625 % can possess both high mechanical and morphological advantages with densities in the same previous range whereas their 28 strength values exceeds 350 kg/cm^2 which can be used effectively in the production of high-strength lightweight concrete.

Aluminium slag materials can be used without significant loss in the mechanical and physical properties up to 4%, while using 3% possess optimum mechanical characteristics with density values lower than 1.70 g/cm^3.

In spite strength values of Al- slag species are lower than aluminium powder, their density values are lower and absorption are higher by about one third, which encourage its beneficial use in lightweight production.

References

[1] Pinto, S. – Almeida, M. – Correia, A. M. S. – Labrincha, J. A. – Ferreira, V. M. – Rosenbom, K. (2004): Use of recycled materials in buildings and structures. *Proceedings of International RILEM Conference on the use of recycled materials in buildings and structures*, 2004, 2: 771-777.

[2] Dondi, M. – Marsigli, M. – Fabbri, B. (1997): Recycling of urban and industrial wastes in brick production: a review. *Tile & Brick International*, 1997, 13(4): 302-315.

[3] Tay, J. H. – Show, K. Y. – Hong, S. Y. (2001): Reuse of industrial sludge as construction aggregates. *Water Science Technology*, 2001, 44 (10): 269-272. https://doi.org.10.2166/wst.2001.0638

[4] Davidovits, J. (2002): 30 Years of Successes and Failures in Geopolymer Applications. Market Trends and Potential Breakthroughs, *Geopolymer 2002 Conference*, October 28–29, 2002, Melbourne, Australia.

[5] Davidovits, J. (1989): Geopolymers and geopolymeric materials, *Journal of Thermal Analysis*, 1989, 35:425–441. https://doi.org/10.1007/BF01904446

[6] Cheng, T. W. – Chiu, J. G. (2003): Fire-resistant geopolymer produced by granulated blast furnace slag, *Minerals Engineering*, 2003, 16:205–210. https://doi.org/10.1016/S0892-6875(03)00008-6

[7] Komnitsas, K. – Zaharaki, D. (2007): Geopolymerisation: a review and prospects for the minerals industry, *Minerals Engineering*, 2007, 20:1261-1277. https://doi.org/10.1016/j.mineng.2007.07.011

[8] Khale, D. – Chaudhary, R. (2007): Mechanism of geopolymerization and factors influencing its development, a review, *Journal of Materials Science,* 2007, 42:729-746. https://doi.org/10.1007/s10853-006-0401-4

[9] Duxson, P. – Van Deventer, J. (2009): Geopolymers, structure, processing, properties and applications. In: Provis J, Van Deventer J, editor. *Geopolymers, structure, processing, properties and applications,* Woodhead Publishing Limited Abington Hall, Cambridge, UK, 2009

[10] Weil, M. – Dombrowski, K. – Buchawald, A. (2009): Life-cycle analysis of geopolymers. In: Provis J, Van Deventer J, editor. *Geopolymers, structure, processing, properties and applications*, Woodhead Publishing Limited Abington Hall, Cambridge, UK, 2009

[11] Liyana, J. – Kamarudin, H. – Mustafa Al Bakri – A. M., Binhussain – M., Ruzaidi – C.M. Izzat, A.M. (2013) Reviews on Fly Ash based Geopolymer Materials for Protective Coating Field Implementations, *Australian Journal of Basic and Applied Sciences*, 2013, 7(5): 182-186.

[12] Lyon, R. E. (1996): Fire Response of Geopolymer Structural Composites, DOT/FAA/AR-TN95/22/1996.

[13] Khater, H. M. (2014): Studying the Effect of Thermal and Acid Exposure on Alkali Activated Slag Geopolymer, *Advances in Cement Research,* 2014, 26(1):1–9. https://doi.org/10.1680/adcr.11.00052

[14] Davidovits, J. (1999) In: Proc. Int. Conf. Geopolymer , France, 1999: 9.

[15] Omar, A. A. – Mustafa Al Bakri, A.M. – Kamarudin, H. – Khairul Nizar, I. – Saif, A.A. (2014): Effects of elevated temperatures on the thermal behavior and mechanical performance of fly ash geopolymer paste, mortar and lightweight concrete, *Construction and Building Materials,* 2014, 50:377-387. https://doi.org/10.1016/j.conbuildmat.2013.09.047

[16] Pinto, S. – Almeida, M. – Correia, A. M. S. – Labrincha, J. A. – Ferreira, V. M. – Rosenbom, K. (2004): Use of recycled materials in buildings and structures. *Proceedings of International RILEM Conference on the use of recycled materials in buildings and structures*, Vol. 2 (2004), pp. 771-777.

[17] Arellano Aguilar, R. – Burciaga Diaz, O. – Escalante Garcia, J. I. (2010): Lightweight concretes of activated metakaolin-fly ash binders, with blast furnace slag aggregates, *Construction and Building Materials*, 2010, 24:1166–1175. https://doi.org/10.1016/j.conbuildmat.2009.12.024

[18] Neville, A. M. (1995): Lightweight concrete. In: Properties of concrete, United Kingdom: Wiley, Prentice Hall, 1995: 688–715.

[19] Azimi, E. A. – Al Bakri Abdullah, M. M. – Ming, L. Y. – Yong, H. C. – Hussin, K. – Hakem Aziz, I. (2016): Processing and properties of geopolymers as thermal insulating materials: a review, *Reviews in Advanced Material Science*, 2016, 44:273-285.

[20] Snow, F. J. (1982): Thermal Infrared Sensing Applied to Energy Conservation in Building Envelopes, International Society for Optics and Photonics, 1982: 94.

[21] Bean, D. L. – Malore, P. G. (1997): United States patent 5605570.

[22] Vargel, C. (2004): Inorganic bases. In: Vargel, C., editor. Corrosion of aluminium. United Kingdom: Elsevier Science, 2004:385–93.

[23] Hollins, O. (2002): Aluminium industry could dramatically reduce landfilling of furnace, http://www.ohlsti.co.uk/ohl/newsletter/ohl_wmr312.pdf. Access date: 11.11.2007.

[24] Brough, M. (2002): Aluminium Lightens the Environmental Load, Vision-*The newsletter of the Foresight and Link Initiative*. Winter 2002. No 4. http://www.berr.gov.uk/files/file30193.pdf. Access date: 11.11.2007.

[25] Puertas, F. – Blanco-Varela, M. T. – Vazquez, T. (1999): Behaviour of cement mortars containing an industrial waste from aluminium refining stability in $Ca(OH)_2$ solutions, *Cement and Concrete Research*, 1999, 29:1673-1680. https://doi.org/10.1016/S0008-8846(99)00157-X

[26] Pereira, D. A. – Aguiar, B. – Castro, F. – Almeida, M. F. – Labrincha, J. A. (2000): Mechanical behaviour of Portland cement mortars with incorporation of Al-containing salt slags, *Cement and Concrete Research,* 2000, 30:1131-1138. https://doi.org/10.1016/S0008-8846(00)00272-6

[27] Brough, M. (2002): Aluminium Lightens the Environmental Load, *Vision-The newsletter of the Foresight and Link Initiative.* Winter 2002. No 4.

[28] Khater, H. M. (2013): Effect of cement Kiln dust on geopolymer composition and its resistance to sulfate attack, *Green Materials Journal.* 2013, 1(1):36-46. https://doi.org/10.1680/gmat.12.00003

[29] El-Sayed, H. A. – Abo El-Enein, S. A. – Khater, H. M. – Hasanein, S. A. (2011): Resistance of Alkali Activated Water Cooled Slag Geopolymer to Sulfate Attack, Ceramics – Silikáty. 2011, 55(2):153-160.

[30] ASTM C109M (2016): Standard Test Method for Compressive Strength of Hydraulic Cement Mortars

[31] Panias, D. – Giannopolou, L. P. – Peraki, T. (2007): Effect of synthesis parameters on the mechanical properties of fly ash-based geopolymers, *Colloids and Surfaces A: Physicochemical and Engineering Aspects*, 2007, 301:246-254. https://doi.org/10.1016/j.colsurfa.2006.12.064

[32] Bakarev, T. (2006): Thermal behavior of geopolymer prepared using class F fly ash and elected temperature curing, *Cement and Concrete Research,* 2006, 36:1134-1147. https://doi.org/10.1016/j.cemconres.2006.03.022

[33] ASTM C140 (2016): Standard test methods for sampling and testing concrete masonry units and related units

[34] Egyptian Standards (2015): Concrete Building Units Used in Non Load and Load Bearing Walls, *Egyptian Organization for Standardization,* Cairo, Egyptian Standards 1292-2, 1-11(2015).

[35] Ugheoke, B. I. – Onche, E. O. – Namessan, O. N. – Asikpo, G. A. (2006): Property Optimization of Kaolin - Rice Husk Insulating Fire – Bricks, *Leonardo Electronic Journal of Practices and Technologies*, 2006, 9, 167–178.

[36] Bakharev, T. (2005): Durability of geopolymer materials in sodium and magnesium sulfate solutions, *Cement and Concrete Research*, 2005, 35:1233-1246. https://doi.org/10.1016/j.cemconres.2004.09.002

[37] Palomo, A. – Grutzeck, M. W. – Blanco, M. T. (1999): Alkali-activated fly ashes: A cement for the future. *Cement and Concrete Research*, 1999, 29:1323-1329. https://doi.org/10.1016/S0008-8846(98)00243-9

[38] de Vargas, Alexandre Silva – Dal Molin, Denise C. C. – Masuero, Ângela B. – Vilela, Antônio C. F. – Castro-Gomes, Joao – de Gutierrez, Ruby M. (2014): Strength development of alkali-activated fly ash produced with combined NAOH and CA(OH)$_2$ activators, *Cement and Concrete Composites*, 2014, 53, 341-349. https://doi.org/10.1016/j.cemconcomp.2014.06.012

[39] Khater, H. M. – El Nagar, Abdeen M. – Ezzat, M. (2016): Alkali activated Eco-friendly Metakaolin/slag geopolymer building bricks, *Journal of Chemistry and Material Research*, Jan 2016, 8(1):21—32.

[40] Bernal, Susan A. – Provis, John L. – Rose, Volker – de Gutierrez, Ruby Mejía (2011): Evolution of binder structure in sodium silicate-activated slag-metakaolin blends. *Cement and Concrete Composites*, 33 (2011) 46–54. https://doi.org/10.1016/j.cemconcomp.2010.09.004

[41] Rees, Catherine A. – Provis, John L. – Lukey, Grant C. – van Deventer, Jannie S. J. (2008): The mechanism of geopolymer gel formation investigated through seeded nucleation, *Colloids and Surfaces A: Physicochemical and Engineering Aspects*, 318 (2008) 97–105. https://doi.org/10.1016/j.colsurfa.2007.12.019

[42] Temuujin, J. – van Riessen, A. – Williams, R. (2009): Influence of calcium compounds on the mechanical properties of fly ash geopolymer pastes, *Journal of Hazardous Materials*, 167(1–3), 2009, pp. 82–88. https://doi.org/10.1016/j.jhazmat.2008.12.121

[43] Rees, C. A. – Provis, J. L. – Lukey, G. C. – van Deventer, J. S. J. (2008): The mechanism of geopolymer gel formation investigated through seeded nucleation, *Colloids and Surfaces A: Physicochemical and Engineering Aspects*, 318 (2008) 97–105. https://doi.org/10.1016/j.colsurfa.2007.12.019

[44] Barrer, R. M. – Mainwaring, D. E. (1972): Chemistry of soil minerals. Part XIII. Reactions of metakaolinite with single and mixed bases, *Journal of the Chemical Society*, Dalton Transactions (1972) 2534. https://doi.org/10.1039/DT9720002534

[45] Provis, J. L. – Lukey, G. C. – van Deventer, J. S. J. (2005): Do geopolymers actually contain nanocrystalline zeolites? A re-examination of existing results, *Chemistry of Materials*. 17 (2005) 3075–3085. https://doi.org/10.1021/cm050230i

[46] Zuhua, Z. – Xiao, Y. – Huajun, Z. – Yue, C. (2009): Role of water in the synthesis of calcined kaolin-based geopolymer, *Applied Clay Science,* 2009, 43:218–23. https://doi.org/10.1016/j.clay.2008.09.003

[47] ASTM C150 (2016) Standard Specification for Portland cement

[48] Neville, A. M. – Brooks, J. J. (2010): Concrete Technology, 2nd edition, Prentice Hall, Pearson Education

[49] Slaby, A. A. – Aziz, K. I. – Hadeed, A. F. (2008): Mechanical Properties of Porcelinite Reinforced Concrete Beams, *Iraqi Journal of Civil Engineering*, Vol. 10, No. 10, pp. 1-24, 2008.

Ref.:
Khater, Hisham Mustafa Mohamed: *Preparation and characterization of lightweight geopolymer composites using different aluminium precursors*
Építőanyag – Journal of Silicate Based and Composite Materials, Vol. 70, No. 6 (2018), 186–194. p.
https://doi.org/10.14382/epitoanyag-jsbcm.2018.33

Microstructure and mechanical properties of TiN dispersed Si_3N_4 ceramics via in-situ nitridation of coarse metallic Ti

Sotaro BABA ▪ The Institute of Scientific and Industrial Research (ISIR), Osaka University ▪ babasou23@sanken.osaka-u.ac.jp
Tomoyo GOTO ▪ The Institute of Scientific and Industrial Research (ISIR), Osaka University ▪ goto@sanken.osaka-u.ac.jp
Sunghun CHO ▪ The Institute of Scientific and Industrial Research (ISIR), Osaka University ▪ shcho@sanken.osaka-u.ac.jp
Tohru SEKINO ▪ The Institute of Scientific and Industrial Research (ISIR), Osaka University ▪ sekino@sanken.osaka-u.ac.jp

Érkezett: 2018. 07. 15. ▪ Received: 15. 07. 2018. ▪ https://doi.org/10.14382/epitoanyag-jsbcm.2018.34

Abstract

Titanium nitride (TiN) was formed by in-situ reaction of coarse metallic titanium (Ti) and silicon nitride (Si_3N_4) powder mixtures through hot-press sintering. Mechanical properties of the prepared Si_3N_4/TiN composite were observed. The Si_3N_4 raw powder containing Al_2O_3 and Y_2O_3 as sintering additives and large metallic Ti powders were mixed by the ball mill and then hot-pressed under a pressure of 30 MPa at 1500 °C for 0.5 h with different heating rate. The obtained sintered body had a unique structure in which polycrystalline and porous large TiN grains were dispersed in a dense Si_3N_4 matrix. The sintered composites were densified over 95 %, however, they contained around 26-38% of β-phase of Si_3N_4, which value was lower than that of monolithic Si_3N_4 sintered under the same condition. Although the hardness and the Young's modulus of the composite slightly decreased from the monolithic Si_3N_4, the fracture toughness was improved due mainly to the dispersion of large-sized TiN grains. It was considered that the matrix and the additive elements, which penetrated and formed oxide phases inside as well as at the grain boundaries of porous TiN grains through the sintering, improved the bonding between the TiN particles and the matrix to suppress the decrease of the mechanical properties.

Keywords: silicon nitride, nitridation reaction, sintering, TiN, microstructure formation, mechanical properties
Kulcsszavak: szilíciumnitrid, nitridálási reakció, szinterelés, TiN, mikrostruktúra kialakulása, mechanikai jellemzők

Sotaro BABA
Graduated master course in Nagaoka University of Technology, Japan (2015) and obtained PhD in September 2018 from Osaka University under supervision of Prof. T. Sekino at the Institute of Scientific and Industrial Research (ISIR). He is Assistant Professor in Mie University since November 2018.

Tomoyo GOTO
Graduated in Nagoya University, Japan and has PhD since 2012. She is appointed in Kyushu University and National Institute of Advanced Industrial Science and Technology (AIST), and at present she is an Assistant Professor in Prof. Sekino's Laboratory of ISIR, Osaka University.

Sunghun CHO
Graduated in Sunmoon University, Korea and has PhD since 2015, and continues his research as a post-doctoral scholar there. He is Assistant Professor in Prof. Sekino's Laboratory of ISIR, Osaka University since 2015.

Tohru SEKINO
Professor of the Department of Advanced Hard Materials, the Institute of Scientific and Industrial Research (ISIR), Osaka University since 2014. He has over 300 peer-reviewed scientific publications and more than 30 patents. He was awarded with various prizes including the Prizes for Science and Technology by the Minister of Education, Culture, Sports, Science and Technology (MEXT) Japan (2016), and the Ceramic Society of Japan Awards for Academic Achievements (2016).

1. Introduction

Silicon nitride ceramics (Si_3N_4) has high strength, high toughness, low density, excellent high temperature strength, low dielectric constant and is the most important material for structural materials. In order to expand the range of further utilization of silicon nitride material, improvement of fracture toughness value lower than general metal material which is one of factors of lowering reliability is required. Si_3N_4/metal composites consisted of metal dispersions having excellent elasticity and Si_3N_4 matrix have been developed for improving the brittleness of ceramics. Among various metals, Titanium (Ti) is lightweight and has a relatively high melting point, and is used as a base for heat resistant alloys, shape memory alloys and so on.

By using these two kinds of materials, Si_3N_4 and Ti in combination, it might be used as structural material that is lightweight and excellent in heat resistance and oxidation resistance. In fact, as the combination of Si_3N_4 and Ti metal, an active metal joining method using a Ti-added brazing filler was reported [1]. However, there was a problem to generate stress concentration at the joint interface and resultant residual stress that degraded bonding two phases.

A functionally-graded material (FGM), in which composition of two phases was gradually changed, was developed as a new method to improve mechanical reliability and to maintain their properties possessed by both materials. This has been studied as a way to further development of heterogeneous composite materials as well as solving the problem of stress concentration and residual stress at the joint interface of dissimilar materials. For example, *Shinohara* et al [2] developed a coating having thermal stress relaxation function by gradually-changed composition of partially-stabilized zirconia (PSZ) ceramic and NiCrAlY alloy to suppress thermal barrier coating degradation due to thermal stress at the interface between super alloy and ceramic thermal barrier coating under high temperature. In addition, *Tsuda* et al [3] fabricated a functionally graded material in which a graded layer of Ti-based ceramics was formed on the surface of a cemented carbide and introduced a gradient of thermal expansion coefficient into the material. As a result, they reported improvement of abrasion resistance and defect resistance as a cutting tool material.

However, when considering the combination of Ti with Si_3N_4, Ti easily reacts with Si_3N_4 and/or N_2 gas atmosphere during sintering to transform into titanium nitride (TiN),

so that partial Si_3N_4/TiN composite material is formed [4]. Studies on Si_3N_4/TiN composites have been reported so far, but most of them are focusing on improving electrical conductivity for addition of electrical discharge machinability to Si_3N_4. *Ahmadet* et al [5] fabricated the sintered composites by spark plasma sintering (SPS) of raw powder mixtures of Si_3N_4, sintering aid (oxides) and Ti powder, and analyzed the crystallography and conductivity. As a result, they obtained Si_3N_4 composite with sufficiently high conductivity that applicable to the electrical discharge machining. *Huang* et al [6] also produced a hot press sintered Si_3N_4/TiN composites using the in-situ nitridation reaction of Ti added to the raw powders, and reported the enhancement of bending strength of monolithic Si_3N_4 (around 400 MPa) to around 600 MP by the addition of 10 wt% Ti. *Lian* et al [7] reported a hot press sintering of Si_3N_4 and TiO_2 nanopowder mixtures in a nitrogen atmosphere. As a result, Si_3N_4/TiN nanocomposites with improved bending strength (1154 MPa) and fracture toughness and high electrical conductivity were achieved. Further, *Tatami* et al [8] reported the improvement of abrasion resistance for Si_3N_4/TiN nanocomposite fabricated from Si_3N_4, sintering aids and TiO_2 mixtures.

On the other hand, since Ti has high reactivity with Si_3N_4 and N_2 during sintering, Si_3N_4/Ti composite or FGM system might contain some weak interfacial reaction phase such as TiN and/or TiN-based compounds, which often hide fundamental Ti properties. In fact, not only materials physical properties but also consideration from the thermodynamic viewpoint concerning the reaction between Si_3N_4, Ti, TiN and TiO_2 have been discussed in these previous studies.

As pointed out here, Si_3N_4/TiN composite is expected to be utilized as a high strength material. For the development of these advanced composites consisted of Si_3N_4 ceramic and Ti metal, it is necessary to know the reaction behavior of Ti metal in silicon nitride in detail. The knowledge concerning the behavior of morphological change of TiN particles transformed from Ti in the sintered body produced by in-situ reaction of Ti with Si_3N_4 and N_2 gas, and the effect of the dispersed particles on the physical properties of the TiN composite can be expected to contribute to microstructures and physical properties control of Si_3N_4/TiN composite materials.

In this study, the effect of the morphology and transformation behavior of Ti particles to TiN grains in the hot press sintered body by changing the heating rate for the Si_3N_4 and Ti powder mixtures, which aimed to vary the total heating time during the sintering. Coarse Ti powder was used in this research to clarify the reaction behaviors and also to increase fracture toughness. The effect of these processing parameters on the phase and microstructure development, physical and mechanical properties of the sintered body was investigated and discussed.

2. Experimental procedure

2.1. Powder preparation and sintering

As a base composition of monolithic Si_3N_4 ceramic sample, α-Si_3N_4 powder (SN-E10, Ube Ind., Tokyo, Japan) was mixed with 2 wt% Al_2O_3 powder (AKP-30, Sumitomo Chem. Co. Ltd., Tokyo, Japan) and 5 wt% Y_2O_3 powder (Ishizu Co., Osaka, Japan) as sintering additives. As a composite sample, 10 wt% of Ti powder (TS-450, Toho Titanium Co. Ltd., Kanagawa, Japan) having a particle size of 45 μm or less was added to the monolithic composition. Each powders were placed in a resin bottle together with Si_3N_4 balls having diameter of 3 mm and ethanol as a mixing solution, and mixed by a wet ball mill for 24 h. The obtained slurry was dried using a vacuum evaporator. Then, the dried powder was aggregated by dry ball mill. After that, the mixed powders were passed through a sieve using a 500 μm sieve.

Then, 20 g of each raw powder mixture was put into graphite die with (44 mm of diameter) and hot press sintered at 1650°C for 0.5 h under 30 MPa of uniaxial pressure in N_2 gas atmosphere. The heating rate were changed in this experiments at 25, 30 and 40 °C·min^{-1}. The sintered samples were cut by diamond disc, grinded by #100 diamond grinding stone and polished by 9 to 0.5 μm of diamond slurry to obtain mirror surface. Hereafter, materials ID is denoted as SN_xx or SNTi_xx, where the SN and SNTi corresponds to the monolithic and 10wt% Ti added Si_3N_4 samples, and xx corresponds to the heating rate, 20, 30 and 40 °C·min^{-1}, respectively.

2.2. Material evaluations

The crystallographic phase of raw powders and sintered bodies were determined by X-ray diffraction method (XRD, D8 Advance, Bruker AXS GmbH, Karlsruhe, Germany). The β-type Si_3N_4 phase ratio (here as β) in the samples was calculated from XRD peak intensity of each phases of α-Si_3N_4 (ICDD PDF 010716479) and β-Si_3N_4 (ICDD PDF 000331160) using equation 1, where the α and β are the intensity (i.e. α + β = 1.0), $\alpha_{(hlk)}$ and $\beta_{(hlk)}$ are the intensity of each peaks of the α- and β-Si_3N_4, respectively.

$$\frac{\beta}{\alpha+\beta} = \frac{\beta(101)+\beta(210)}{\alpha(210)+\alpha(201)+\beta(101)+\beta(210)} \quad (1)$$

The density of samples were measured by Archimedes' method using samples immersed in toluene for 24 h. The microstructure were observed by using ultra high-resolution field emission scanning electron microscope (FE-SEM, SU-9000, Hitachi High-Technologies Co., Tokyo, Japan), and elemental analysis were carried out by energy dispersive X-ray spectrometer (EDX, X–Max100TLE, HORIBA Ltd., Kyoto, Japan) coupled in FE-SEM.

The Vickers hardness (*Hv*) was measured using a Vickers Hardness Tester (FV-310e, Future-tech Corp., Tokyo, Japan) on the polished surface with an indentation load of 98 N and holding time of 15 s. Further, the fracture toughness (K_{IC}) were evaluated by the indentation fracture (IF) method [9] using the Eq. (2) with the same condition as that of *Hv* measurement.

$$K_{IC} = 0.203\left(\frac{c}{a}\right)^{-\frac{3}{2}} a^{\frac{1}{2}} Hv \quad (2)$$

where, *c* and *a* are the length of median crack and half of diagonal of indentation.

The Young's modulus (*E*) were determined by the ultrasonic pulse echo method using a digital storage oscilloscope (DSOX3052T, Keysight, Tokyo, Japan) and an ultrasonic

pulser/receiver (Model 5072, PANAMETRICS, MA, USA). The Young's modulus value was calculated by Eq. (3) [10].

$$E = V_S^2 \rho \frac{3V_L^2 - 4V_S^2}{V_L^2 - V_S^2} \quad (3)$$

where, ρ is bulk density of sample, and V_L and V_S are sound velocity of measured longitudinal and transverse waves.

3. Results

3.1 Phase development and sinterability

Under the present experimental condition, well-sintered samples were obtained by hot press sintering at 1650°C for 0.5 h at a heating rate from 25 to 40 °C·min^{-1} in a N_2 gas flow. On the other hand, sufficiently densified sintered bodies were not obtained when the hot press was carried out under an Ar or vacuum conditions. Therefore, the samples sintered under the N_2 atmosphere have been further investigated hereafter.

Fig. 1 shows the XRD patterns of sintered bodies and raw powders. In a raw mixed powder, α-type of Si_3N_4 (ICDD PDF: 010716479) was only identified with sintering additives and metallic α-type of Ti (ICDD PDF: 010773482). On the other hand, the both α- and β-type of Si_3N_4 (ICDD PDF: 000331160) peaks were identified from the whole samples after sintering. In addition, TiN (ICDD PDF: 030650565) was identified from the composite samples (SNTi) instead of metallic Ti. It is generally known for the silicon nitride ceramic that the α-Si_3N_4 of raw powder transformed to β-Si_3N_4 during singeing by following dissolution and re-precipitation mechanism [11]. In the case of Ti added sintered body, the α-Ti peak was disappeared and nitrided metal phase as TiN appeared under the whole sintering, i.e. under the heating rate condition. Also, the titanium silicide phase that was often reported [5] was not identified in the present investigation.

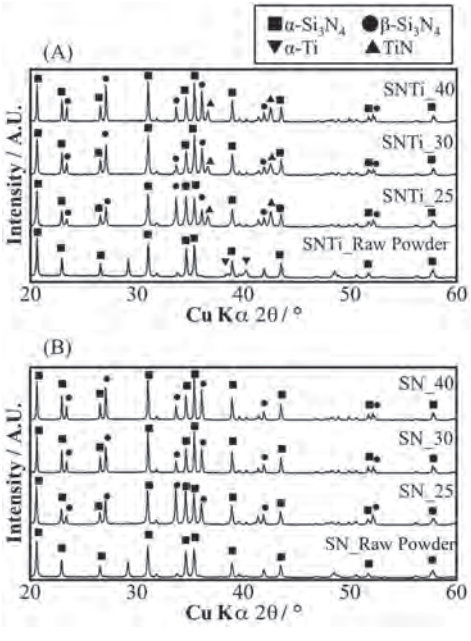

Fig. 1 XRD patterns of sintered bodies and raw powders for (a) monolithic (SN) and (b) Ti-added Si_3N_4 (SNTi) ceramics

1. ábra Szinterelt és nyers porok röntgendiffraktogramjai (a) monolitikus (SN) és (b) Ti adalékolt Si_3N_4 (SNTi) kerámiák

As mentioned above, in this study, an α/β mixed phase was obtained by the hot press sintering. Therefore, the β-ratio, which is the fraction of β-phase in the sintered Si_3N_4, was calculated from the XRD results using the Eq. (1). And the relationships between the β-ration and the heating rate of sintering was shown in *Fig. 2* together with that between the relative density and the heating rate. In the case of monolithic Si_3N_4, the β-ratio was 30-50% depend on the heating rate while the density was 3.236, 3.230 and 3.201 g·cm^{-3} at a heating rate of 25, 30 and 40 °C·min^{-1}, respectively. On the other hand, the β-ratio for the Ti-added samples was around 26 to 38 %, which values were slightly lower than that of monolithic Si_3N_4.

In contrast, the density values (3.321, 3.281 and 3.331 g·cm^{-3} at 25, 30 and 40 °C·min^{-1}, respectively) was slightly higher than the monolithic samples. In spite of the complex reaction of Ti phases among the sintered bodies, the theoretical density of Ti added sample was calculated by assuming 12.6 wt% of TiN dispersion in Si_3N_4 ceramic, which value was calculated by the nitridation of 10 wt% of Ti into TiN, resulted in the value of 3.362 g·cm^{-3} as the theoretical density of the samples. The relative densities were then obtained and reached to 95 TD% or more under all the sintering conditions (*Fig. 2.b*), indicating that a sufficiently densified sample was obtained. In the case of monolithic Si_3N_4, the relative density tended to decrease with increase in heating rate as shown in *Fig. 2.b*, however, both β-ratio and relative density of Ti dispersed sample showed lower values for the sample obtained from 30 °C·min^{-1}.

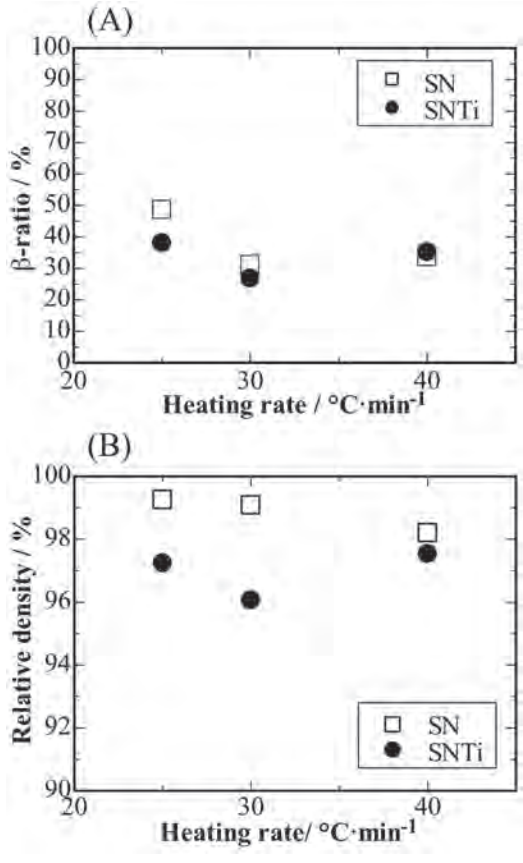

Fig. 2 Effects of heating rate on (a) β-ratio and (b) relative density for sintered samples

2. ábra Felfűtési sebesség hatása (a) a β-arányra és (b) a realtív sűrűségre a szinterelt mintákban

3.2 Microstructure

Fig. 3 shows a SEM image of Ti particle in the raw mixture powder. The average diameter of Ti particles in the raw mixture powder were 5.83 μm which was smaller than the raw Ti particles (<45 μm) by ball milling. It was also observed that raw Si_3N_4 and additives powders, which primary size was much smaller than that of Ti, were adhered around large Ti particle.

Fig. 4 shows the optical image on the polished surface of the sintered body. The surface of monolithic Si_3N_4 was smooth, and a few pores were observed (*Fig. 4.a*). On the other hand, large particles of several tens of micrometers were found to disperse in the matrix of the Ti-added composite sample (*Fig. 4.b)*. The color of these large particles were gold, which was the typical color of the TiN compound, and is consisted with the result of XRD analysis.

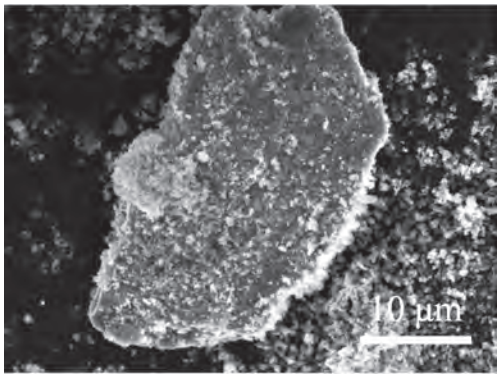

Fig. 3 SEM image of titanium particle in the raw mixture powder. Fine particles are Si_3N_4 raw material
3. ábra Titán részecskék elektronmikroszkópos képe a nyers por keverékben. A finom részecskék a nyers Si_3N_4 anyag

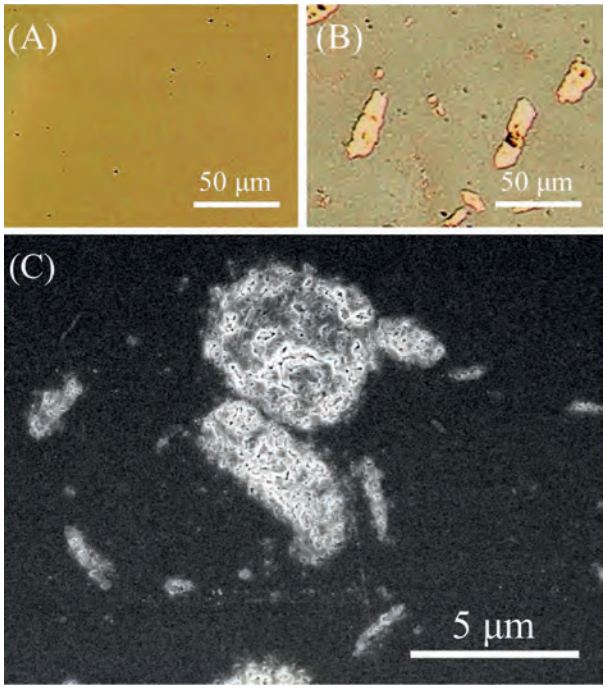

Fig. 4 Optical images on the polished surface of the sintered bodies for (a) monolithic Si_3N_4 (SN_25) and (b) Ti-added Si_3N_4 (SNTi_25), and SEM image on the surface for (c) Ti-added Si_3N_4 (SNTi_40)
4. ábra Szinterelt minták polírozott felületének optikai képe (a) monolitikus Si_3N_4 (SN_25) és (b) Ti adalékolt Si_3N_4 (SNTi_25), és elektronmikroszkópos felvétel a felületen (c) Ti adalékolt Si_3N_4 (SNTi_40) anyagra vonatkozóan

To evaluate structures of dispersed phase in more detail, SEM observation and EDS analysis for the formed TiN particles were carried out, and the results are shown in *Fig. 5*. The Ti particle used as raw powder had a dense structure, however, porous structure and inner grain boundaries were observed in Ti-derived particles. Ti and N was detected from the corresponding Ti-derived particles by EDS. Nitrogen was found also in the center of the particle, indicating that N penetrated to the central part of Ti particles. From the matrix region, Si, Al and Y as well as N derived from Si_3N_4 and additives were detected. Based on the above results as well as the XRD (*Fig. 1*), it was clear that the metal Ti particles used as a raw material was nitrided during sintering to form TiN, thus obtained material by this sintering method was Si_3N_4/TiN composite.

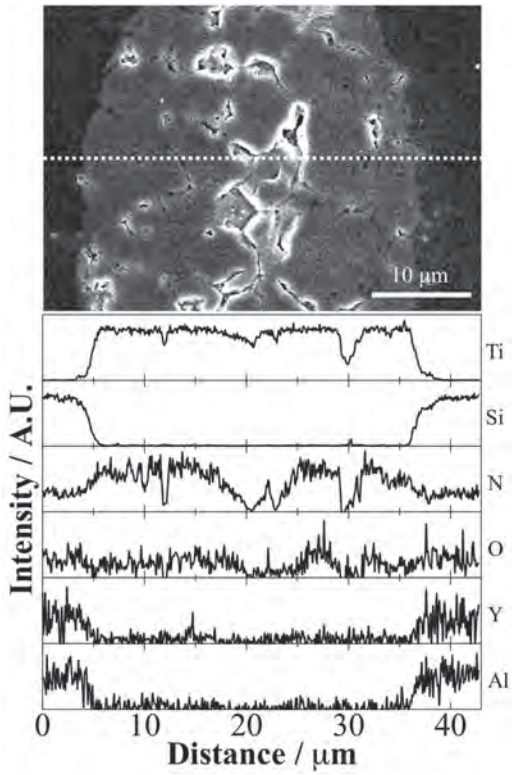

Fig. 5 SEM image of titanium-derived coarse TiN particle and EDS line analysis results (scan on broken-line) for the cross-sectional surface of the SNTi_25 sample, where the EDS line scan was taken for the parallel to the uniaxial pressing direction
5. ábra Elektronmikroszkópos felvétel Ti generált TiN szemcséről és EDS vonal elemzés (felvétel törött felületen) a SNTi_25 minta keresztmetszeti felületén, ahol az EDS vonal elemzés iránya párhuzamos az egytengelyű nyomás irányával

Fig. 6 shows the relationships between heating rate and equivalent diameter of dispersed TiN particle in the sintered bodies, where the diameter was calculated by the image analysis method from obtained SEM images. The diameter value of the dispersed phase was 12.29, 10.25 and 9.98 μm at the heating rate of 25, 30 and 40 $^{o}C \cdot min^{-1}$, respectively, and tended to decrease as the heating rate increased. The diameter of the dispersed particle was approximately two times larger than that of used Ti raw powder, which was 5.8 μm, showing the particle size increase was governed after the hot press sintering.

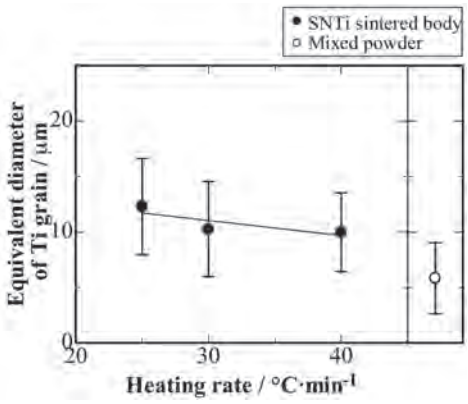

Fig. 6 The relationship between heating rate and equivalent diameter of TiN particles formed in the Si_3N_4 sintered samples
6. ábra A felfűtési sebesség és a kialakuló TiN szemcsék egyenértékű átmérőjének összefüggése szinterelt Si_3N_4 mintákban

4. Discussion

Generally, sintered Si_3N_4 is well known to be formed by a dissolution of α phase in liquid phase by sintering additives and followed re-precipitation and growth as to be β phase grains [11]. In the present study, the mixed phase of α- and β-Si_3N_4 was observed a mentioned before (*Fig. 1*). In this study, we selected a sintering condition with a relatively higher heating rate (> 25 °C·min^{-1}), lower sintering temperature (1650°C) and shorter holding time (~ 0.5 h) compared to the commonly used condition of Si_3N_4 sintering, above 1800°C [11]. For this reason, unlike the commonly obtained sintered body with single β-phase, the present samples contained the both β- and α-phases. Nevertheless, sintered samples were fairly densified, more than 95% of relative density (see *Fig. 2*). This phenomenon was often reported for the Si_3N_4 sintered by pulse electric current sintering (PECS, also described as SPS) which enables rapid and short-time sintering [5, 12].

4.1 Effect of Ti addition to Si_3N_4 on physical properties

Fig. 7 shows the relationship between the heating rate and the Young's modulus. In the Si_3N_4 monolith, the Young's modulus tended to decrease slightly with increase in heating rate. On the other hand, Young's modulus of Ti-added samples slightly increased with the heating rate. The theoretical Young's modulus of the Si_3N_4 composite containing 12.6 wt% of TiN (by considering complete transformation of Ti to TiN as mentioned before) was estimated by the Hill's equation [13], and the value was calculated to be 325 GPa. However, the observed Young's modulus of the present samples was lower than the calculated value, which was around 270 GPa (30 °C·min^{-1}) to 305 GPa (40 °C·min^{-1}).

As found by the SEM investigation, the present composites contained aggregated but porous polycrystalline TiN regions (see *Fig. 5*) which dispersed in dense Si_3N_4 matrix. It imply us that the porosity of the TiN particles might affect on the decrease in density of the sintered samples, and then resultantly on the decreased Young's modulus. Thus, at first, the density of TiN particle (d_{TiN}) dispersed in sintering body was calculated from the relationship between density and mass concentration by the Eq. (4).

$$d_{TiN} = \frac{W_{TiN} d_c d_m}{(1-W_{TiN})(d_m - d_c) + W_{TiN} d_m} \quad (4)$$

Where d_m and d_c is the measured density of monolithic Si_3N_4 and TiN dispersed Si_3N_4 composite, respectively, and W_{TiN} is the mass concentration of TiN in the sintered body (12.6 wt%). Further, the porosity in the TiN particle region (P_{TiN}) was taken into account and was calculated from the relationship between the density and the porosity by Eq. (5),

$$P_{TiN} = 1 - \frac{d_{TiN}}{d_{th,TiN}} \quad (5)$$

where, $d_{th,TiN}$ is the theoretical density of TiN (5.45 g·cm^{-3}).

Then, the Young's modulus of porous TiN grain (E) was calculated using the Eq. (6) [14] representing the porosity dependency of the elastic modulus of the porous body.

$$E = E_0(1 - P_{TiN}) \quad (6)$$

Were E_0 is the Young's modulus of fully-densified TiN (390 GPa). *Table 1* shows the calculated porosities of the TiN particle and Young's modulus. The porosity of TiN particle was estimated to 13, 32 and 24% at 25, 30 and 40 °C·min^{-1}, respectively. These values seems to be reasonable by considering porous morphology of TiN grains observed by SEM image in *Fig. 5*. On the other hand, the Young's modulus of the porous TiN particles was estimated to be about 294, 265 and 339 GPa at 25, 30 and 40 °C·min^{-1}, respectively. High porosity and low Young's modulus were observed for the sample sintered at 30 °C·min^{-1}, which was due to the low density for the sample.

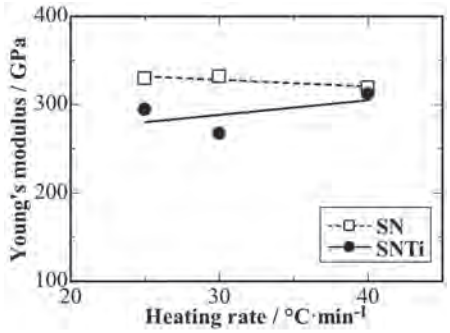

Fig. 7 Effect of heating rate on the Young's modulus for sintered Si_3N_4 samples
7. ábra A felfűtési sebesség és a rugalmassági modulus összefüggése szinterelt Si_3N_4 mintákban

Heating rate / °C·min-1	*PTiN* / %	*E* / GPa
25	24	294
30	32	265
40	13	339

Table 1 Calculated porosity and Young's modulus of TiN particle within the sintered Si_3N_4 samples. The values were estimated from each density data
1. táblázat Számított porozitás és rugalmassági modulus a TiN szemcsében a szinterelt Si_3N_4 mintákban. Az értékek becsült mennyiségek az egyes sűrűség adatok alapján

4.2 Effects of large and porous TiN grain on the mechanical properties.

Fig. 8.a shows the relationship between heating rate and the Vickers hardness. The hardness of the Si_3N_4 monolithic

was about 18 GPa, and the effect of the heating rate was not confirmed. The hardness of TiN dispersed samples was around 15 GPa, which was slightly lower than Si_3N_4 monolith. However, as discussed above, the *Hv* of composites was reasonable by considering the fact that large but porous TiN particles were dispersed in.

Fig. 8.b shows the relationship between heating rate and fracture toughness measured by the indentation fracture method. The fracture toughness of the monolithic Si_3N_4 showed a tendency to slightly decrease with increase in heating rate. On the other hand, the TiN dispersed samples showed an opposite tendency, and the value increased to 5.8 MPa·m$^{1/2}$ at 40 °C·min^{-1} which was higher than the toughness value of the monolithic Si_3N_4 sintered at the same condition.

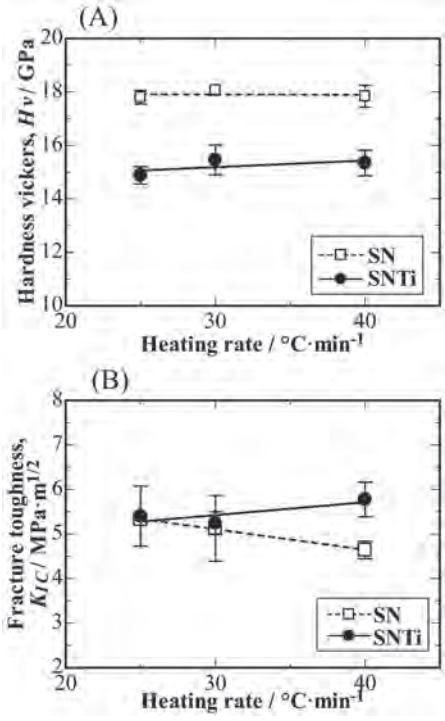

Fig. 8 Effect of heating rate on mechanical properties for sintered samples, (a) Hardness and (b) Fracture toughness
8. ábra A felfűtési sebesség hatása szinterelt minták mechanikai jellemzőire, (a) keménység és (b) törési szívósság

To discuss the mechanical properties of the present Si_3N_4/TiN composites from viewpoint of the crystalline phase of Si_3N_4 matrix, i.e. the effect of α/β phase, the relationships between these mechanical properties and β-ratio of Si_3N_4 matrix were shown in *Figure 9*. It is reported that the α-Si_3N_4 single crystal has 1.3 times higher hardness value that that of β-Si_3N_4 [15]. It is thus easily predicted that hardness declined as the β-ratio increases. In fact, *Kawaoka* et al [12] reported that the hardness and the Young's modulus decreased while the fracture toughness increased when the β-ratio increased for the spark plasma sintered Si_3N_4.

In the present study, however, the hardness of both monolithic and TiN dispersed Si_3N_4 did not depend strongly on the β-ratio (*Fig. 9.a*) although the value was higher for the monolithic Si_3N_4, which was, as discussed before, due to the dispersion of porous TiN phase. The reason of this behavior is regarded as the trade-off relation between the decreased hardness due to the density degradation and the increase in hardness due the increased α-Si_3N_4 ratio in the samples.

It is well-known that fracture toughness of sintered Si_3N_4 generally increases with grain growth of β-Si_3N_4 particles, especially formation of elongated large β-grains, resulting in high fracture toughness for high β conversion ratio [12]. In the present case, the toughness value seemed to be higher for the higher β-ratio. However, the correlation between the β-ratio and the fracture toughness was not distinct (*Fig. 9.b*).

For the TiN dispersed samples, it was considered that the fracture toughness value seemed to be affected more by the characteristics of the dispersed TiN; Sample SNTi_40 (40 °C·min^{-1}) showed the highest toughness and the lowest porosity in dispersed TiN (P_{TiN} = 13%, see *Table 1*), while the SNTi_30 (30 °C·min^{-1}) containing porous TiN (P_{TiN} = 32%) exhibited the lowest toughness among the composites. These fact imply us that the microstructural characteristic of dispersed TiN grains, i.e. porous structure, is more dominantly affect on the fracture toughness than the β-ratio of matrix.

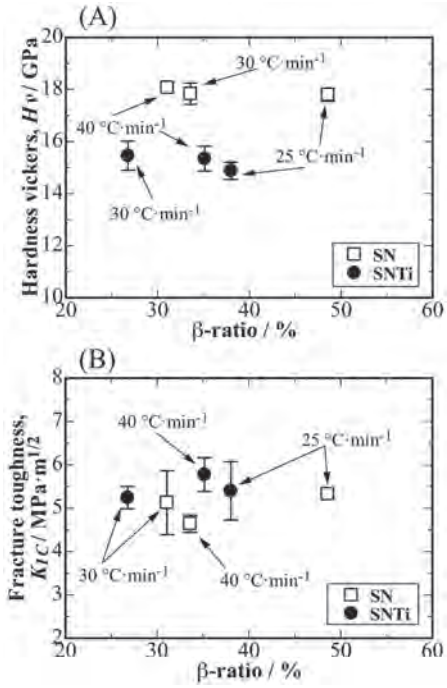

Fig. 9 The relationship between β-ratio and (a) Hardness, (b) Fracture toughness and (c) Young's modulus of sintered samples
9. ábra Összefüggések a β–aránnyal (a) keménység, (b) törési szívósság és (c) rugalmassági modulus a szinterelt mintákban

4.3 Microstructural characteristics of dispersed TiN particles

Although the Ti particle of the raw powder was large (*Fig. 3*), Ti-derived grains in the sintered body were polycrystalline but porous structure as explained before (*Fig. 4.c*). Thus it is said that the present Si_3N_4-based composite has a unique structure, where porous TiN grains were dispersed in Si_3N_4 matrix. The reason why such a complicated structure is formed will be discussed below. It should be considered that the Ti particles expanded during the reaction (transformation) to TiN. The mass increase rate when Ti (molecular weight: 47.96 g·mol^{-1}

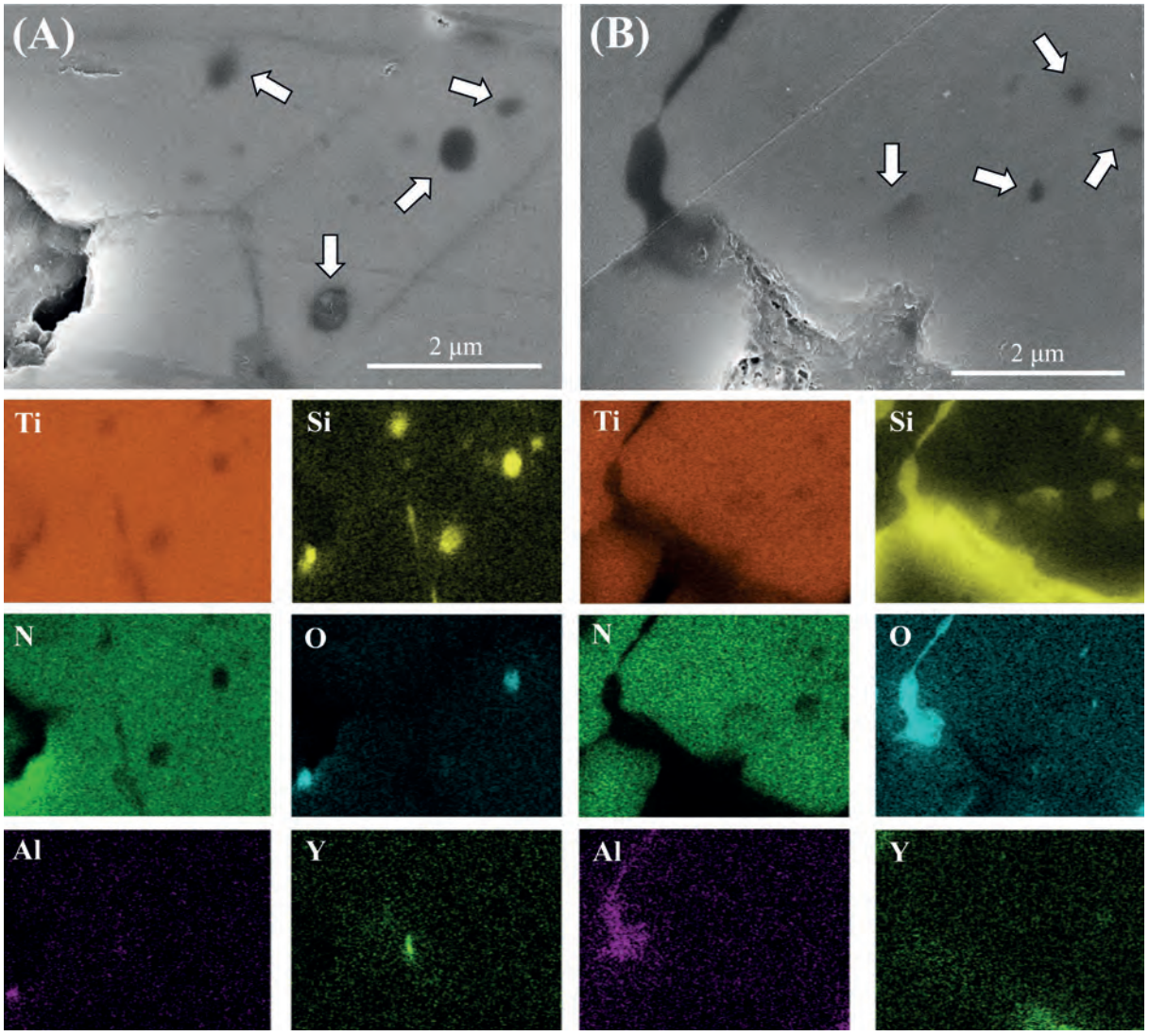

Fig. 10 Magnified SEM image of the center of TiN grain and corresponding elemental mapping images of Ti, Si, N, O, Al and Y for the samples (a) SNTi_25 and (b) SNTi_30
10. ábra Felnagyított elektronmikroszkópos felvétel a TiN szemcse középpontjában és a hozzá tartozó elemanalízis (Ti, Si, N, O, Al és Y) a mintákban (a) SNTi_25 és (b) SNTi_30

density: 4.51 g·cm^{-3}) transforms to TiN (weight: 61.96 g·mol^{-1}, density: 5.45 g·cm^{-3}) is 1.29, while the volume increase rate is calculated to be 1.068, which corresponds to only 2.2 % (1.022 times) increase in equivalent particles diameter. However, in this study, average grain size of dispersed TiN in the sintered Si_3N_4 (SNTi_25; 25 °C·min^{-1}) was 2.1 times larger than that of used raw Ti particles (see *Fig. 6)*. Therefore, it is not able to explain the reason of larger TiN by the chemical reaction (nitridation of Ti), and it is considered to be a minor role.

Magnified SEM and elemental mapping images of inside of TiN grains in the sintered body for SNTi_25 (heating rate of 25 °C·min^{-1}) and SNTi_30 (30 °C·min^{-1}) are shown in *Figs. 10.a* and *10.b*, respectively. It was clearly seen that the Ti-derived grain was polycrystalline structure with grain boundaries. In addition, some finer particulates which size is around 1 µm or less can be seen within the grains (see arrows in SEM images of *Fig. 10*). From element mapping results, Ti and N was uniformly detected from the whole area except pores, grainboundary and finer particles mentioned above, which results well agree to the fact previously discussed that the Ti was converted to the TiN during sintering. On the other hand, Si was found in the finer particles inside of the TiN and at some part of grain boundaries of TiN. Oxygen was also detected from not all but some region of Si detected (particulates and grainboundary). In addition, Al was often detected from the grain boundary phase together with Si and O (see *Figs. 10.a* and *10.*b). These results implied that the particulates inside of TiN was SiO_2 and Si, which might be formed or precipitated by the complicated reaction during sintering. At the grainboundary of formed TiN, SiO_2 or Al-Si-O compound were also precipitated during the reaction.

From these facts, it was considered that Si, Al, Y and O elements in Si_3N_4 and additives (Al_2O_3 and Y_2O_3) might diffused into the Ti particles during the nitridation reaction or into the formed TiN phase at the late stage of sintering. In the TiN regions, some oxides consisted of SiO_2 or Al-Si-O were found as mentioned above. These silica-based oxides were known to have lower melting temperature and to form glassy phase, and thus liquid phase of these oxides might exist during sintering that promoted reaction of TiN with Al and/or O and formation of Al-Si-O phases at the boundaries among TiN regions. Based on these results, the formation of coarse and porous TiN grains within Si_3N_4 matrix as well as enlargements of TiN grain size

more than primary Ti particles might be considered due to the combination of several factors as described follows.

Reaction and followed solid solution formation of constituent elements, especially Si-O and/or Si-Al-O based compounds near the Ti particles, should be taken place at first. In fact, grain boundary phases containing Si and O as major elements and Al, Y and Ti as minor elements. These grain boundary phases seemed to be generated form a liquid phase, and they were penetrated and precipitated into the internal grain boundary of polycrystalline TiN particles produced from Ti, thereby dividing primary Ti particles and increasing the equivalent diameter of Ti-based particles. The fine particulates within TiN, which were consisted mainly from Si-O or Si (*Fig. 10*), were considered to be formed by precipitation during sintering followed by the diffusion of corresponding elements in the raw materials into Ti particles.

Before or at the same time, nitridation of metallic Ti might be taken place by the direct reaction of Ti with N_2 atmosphere, or by the reaction with Si_3N_4 particles, because the reactivity of Ti with nitrogen is thermodynamically high. Reaction of nitrides with liquid phase might promote further diffusion of elements, such as Y etc. into the TiN, which could be seen in small amount but uniform distribution of Si, O and Y within the TiN particles existing as solid solution or precipitates as fine particles within TiN (see for example Si, O and Y in *Fig. 10.a*).

In addition, the effect of pressurization, i.e. mechanical uniaxial pressing during sintering should be considered. In this study, sintering was performed by hot press method at a high temperature of 1650°C, which corresponded to 0.99 T_m of Ti metal, extremely close to the melting point of Ti (T_m = 1668°C). At this temperature, Ti was sufficiently softened, and hence it might easily react with other components including Si_3N_4, nitrogen and formed oxide glassy phases.

In the case of nano-sized TiN dispersed dense Si_3N_4 composites, it was reported that the addition of several tens of volume percents of TiN was necessary to achieve the enhanced toughness [6, 7]. In this study however, Si_3N_4 composites containing porous TiN grains, in which the porosity of around 20 vol%, exhibited decreased hardness while slightly increased fracture toughness compared to the monolithic Si_3N_4 sintered ceramic by addition of only 10 wt% of Ti powder to Si_3N_4 matrix.

It is suggested that the formation of grain boundary phases within the porous TiN regions might improve bonding between constituent TiN particles with the porous regions, i.e. strengthening porous TiN structures, and also contribute to make better bonding between porous TiN and Si_3N_4 matrix, implying us that the dispersing coarse Ti particles and promotion of reaction to form porous TiN grains would be advantageous to develop Si_3N_4-based composites with improved mechanical properties by using commercially-available coarse metal powders.

5. Conclusions

Coarse-grained Ti metal powder was added by 10 wt% to Si_3N_4 raw powder together with Al_2O_3 and Y_2O_3 sintering additives, and the mixtures were hot-press sintered in a nitrogen atmosphere under an uniaxial-pressure of 30 MPa at 1650°C for 0.5 h with different heating rate. Effect of heating rate for hot-press sintering was investigated for the obtained Si_3N_4-based composites. The TiN grains were finally dispersed in the Si_3N_4 sintered bodies due to the reaction of Ti with Si_3N_4 and/or N_2 atmosphere during sintering. The following conclusions were obtained through the structural and mechanical properties investigations.

Coarse Ti powders reacted to form TiN grains during sintering. It was found that the formed TiN grains consisted from polycrystalline and porous TiN having oxides grain boundary phases of Si, O, Al and some minor elements. These implied that the obtained Si_3N_4 sintered body was complicated composite structure consisted of porous TiN grains (porosity of 13 to 32%) dispersed in dense Si_3N_4 matrix.

The Si_3N_4 matrix had the mixed phase of α- and β-type Si_3N_4, where the β-phase of around 26 to 38%, due to the relatively lower sintering temperature and higher heating rate for sintering. However, matrix itself was mostly densified of over 95% under the present sintering conditions.

Polycrystalline and porous TiN grains were much larger (~2 times) than the used coarse Ti particles and as well as than the theoretically-estimated particle size of nitrided Ti. It was considered that the reaction between Ti and other compounds such as Si_3N_4, Al_2O_3 etc. and resultant formation of glassy phase within the TiN regions might contribute to the enlargement of particle size from Ti to porous TiN during sintering.

Comparing with Si_3N_4 monolithic samples, Ti-added samples exhibited lower hardness and Young's modulus due to the porous structure of dispersed TiN grains. However, fracture toughens slightly enhanced than that for monolithic Si_3N_4. The present composite contained the both α and β-Si_3N_4 that suspected the lower toughness due to the lesser amount of elongated β-grains of matrix, however, the increased toughness was considered due to the dispersion of porous but large TiN grains in the matrix.

6. Acknowledgements

This work was supported by the program Dynamic Alliance for Open Innovation Bridging Human, Environment and Materials in Network Joint Research Center for Materials and Devices (MEXT, Japan).

References

[1] Carim, A. H. (1990): Transitional Phases at Ceramic–Metal Interfaces: Orthorhombic, Cubic, and Hexagonal Ti-Si-Cu-N Compounds. *Journal of the American Ceramic Society*, Vol. 73, pp. 2764-2766. https://doi.org/10.1111/j.1151-2916.1990.tb06762.x

[2] Shinohara, Y. – Imai, Y. – Ikeno, S. – Shiota, I. – Fukushima, T. (1992): Thermal stability of NiCrAlY/PSZ by plasma twin torches method, *ISIJ International*, Vol. 32, pp. 893-901. https://doi.org/10.2355/isijinternational.32.893

[3] Tsuda, K. – Ikegaya, A. – Nomura, T. (2000): Development of functionally graded sintered hard material, *Journal of Powder Metallurgy*, Vol. 47, pp. 487-495. https://doi.org/10.1179/pom.1996.39.4.296

[4] Wriedt, H.A. – Murray, J. L. (1987): The N-Ti (Nitrogen-Titanium) System, *Bulletin of Alloy Phase Diagrams*, Vol. 8, pp. 378-388. https://doi.org/10.1007/BF02869274

[5] Ahmad, N. – Sueyoshi, H. (2010): Properties of Si_3N_4-TiN composites fabricated by spark plasma sintering y using a mixture of Si_3N_4 and Ti powders, *Ceramics International*, Vol. 36, pp. 491-496. https://doi.org/10.1016/j.ceramint.2009.09.029

[6] Qiliang, H. – Juan, C. – Wei, P. – Jian, C. – Jie, L. (1997): In situ processing of TiN/Si_3N_4 composite by Ti-Si_3N_4 solid state reaction, *Material Letters*, Vol. 31, pp. 221-225. https://doi.org/10.1016/S0167-577X(96)00277-7

[7] Gao, L. – Li, J. – Kusunose, T. – Niihara, K. (2004): Preparation and properties of TiN-Si_3N_4 composites, *Journal of the European Ceramic Society*, Vol. 24, pp. 381-386. https://doi.org/10.1016/S0955-2219(03)00218-8

[8] Tatami, J. – Watanabe, H. – Wakihara, T. – Yoneya, K. – Meguro, T. (2008): Development of Nano-particle Dispersed Si_3N_4 Ceramics Using Composite Powders Prepared by Mechanical Treatment, *Funsai* (in Japanese), Vol. 51, pp. 52-56.

[9] Nihara, K. (1983): A fracture mechanics analysis of indentation-induced Palmqvist crack in ceramics, *Journal of Materials Science Letters*, Vol. 2, No. 5, pp. 221-223. https://doi.org/10.1007/BF00725625

[10] Nishida, T. – Yasuda, E. (Ed.) (1986): Evaluation of mechanical properties of ceramics, *Nikkan Kogyo Shinbun Sya*, Tokyo Japan.

[11] Mitomo, M. – Mizuno, K. (1986): Sintering Behavior of Si_3N_4 with Y_2O_3 and Al_2O_3 Addition, *Yogyo Kyokaishi* (in Japanese), Vol. 94, No. 1085, pp. 106–111. https://doi.org/10.2109/jcersj1950.94.106

[12] Kawaoka, H. – Adachi, T. – Sekino, T. – Choa, Y. – Gao, L. – Niihara, K. (2001): Effect of α/β phase ratio on microstructure and mechanical properties of silicon nitride ceramics, *Journal of Materials Research*, Vol. 16, No. 8, pp. 2264-2270. https://doi.org/10.1557/JMR.2001.0311

[13] Miki, M. – Fukuda, T. – Motoki, S. – Hohjo, M. (1997): Composite Material, *Kyoritsu Shuppan*, Tokyo Japan, pp.70-72.

[14] Kondo, R. (1978): Porous material –Properties and Application, *Gihodo Shuppan*, Tokyo Japan, pp.174-181.

[15] Niihara, K. – Hirai, T. (1978): Hardness anisotropy of α-Si_3N_4 single crystal, *Journal of Materials Science*, Vol. 13, pp. 2276-2278. https://doi.org/10.1007/BF00541688

Ref.:
Baba, Sotaro – **Goto,** Tomoyo – **Cho,** Sunghun – **Sekino,** Tohru: *Microstructure and mechanical properties of TiN dispersed Si_3N_4 ceramics via in-situ nitridation of coarse metallic Ti*
Építőanyag – Journal of Silicate Based and Composite Materials, Vol. 70, No. 6 (2018), 195–203. p.
https://doi.org/10.14382/epitoanyag-jsbcm.2018.34

Finite Element Method analysis for mechanistic design in flexible pavement, Review: From how to build a material in FE analysis to complexity in reality

Seoyoung CHO ▪ Department of Highway and Railway Engineering, Budapest University of Technology and Economics ▪ hotaru128@hanmail.net
Csaba TÓTH ▪ Department of Highway and Railway Engineering, Budapest University of Technology and Economics
Zoltán SOÓS ▪ Department of Highway and Railway Engineering, Budapest University of Technology and Economics

Érkezett: 2018. 07. 16. ▪ Received: 16. 07. 2018. ▪ https://doi.org/10.14382/epitoanyag-jsbcm.2018.35

Abstract
There are plenty of applications of finite element methods (FEM) in various fields. FEM itself stands strong in the field of structural analysis and the trend of applying it into asphalt pavement is widespread. As the mechanistic analysis becomes an important part of pavement design for the estimation of its structural response, FEM in terms of precise mechanical design became one of a strategic tool. Hereinafter a short overview of FEM adapted flexible pavement design field will be introduced. The main focus will be on how the material model for each layer of pavement structure is embodied in FE modeling. The aim of this overview is to show a stream of FEM application in flexible pavement design and call an attention to its potential. A strong point and shortcoming will be introduced as well, and try to reflect recent trends.
Keywords: finite element method, asphalt pavement analysis, material model

Seoyoung CHO, PhD Student
PhD student at Budapest University of Technology and Economics.

Csaba TÓTH PhD, MBA
Member of the Hungarian Chamber of Engineers, the Hungarian Scientific Association for Transport and the Hungarian Road Society. Worked as Head of Division at Csongrád Couty Road Administration, then ÁKMI Kht. Involved in quality control of Hungarian road developments and both national and international researches as part of the Strabag concern. Had a role in several road overlay projects as engineering expert, designer and supervisor. Currently Assistant Professor and Head of Asphalt Unit at the Pavement Laboratory. Research field includes load bearing capacity of road structures and overlay design of flexible pavements.

Zoltán SOÓS, PhD
Obtained PhD in pavement design at Department of Highway and Railway Engineering, BME. Member of the Hungarian Scientific Association for Transport. Research topics include testing and design of asphalt pavement materials and road structures with emphasis on fatigue behaviour and service life, performance and structural design. Takes part in lecturing at the University and as Deputy Head, in the work of the Pavement Laboratory since 2015.

1. Introduction

For decades, the multilayered elasticity model is widely used in pavement structure analysis. Software based on multilayered elastic model such as ILLIPAVE, MICHPAVE and EverStress are easy to use, however, granular material of pavement structure shows nonlinear behavior that is there is a need of mechanistic analyses which can deal with this characteristic. FE method can be powerful tool for this thanks to its user define element command. Not only the measurement of critical response can be done easily by FE program, but also it helps analysts to build a stress-dependent material model by editing some part of codes so FEM can be distinguished from existing multilayer elastic analysis programs.

As the design concept of Mechanistic-Empirical design on pavement design was introduced, there are the various tool for supporting mechanistic design also become widespread. Representatively, Finite Element (FE) Method is one of the tool for mechanistic design. Since the commercial FE analysis solution contains constitutive equations in itself, the FE method could be used in pavement design to model the viscoelasticity or anisotropy. However, commercial FE solutions do not fully support nonlinear analysis of pavement design like stress dependent strength in each layers, and not suitable for the purpose of investigating material properties. Thus in recent days researchers are trying to involve this nonlinearity into analysis in their own codes.

Here the followings are about those codes in time series. Tried to introduce essential process during development of numerical model and the background of FE analysis in pavement design.

2. Constitutive equations of pavement layers

Pavement is composite with layers, which are having different material property from each other but work together to move as a one structure so it makes analysis be difficult. The essence of analysis is to verify each layer's response to depict the behavior of whole pavement structure. FE is the tool for this verification. Followings are well known constitutive equations for each layer.

2.1 Asphalt concrete surface layer

The dynamic modulus measured over various temperature ranges and load cycles can be converted into master curves that represent the physical properties of the asphalt concrete for pavement thickness design and for the performance analysis.

Most of case asphalt binder and mixture is affected by temperature and loading frequency. These material properties cause those bituminous layer displays viscoelasticity. As a strength parameter of these bituminous material's property, dynamic modulus (E^*) is used:

$$E^*(t) = \frac{\sigma_0}{\varepsilon_0} e^{-i\varphi} = |E^*| e^{i\varphi} \quad (1)$$

This complex modulus is a function of stress and strain amplitudes (σ_0; ε_0), phase angle (φ), angular frequency (ω) and imaginary number.

Bituminous materials like asphalt mixture displays time dependent mechanical behavior. A Huet-Sayegh model describes response of bituminous material. This mathematical representation can simulates the behavior of asphalt mixes

in cycling tests in wide frequency range [1]. This model is implemented as a rheological model which employs additional dashpot in series along with spring elements (*Fig. 5*). Mathematical expression of Huet-Sayegh model is below, Eq. (2).

$$G^*(\omega) = G_0 + \frac{G_\infty - G_0}{1 + \delta_1(i\omega\tau_1)^{-m_1} + \delta_2(i\omega\tau_2)^{-m_2}} \quad (2)$$

Eq. (2) indicates a shear modulus in Huet-Sayegh model in frequency domain. G_0 is rubbery shear modulus, G_∞ is instantaneous shear modulus. τ_1 and τ_2 are parabolic dashpot's time constant, m_1, m_2, δ_1, and δ_2 are model parameters.

2.2 Subgrade

Subgrade modulus shows a stress-dependency on its modulus, thus the modeling of it includes the modulus values assigned to any element are related to previously computed values of stress for that element [2], [4].

It is known that subgrade modulus (M_r) is the key factor which controls the surface deflection in flexible pavement since base course layer modulus and asphalt surface modulus have minor effect on surface deflection compare to effect of subgrade modulus [22]. Among the intense studies on constitutive models of subgrade, followings are the roots of widely used ones until now (*Table 1*). Main features of those models is that it contain stress state; principal stress (σ_3), bulk stress (θ), deviatoric stress (σ_d) inside the modulus (M_r).

Model name	Subgrade modulus
Confining model [4]	$M_r = k_1 (\sigma_3)^{k_2}$
K-θ model [5]	$M_r = k_1 (\theta)^n$
Uzan model [6]	$M_r = k_1 (\theta)^{k_2} (\sigma_d)^{k_3}$

Table 1. Subgrade modulus models
1. táblázat Modellek az alapréteg modulusának meghatározására

The models shown in *Table 1*, M_r is related to stress state in complicate relation. FE method is practical to predict stress states with accuracy and includes those stress state got from the formal analysis step to following analysis step instantly.

3. FE model

The pavement is a layered structure and the load applied is delivered on the AC surface to the underlying layers. Thus the modeling of the pavement structure is to set element data for each layer and consider all layers acting as whole one structure. *Fig. 1* describes the cross section of numerical model, and positioned the critical point where the plastic distress occurs. Geometry and load configuration look simple to model, but there is a complexity on modeling realistic behavior of computation.

From the studies researchers found that granular materials of pavement structure exhibits stress-dependency that is resilient behavior. FE programs that analyze pavement structures need to take into account this nonlinearity resilient characterization to make much realistic analysis.

The difference in behavior between a homogeneous (elastic half system) and a layered system modeled by FE method is shown in *Fig. 3*, where the contributions to surface deflection are functions of depth beneath the surface. It shows that the contribution of the material in deep part plays an important role on the deflection in multi-layer system than the half-space [6], [12]. This analysis shows the awareness of effect on surface deflection of sub-layer is important, and has to guarantee enough depth but does not exceed length-to-width ratio five to one.

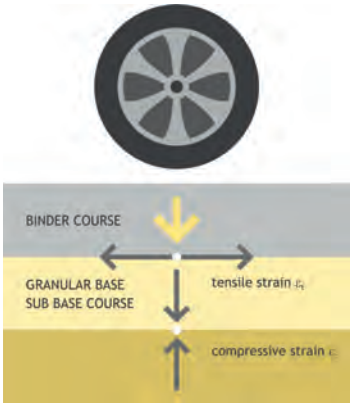

Fig. 1 Typical cross section of pavement with critical locations [19]
1. ábra A pályaszerkezet kritikus feszültségeinek típusa és helyzete [19]

In terms of convenient and accurate analysis, the former ones are suitable with relatively simple inputs. The latter ones are for realistic analysis but requires analysts a period to be skilled. The result may differ from the analysts because the assumptions on inputs during modeling process are up to analysts. There guidelines exist to avoid individual error and set a ready-to-use input guide [1]. Followings are the introduction of studies to set a subjective input variables.

3.1 Material modeling

Material selection in FE modeling is the crucial process. To build more realistic numerical model, the proper material selection has to be followed. There are the isotropic and anisotropic material models which can be modeled by differ the horizontal and vertical elastic modulus. Since the soil particle is not a regular shaped, considering the anisotropic properties of materials during modeling can be sometimes needed.

Anisotropic properties of materials have no significant effect on the magnitude of pavement displacement under traffic loads, while have significant effect on the magnitude of tensile strain. However, in terms of service life there is no significant difference between isotropic and anisotropic models [18]. *Fig. 2* shows the differences in the tensile strain at the bottom of the asphalt layer between isotropic model and anisotropic model (where, $n = E_h/E_v$).

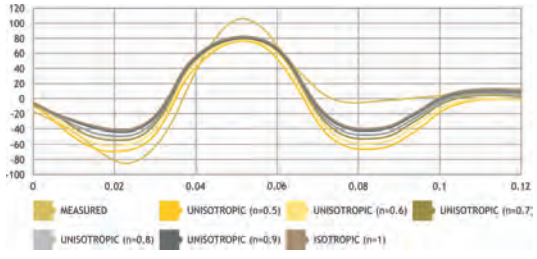

Fig. 2 Comparison between measured and calculated longitudinal strain at the bottom of the wearing surface [18]
2. ábra A mért és számított vízszintes húzófeszültség közötti összehasonlítás a kopóréteg alján [18]

Another material model to decide is to determine whether the model will be linear or nonlinear. A thing to be cleared is that thanks to resilient behavior of pavement, it is enough to set up model system with an elastic constitutive relationship. The fact that well known is that granular materials and subgrade soils performs non-linear resilient behavior which is varied by level of stress.

Most of time the design of pavement stress is based on multilayered elasticity theory, however, disadvantage of this theory comes from its assumption; each layer is homogeneous throughout the layers. In particle level, material behaves in nonlinear way and if the model neglects this nonlinearity then it cannot have much realistic results. FE programs are used to solve this shortcoming by combining the material models; until now K – θ model and bilinear material model is used for granular layer to reflect this nonlinearity. The effect of nonlinearity of base course is reduced as the elastic modulus of surface course increases [10], [23].

The model with consideration of dynamic analysis, viscoelasticity and nonlinearity, and temperature gradient lies along field data whereas simple model assumption produces high errors especially when the viscoelasticity of asphalt mixture was not considered [10].

As one of the powerful feature of FE program is that analysts can use user define material subroutines. With this subroutine, evaluation of interlayer is available which makes FE model much more realistic. There is a study which employs spring element (partial bond) and set different spring constants in different directions of axes [11]. The whole pavement structure is layered and is the layers are not fully (asphalt layers), or not bonded at all (granular layers). By using user define material models, modeling of this kind of partial boding condition is possible [5].

It is well known that a comprehensive analysis of flexible pavements should include the stress-dependent behavior of granular base course and the cohesive subgrade, finite width of the AC pavement, multiple wheel loading at any location of the given domain being analyzed, and partial bonding between the AC and the granular layer [5]. The challenge in the modeling of asphalt mixture contain the highly heterogeneous nature including aggregate internal structure and air void distribution, the time, temperature and rate-dependent behavior of the matrix and the limited computation capacity for very precise prediction [23].

A non-linear and time dependent analysis by FE method, literatures suggests to use a time depend materials. By taking step by step analysis the time dependent problem is solved. In this time interval, stress has to be constant and this interval has to be small enough. The viscoelastic pavement model; use the concept of simulating the partial bond condition between the asphalt and the base layer [11]. Time histories of strains or creep stiffness of creep tests are needed to simulate viscoelastic responses of asphalt material [14].

3.2 Mesh

The most time and effort consuming part is mesh generation in FE analysis. The mesh size is directly related to the accuracy of the results, and the cost of analysis. Fine mesh produces much more accurate result compared to coarse mesh but not always the finer mesh is adequate since there is a certain level that suits the accuracy and economy at the same time. Designers are intensively trying to find such level and build criteria for it.

Computed stress accuracy is related to mesh in vertical direction and deflection is related in horizontal direction mesh. Vertical extent of finite element mesh dominates convergence of stress [11]. The selection for the element sizes is based on the mesh convergence analysis.

The degree of mesh refinement is an important factor in estimating an accurate stress filed in the pavement. The mesh construction, mesh refinement, element aspect ratios and material non-linearity affect the overall time efficiency. For the three-dimensional problems, a careful balance is required to meet the demands of solution time and memory without sacrificing accuracy [13].

In the pavement analysis, mesh size determination is an important matter of fatigue crack analysis. Traffic flow is usually modeled as an axle fatigue load with equivalent fatigue damage. FE method is useful to determine the reference stress for fatigue life estimation and at the same time investigation of interaction between pavement and bridge deck [3]. So that it helps to decide the allowable stress level of pavement structure.

3.3 Load and boundary condition

Tire contact pressure is modeled as a uniformly distributed load in circular or rectangular area, see *Fig. 3*. The selection of analysis model is also one of the factor that influences on analysis result. Designers can choose between statistical analysis and dynamic analysis. Statistical analysis is economically effective and reliable but the dynamic analysis reflects much more realistic effect on model.

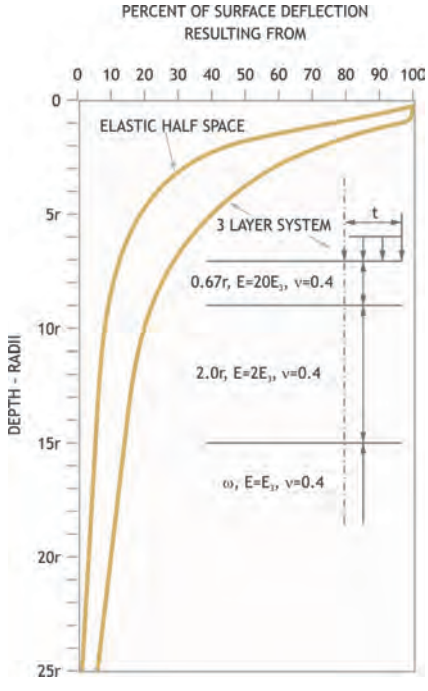

Fig. 3 Comparison of surface deflections of elastic half-space and layered system [6]
3. ábra A rugalmas féltérben és többrétegű rendszerben létrejövő behajlások összehasonlítása [6]

Most of cases tire pressure is modeled as a contact stress at the area where the tire is standing on pavement surface and is to be a distributed load on a contact area. The contact area can be modeled as a circular shape or rectangular shape, and in the case when contact is modeled in rectangular shape it is guided to have a dimension of BX0.7B. The moving tire can be embody as an imprint area to represent a smooth pavement surface [8], [9].

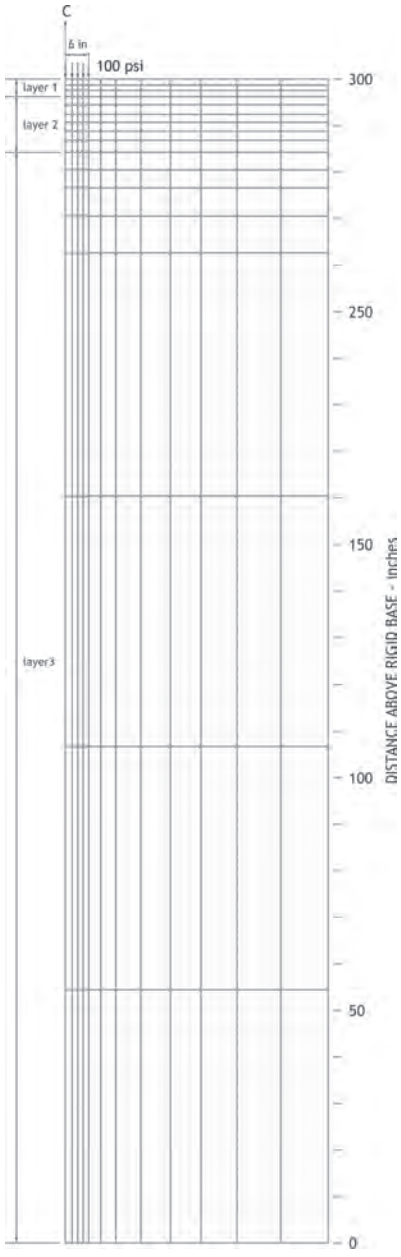

Fig. 4 Finite element configuration used for analysis of layered system-deep bottom boundary [6]
4. ábra A többrétegű rendszer elemzéséhez használt véges elemes összeállítás [6]

There are two types of thermal strains which are interesting in mechanistic design. One is thermal gradient and the other one is uniform thermal strains. The formal one happens because of the temperature change in a day, and the latter one is because of temperature change due to seasons. In the FE modeling, the thermal load can be modeled by applying gravity load in separate time step and propagate gravity load to get a thermal gradient profile [18], [17], [7], [16].

Hooke's linear elastic model is used for mechanistic analysis and design of asphalt pavement structures. It is considered to be appropriate for determination of response of asphalt layers at lower temperatures [19].

The rheological behavior directly connected to deterioration and determine the thickness of layers. Bituminous materials like asphalt mixture displays time dependent mechanical behavior. A Huet-Sayegh model, Eq. (3) describes response of bituminous material. This mathematical representation can simulates the behavior of asphalt mixes in cycling tests in wide frequency range [1]. This model reflect the time lag between stress and response due to the viscoelastic behavior of bituminous asphaltic material in pavement structure. Burger, Maxwell, and Kelvin models are included in mechanical model for viscous material as well, however they have constrain that they do not fully draw complex behavior of asphalt concrete. Whereas Huet-Sayegh model has shortcoming which does not reflect irreversible deformation properly compare to those models (*Fig. 5*).

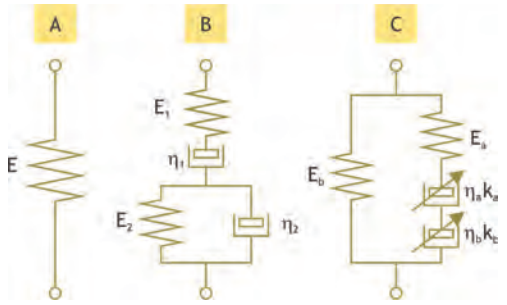

Fig. 5 Rheological models of the materials of asphalt layers: A) Hooke's elastic model, B) Burgers' viscoelastic model, C) Huet-Sayegh's viscoelastic model [15]
5. ábra Az aszfaltrétegek anyagainak reológiai modelljei: A) Hooke-féle rugalmas modell, B) Burgers-féle viszkoelasztikus modell, C) Huet-Sayegh-féle viszkoelasztikus modell [15]

To account for the variation in the modulus of elasticity with depth within a layer, the layer should be divided into several sublayers and the modulus should be gradually varied between the layers.

To numerically solve a boundary value problem that involves boundaries extending to infinity (e.g. subgrade), the domain must be truncated at a reasonable distance from the loads. For this reason, the size of the computational domain and the effects of the boundary conditions at the truncated remote boundaries has to be carefully studied [20], [11].

Subgrade layer is modeled to be infinite in vertical direction. Take into account the computation time and cost, the size of domain has to be determined. For the analysis of structure, set the proper boundary condition is crucial part in modeling. In 1968 there was a study which verified boundary condition that produces accurate results is to set fixed boundary at a depth about 50 radii and constrained from moving in radial direction about 12 radii from the center when the FE model is under circular distributed load [2].

A model which is large enough can avoid the boundary effect. To determine the domain size differs from designers and this step is comparison of structural responses when boundary position is 10 to 50 times from the center of symmetry. A research suggests a general criteria for circular distributed load, designers to use a domain 150 times bigger than loading radius [21].

3. Conclusions

This is a very short review about the concerns and choices when do the modeling with FE software. There are more and more demand for accurate analysis to save design cost and ensure structure integrity during its service life. Now the design trend is changing empirical method into Mechanistic-Empirical method for that purpose. Along with mechanistic-empirical analysis, various mechanical model is verified and applied in the FE method in a user define element command.

From the choice of proper material model to set proper mesh size and boundaries are all done by analyst in FE analysis. All of the stages in modeling process a series of selection is continued and it makes whole design process be dependent on analysts. These selection problems make modeling be difficult and complicated. To overcome, many researchers carry out a sensitivity tests to verify and choose which parameter is crucial and has impact on the response. In closure, there is a need to catch up the gap between numerical models which can overcome the complexity in real behavior due to mechanical interaction in each layers.

References

[1] AASHTO, (2008): Mechanistic-Empirical Pavement Design Guide. Washington DC: *American Association of State Highway and Transportation Officials*. ISBN; 978-1-56051-597-5

[2] ABAQUS, (2014): Standard user's guide. RI, USA.: *The Abaqus Software is a product of Dassault Systèmes Simulia Corp.*.

[3] Bohai, J. et al., (2013): Evaluation on root-deck fatigue of orthotropic steel bridge deck. *Journal of Construction Steel Research*, Volume 90, pp. 174-183. https://doi.org/10.1016/j.jcsr.2013.07.036

[4] Chen, D. H. – Zaman, M. – Laburos, J. – Soltani, A. (1995): Assessment of Computer Programs for Analysis of Flexible Pavement Structure, Washington D.C.: *Transportation Research Board of the National Academy of Sciences.*

[5] Chun, S. – Kim, K. – Greene, J. – Choubane, B. (2015): Evaluation of interlayer bonding condition on structural response characteristics of asphalt pavement using finite element analysis and full-scale field tests. *Construction and Building Materials*, Volume 96, pp. 307-318. https://doi.org/10.1016/j.conbuildmat.2015.08.031

[6] Duncan, M. J. – Monismith, C. L. – Wilson, E. L. (1968): Finite Element Analyses of Pavements. *Highway Research Record*, Volume 228, pp. 18-33.

[7] El-Maaty, A. E. A. – Hekal, G. M. – El-Din, E. M. (2016): Modeling of Dowel Jointed Rigid Airfield Pavement user Thermal Gradients and Dynamic Loads. *Civil Engineering Journal*, 2(2), pp. 38-51.

[8] Faheem, H. – Hassan, M. (2014): 2D plaxis finite element modeling of asphlalt concrete pavement reinforced with geogrid. *Journal of Engineering Sciences*, pp. 1336-1348.

[9] Gupta, A. – Kumar, A. (2014): Comparative structural analysis of flexible pavements using finite element method. *The International Journal of Pavement Engineering and Asphalt Technology*, pp. 11-19. https://doi.org/10.2478/ijpeat-2013-0005

[10] Hicks, R. G. – Monismith, C. L. (1971): Factors influencing the resilient response of granular materials. *Highway research record*, Volume 345. Record URL: http://onlinepubs.trb.org/Onlinepubs/hrr/1971/345/345-002.pdf

[11] Hjelmstad, D. K. – Kim, J. – Zuo, H. Q. (1997): Finite Element Procedures for Three-dimensional Pavement Analysis, Seatttle: ASCE.

[12] Hjelmstad, K. D. – Taciroglu, E. (1997): Coupled hyperelastic constitutive model for resilient response of granular materials. N.Y., *Proceedings of the Airfield Pavement Conference.*

[13] Kuo, C.-M. – Chou, F.-J. (2004): Development of 3-D Finite Element model for flexible pavements. *Journal of the Chinese Institute of Engineers,* 27(5), pp. 707-717. https://doi.org/10.1080/02533839.2004.9670918

[14] Li, M. – Wang, H. – Xu, G. – Xie, P. (2017): Finite element modeling and parametric analysis of viscoelastic and nonlinear pavement responses under dynamic FWD loading. *Construction and Building Materials,* Volume 141, pp. 23-35. https://doi.org/10.1016/j.conbuildmat.2017.02.096

[15] Mejłun, Ł. – Judycki, J. – Dołżycki, B. (2016): Comparison of elastic and viscoelastic analysis of asphalt pavement at high temperature. *Vilnius, Modern Building Materials, Structures and Techniques.* https://doi.org/10.1016/j.proeng.2017.02.095

[16] Pronk, A. C. (2005): The Huet-Sayegh model; A simple and excellent rheological model for master curves of asphalt mixes. *Louisiana, American Society of Civil Engineers*. https://doi.org/10.1061/40825(185)8

[17] Seed, B. H. – Mitry, G. F. – Monismith, C. L. – Chan, K. C., (1967): Prediction of flexible pavement deflections from laboratory repeated load tests, Washington D.C.: *Transportation Research Board*. Order URL: http://worldcat.org/issn/00775614

[18] Shayesteh, A. – Ghasemisalehabadi, E. – Khordehbinan, M. W. – Roastmi, T. (2017): Finite Element Method in Statistical Analysis of Flexible pavement. *Journal of Marine Science and Technology*, 25(2), pp. 142-15. 10.6119/JMST-016-0721-1

[19] Srikanth, R. M. (2015): Study on Analysis of Flexible Pavement using Finite Element based Software Tool. *International Journal of Engineering Research & Technology*, 4(9), pp. 912-916. https://doi.org/10.17577/ijertv4is090865

[20] Sukumaran, B. et al. (2004): Three dimensional Finite Element modeling of flexible pavements. Atlantic city, *FAA Worldwide airport technology transfer*. https://doi.org/10.1061/40776(155)7

[21] Szydłowski, C. – Górski, J. – Stienss, M. – Smakosz, Ł. (2018): Numerical simulation of asphalt mixtures fracture using continuum models. s.l., *AIP Conference Proceedings 1922*. https://doi.org/10.1063/1.5019142

[22] Uzan, J. (1985): Characterization of Granular Material, Washington D.C.: Transportation Research Record.

[23] Zhang, J. – Yang, J. (2013): Advances in micromechanical constitutive theories and modeling. *China, Procedia-Social and Behavioral Sciences* 96, pp. 1304-1314. https://doi.org/10.1016/j.sbspro.2013.08.148

Végeselem modellezés használata mechanikus pályaszerkezet-méretezéshez. Áttekintés: a modell felépítésétől az anyag valódi összetettségéig

A végeselem modellezést (VEM) számos tudományos területen alkalmazzák. A VEM a szerkezeti vizsgálatok területén rendkívül megalapozott, de az aszfaltburkolatú útpályaszerkezetek méretezése terén is egyre gyakrabban merül fel az alkalmazása, sőt, ahogy a szerkezet terhelésre adott reakcióinak becslése a pályaszerkezet-méretezés alapvető összetevője, a véges elemmel végzett precíz modellezések egyre fontosabbá válnak. A cikk a VEM pályaszerkezet-méretezés során való alkalmazásairól ad összefoglalást, az egyes szerkezeti rétegeknek a modellben való felépíthetőségére fókuszálva. A cikk célja emellett felhívni a figyelmet a VEM-ben rejlő lehetőségekre, miközben a VEM erősségei mellett rámutat annak gyengeségeire is.

Kulcsszavak: végeselem módszer, aszfaltburkolat modellezése, anyagmodell

Ref.:

Cho, Seoyoung – **Tóth,** Csaba – **Soós,** Zoltán: *Finite Element Method analysis for mechanistic design in flexible pavement, Review: From how to build a material in FE analysis to complexity in reality* Építőanyag – Journal of Silicate Based and Composite Materials, Vol. 70, No. 6 (2018), 204–208. p. https://doi.org/10.14382/epitoanyag-jsbcm.2018.35

Nanostructure and Surface Characteristic of Electrospun Carbon Black/PVDF Copolymer Nanocomposite

Muhamad NASIR ▪ Research Unit for Clean Technology, Indonesian Institute of Sciences (LIPI), Indonesia ▪ mnasir71@yahoo.com
Rana Ida SUGATRI ▪ Research Unit for Clean Technology, Indonesian Institute of Sciences (LIPI), Indonesia
Putri Putih Puspa ASRI ▪ Research Unit for Clean Technology, Indonesian Institute of Sciences (LIPI), Indonesia
Fitri DARA ▪ Research Unit for Clean Technology, Indonesian Institute of Sciences (LIPI), Indonesia
ARDENISWAN ▪ Research Unit for Clean Technology, Indonesian Institute of Sciences (LIPI), Indonesia

Érkezett: 2018. 07. 24. ▪ Received: 24. 07. 2018. ▪ https://doi.org/10.14382/epitoanyag-jsbcm.2018.36

Abstract

Carbon black/PVDF copolymer (CB/PVDF copolymer) nanofiber composite has been synthesized by electrospinning process. Nanostructure and surface property of CB/PVDF copolymer were studied by using Scanning Electron Microscopy (SEM), Fourier Transform Infrared Spectroscopy (FTIR), X-ray Diffraction (XRD) and water contact angle (WCA). Nanofiber composite has smooth surface morphology without bead on nanofiber string. Increase of CB content in nanofiber composite decreased diameter of nanofiber size. Range of average nanofiber diameter was from 405.2 and 421.3 nm where it depended on CB content in nanofiber composite. FTIR and XRD analysis showed that structure of PVDF copolymer in nanofiber composite had a dominant β phase crystal structure. The β phase was showed and confirmed by vibration band peak at 838.55 cm^{-1} of IR spectrum and $2\theta = 20.44°$ of XRD. Presence of CB in nanofiber composite also influenced WCA and water spreading on nanofiber composite. WCA of pristine PVDF copolymer, CB/PVDF copolymer nanofiber with 1% CB, and CB/PVDF copolymer with 5% CB were 113.8, 105.2, 117.3°. From this result showed that nanostructure and surface characteristic can be adjusted and controlled by presence of CB in nanofiber composite. This result has potential application for air filtration to solve air pollution issued.

Keywords: CB/PVDF copolymer nanofiber composite, carbon black, nanostructure, electrospinning, water contact angle of nanofiber composite
Kulcsszavak: CB/PVDF kopolimer nanoszál kompozit, szén fekete, nanoszerkezet, elektroszálképzés, víz nedvesítési szöge nanoszál kompoziton

Dr. Eng. Muhamad NASIR
He has research interest in nanomaterials and nanoengineering fields especially in nanofiber, nanoparticle such metal, metal oxide, and nanocarbon, nanocomposite, electrospinning and membrane process for various applications. He finished his PhD in Tokyo Institute of Technology, Japan. After that he took postdoctoral in Kyoto Institute of Technology, Japan. Now he is head of environmental nanotechnology research group in Research Unit for Clean Technology, Indonesian Institute of Sciences (LIPI).

Rana Ida SUGATRI
She obtained her bachelor's degree from University of Jenderal Achmad Yani, Indonesia in 2016. She is currently a research assistant under the supervision of Dr. Eng. Muhamad Nasir at Research Unit for Clean Technology, Indonesian Institute of Sciences. She joined in a team that focuses on the development of nanofiber and nanoparticle as main materials to solve environmental problems. In the laboratory, she showed interests in a synthesis nanofiber using electrospinning process and their application as membrane filtration

Putri Putih Puspa ASRI
She received her bachelor degree in chemistry from Jenderal Achmad Yani University, Cimahi, Indonesia In 2016. She worked as Research Assistant and was doing some research related to nanotechnology topic under supervision of Dr. Eng. Muhamad Nasir. Her research interests are synthesis, nanomaterial composite for battery application, thermal and spectroscopy characterization for nanomaterial composite, and nanomaterial for green and sustainable technology.

Dr. Fitri DARA
Researcher at Research Unit for Clean Technology, Indonesian Institute of Sciences. She finished her Doctoral Programme in 2017 from Chemistry Department, Institut Teknologi Bandung, Indonesia. Her research interest is qualitatively and quantitatively assess Nanoparticle (NP) under environmentally relevant conditions, reflecting amongst others not only realistic NP concentrations, environmental conditions but also reaction and residence times..

ARDENISWAN
He received his master degree in environmental engineering, Bandung Institute of Technology. His research interest is in the field of hazardous waste and environmental monitoring such as air and water pollution.

1. Introduction

Nanofiber, fabricated by electrospinning, has great potential to be used in many environmental applications. The main advantage of this process is the relative quick and simple way to fabricate a variety of materials into nanofiber structure [1]. Besides, the high surface-to-volume ratio, large porosity (up to over 80%) and adjustable functionality are more effective than conventional non-woven and polymeric membranes in particulate separation and liquid filtration [2].

Poly(vinylidene fluoride) (PVDF) nanofiber and poly(vinylidene) fluoride copolymer are the polymer materials which easily synthesized by electrospinning process. Excellent resistance towards harsh chemicals, piezoelectricity, flexibility, durability, lightweight, and relatively low acoustic impedance properties [3-5] considered PVDF nanofiber to be used in some applications such as membrane separator of secondary Li-ion battery [6-8], supercapacitor [9-10], sensing element [11-13] and air filtration [14-16].

PVDF has dipole moments due to the polar C-F bond which distribute along the fiber axis. It causes the electrostatic attractive forces integrate along the length of the fiber segments. This integration strengthens the electric field projected from the fibers [15, 17]. The electric charge which takes place between filter media and dust particles makes PVDF nanofiber is capable for capturing particles (charged and uncharged aerosols) effectively in air filtration application [14-16, 18-19]. The fibers with small diameter enhance the van der Walls attractive force between nanofiber and particle [14] then trap particles among the polymer matrix [16].

The unique electrospinning process offers opportunities to fine tune the surface functionality through polymer chemistry,

blending and nanofiller incorporation during the process [2]. New approaches in a modification of nanofiber were reported by many researchers which have been incorporating nanoparticle in solution polymer system for fabricating nanofiber composite.

It has been over one decade that carbon black (CB) nanoparticle became one of the interesting materials to modify polymer nanofiber due to small particle size (high surface area), aggregation behavior, low cost and conductive property [20-21] Those properties make CB has usability as an adsorbent material [22]. *Islam* et al [23] reported that CB is the most effective adsorbent material than extruded activated carbon and granular activated carbon. In nanofiber system, the presence of CB in polyurethane (PU) [20] and polyaniline (PANI) [24] nanofiber composite increased the fiber web strength and electrical conductivity. However, it decreased significantly when CB incorporated in PEO system [25].

As much as we know that no other researchers reported the effect of incorporating CB in pristine PVDF copolymer solution to synthesize nanofiber using electrospinning. In this work, we used some variation of the amount of CB which incorporated into PVDF copolymer to produce nanofiber composite. We concerned in basic concept including effect of the filler content on the fiber morphology, the bond structure of the nanofiber composite, the crystallinity and the hydrophilicity. These results will support usability of CB/PVDF copolymer nanofiber composite to improve PVDF nanofiber function as air filtration. We suggested this nanofiber composite not only trap particulate matter, but also adsorb chemical pollutant in the air. Increasing the web strength and electrical conductivity of CB/PVDF copolymer nanofiber composite are expected can improve their ability to trap particulate matter more easily.

2. Experimental

2.1 Materials

Poly(vinylidene fluoride) (PVDF) copolymer which was used in this work is poly(vinylidene fluoride-co-hexafluoropropene) (PVDF-HFP). It was purchased from Arkema Inc. U.S.A. The *N,N*-dimethylacemide (DMAc) from Merck was used as solvent for preparation of polymer solution. Carbon black (Dashblack HAF N330) was obtained from OCI Company Ltd. and used as nanoparticle which incorporated into polymer solution.

2.2 Nanofiber preparation

A 24% (w/v) cPVDF solution was prepared by dissolving 2.4 g cPVDF powder in 10 mL DMAc. It was stirred at room temperature for 5 h. CB was added to the cPVDF solution with variation concentration 0, 1, and 5% (w/v) for pristine PVDF, CB1/PVDF copolymer and CB5/PVDF copolymer, respectively, then stirred for 12 h. The composite solution was spun into nanofiber using electrospinning with parameters 22 kV, 13 cm, and 0.004 mL/min for 2 h.

2.3 Characterization

Surface morphology of nanofiber was analyzed by Scanning Electron Microscopy (SEM) SEMSU3500. Fourier Transform Infrared Spectroscopy (FTIR) Nicolet iS5 ATR iD5 Thermo Scientific was used for analysis of interaction between PVDF and carbon black in nanofiber composite. Crystallinity between pristine PVDF nanofiber and its composite was analyzed by XRD Shimadzu 7000. Water contact angle was measured by drop shape method and calculated by the equation:

$\frac{\theta}{2} = \tan^{-1}(\frac{h}{d})$ with θ = contact angle, d = diameter, h = height.

3. Results and discussion

3.1 Morphological characteristics and fiber diameters

Incorporated CB into PVDF copolymer nanofiber system gives effect onto morphology and diameter of nanofiber. The amount of CB was added into polymer solution is 0, 1, and 5% (w/v). *Fig. 1* shows that pristine and composite of nanofibers have smooth morphology without bead on nanofiber string. Increase of CB content in CB/PVDF copolymer nanofiber composite results decreasing diameter of nanofiber. Diameter of pristine PVDF copolymer nanofiber is 599.5 nm then changes to 405.2 and 421.3 nm after adding carbon black 1 and 5% (w/v), respectively. The diameter of CB/PVDF copolymer nanofiber composite tends to decrease was caused by the tendency of CB to absorb the solvent. Evaporation of solvent in composite polymer solution can be slower than pristine polymer during the fiber formation [20, 26]. Besides, the conductivity of CB in composite polymer solution also caused diameter of CB/PVDF copolymer nanofiber is smaller than pristine PVDF copolymer [27-28]. In CB5/PVDF copolymer composite nanofiber, the diameter is larger than CB1/PVDF copolymer. It suggested the amount of CB 5% (w/v) attributed to form agglomeration of nanoparticle. The agglomeration of CB is apparent on the fiber surface clearly, see *Fig. 1.c.*

3.2 Infrared spectrum

The bond structure and interaction between CB and PVDF copolymer in nanofiber composite is shown by *Fig. 2.*

In the IR spectrum of PVDF copolymer, crystalline β phase peak at 839.23 cm^{-1} indicated rocking vibration of CH_2 group. The presence of CB in composite nanofiber caused shifting peak at 838.55 and 834.62 cm^{-1} for CB1/PVDF copolymer and CB5/PVDF copolymer, respectively. The CF_2 symmetrical stretching was shown at 1400.27, 1175.09, and 1072.76 cm^{-1}. Incorporated CB in CB/PVDF copolymer nanofiber composite caused shifting peak at CF_2 function group such as 1399.30, 1171, and 1071.99 cm^{-1} for CB1/PVDF copolymer and 1396.61, 1164.68, and 1062.16 cm^{-1} for CB5/PVDF copolymer. The 1274.58 cm^{-1} is a peak for CF stretching vibration. Decreasing band intensity at about 1274 cm^{-1} in CB/PVDF copolymer can be caused by interaction between function group of CB and CF of PVDF. The 876.81 cm^{-1} is identical for CH_2 of PVDF. It shifted to 875.71 and 871.17 after added CB 1 and 5% (w/v), respectively. Band peaks at around 1160-900 cm^{-1} and 800-600 cm^{-1} of CB/PVDF copolymer nanofiber composite are broader than pristine PVDF copolymer nanofiber due to dominant effect from increasing amount of CB in nanofiber composite. The C≡C bonding and CH_3-O- at 2114.04 and 993.36 cm^{-1} are characteristics of CB function groups.

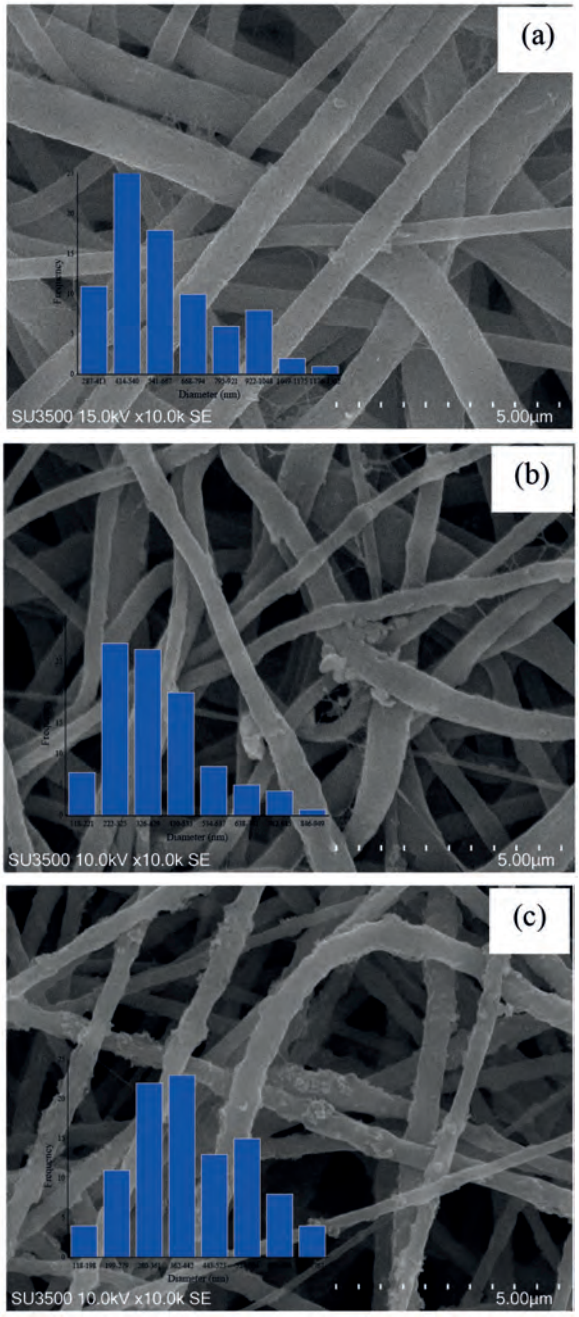

Fig. 1 SEM images of CB/PVDF copolymer nanofiber with various amount of CB (a) pristine PVDF copolymer, (b) 1% (w/v) and (c) 5% (w/v)

1. ábra Elektronmikroszkópos felvételek; CB/PVDF kopolimer nanoszál különböző CB adagolással (a) kiindulási PVDF kopolimer, (b) 1% (w/v) és (c) 5% (w/v)

3.3 Crystallinity

X-ray diffraction (XRD) pattern confirms the existence and effect of CB in nanofiber composite. *Fig. 3* shows characteristic peak at 2θ = 20.44° for pristine PVDF copolymer nanofiber, 20.06° for CB1/PVDF copolymer and 20.88° for CB5/PVDF copolymer. Those peaks show strong peak of piezoelectric crystal β-phase structure of PVDF copolymer. The CB which incorporated in PVDF copolymer nanofiber gives effect on crystallinity of composite. CB acts as the nucleation agent in polymer matrix which affecting the crystallization process in the formation of PVDF copolymer nanofiber [29].

Incorporating CB in PVDF copolymer nanofiber decreases the crystallinity. The pristine PVDF copolymer nanofiber has 49.84% and decreases to 42.73 and 48.49% for adding CB 1 and 5% (w/v), respectively. The crystalline structure of the CB/PVDF copolymer may arise from the cooperative orientation of the CB and PVDF copolymer chains along the fiber axis to facilitate the nucleation of highly oriented chains crystallites at the interface [30]. The amount and type of nanoparticle can result difference crystallinity [29-31].

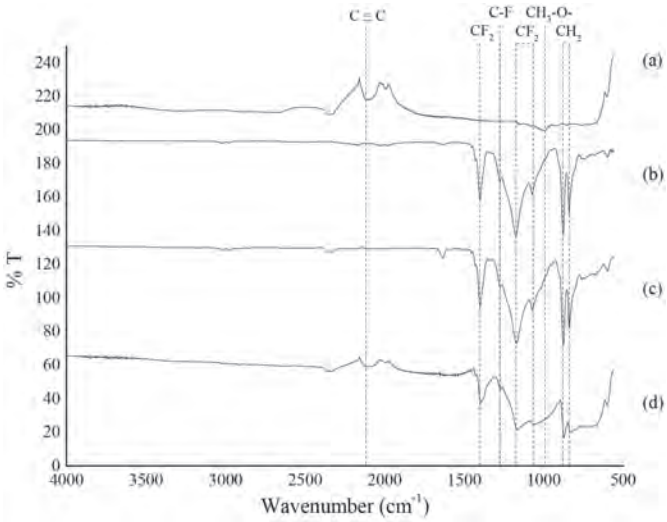

Fig. 2 FTIR spectrum of CB/PVDF copolymer nanofiber composite (a) CB nanoparticle, (b) pristine PVDF copolymer, (c) CB1/PVDF copolymer, and (d) CB5/PVDF copolymer

2. ábra FTIR spektrumok; CB/PVDF kopolimer nanoszál kompozit (a) CB nanorészecske, (b) kiindulási PVDF kopolimer, (c) CB1/PVDF kopolimer, és (d) CB5/PVDF kopolimer

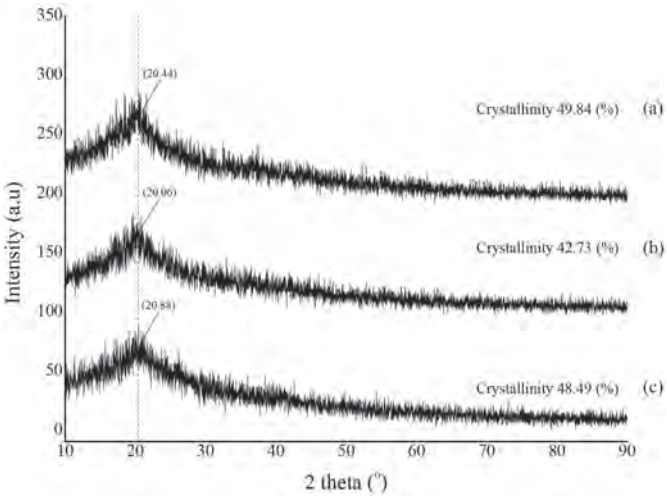

Fig. 3 XRD spectrum of nanofiber composite (a) pristine PVDF copolymer, (b) CB1/PVDF copolymer, and (c) CB5/PVDF copolymer

3. ábra Kompozit nanoszál röntgendiffraktogramok (a) kiindulási PVDF kopolimer, (b) CB1/PVDF kopolimer, és (c) CB5/PVDF kopolimer

3.4 Hydrophobicity

The hydrophobicity of the nanofiber is analyzed by its value of water contact angle. The amount of CB which incorporated in CB/PVDF copolymer nanofiber composite gives effect to contact angle value. Pristine PVDF copolymer nanofiber has 113.8° then decreases to 105.2 for CB1/PVDF copolymer, but increases to 117.3° for CB5/PVDF copolymer.

Many pores of CB have ability to absorb liquid matter. In *Figs. 1* and *5*, CB incorporated well inside of CB1/PVDF copolymer nanofiber. When water droplet contacted with surface nanofiber, it is not only interacts with C-F of PVDF copolymer but also with function groups and pores of CB. It suggested contact angle value of water droplet is smaller than pristine PVDF copolymer nanofiber. Unlike CB5/PVDF copolymer, CB made formation of agglomeration and apparent on surface of nanofiber. In this case, the surface roughness plays a role in the formation of higher contact angle.

Fig. 4 shows the spreading time of water droplet on CB/PVDF copolymer composite nanofiber. After 130 and 240 minutes, water droplet on CB5/PVDF copolymer composite nanofiber is faster to spread than pristine PVDF copolymer and CB1/PVDF copolymer regularly. In that time, water droplet has contacted with CB surface then CB can easily absorb water.

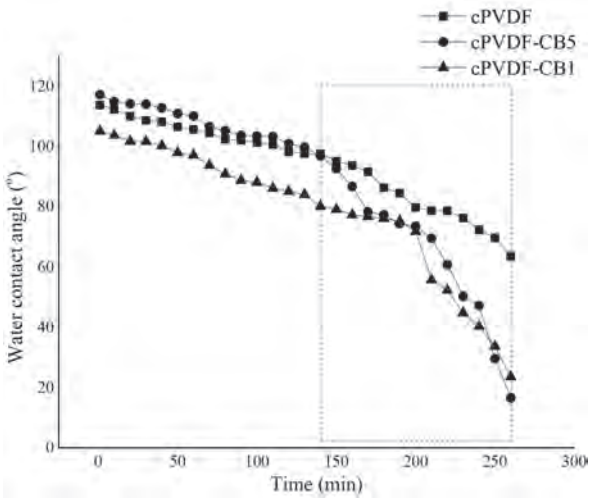

Fig. 4 The spreading time of water droplet on CB/PVDF copolymer nanofiber composite
4. ábra Vízcsepp terjedési ideje CB/PVDF kopolimer nanoszál kompoziton

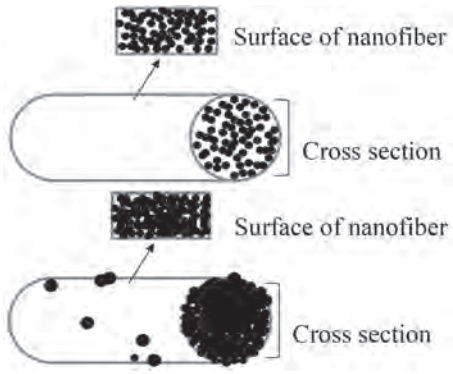

Fig. 5 Illustration of CB incorporated in CB/PVDF copolymer nanofiber composite
5. ábra CB elegyedésének illusztrációja CB/PVDF kopolimer nanoszál kompozittal

4. Conclusions

PVDF copolymer nanofiber composite was successfully synthesized by electrospinning which incorporating CB into solution system. These results clearly demonstrate that CB has significant effect on nanostructure and surface characteristic. Their morphology showed that the presence of CB in PVDF copolymer nanofiber system decreases diameter of nanofiber nanocomposite. In 5% (w/v) of CB in nanofiber composite, the agglomeration of nanoparticle is apparent in surface of nanofiber. Interaction between CB and PVDF was showed by shifting peak at CF_2 and CH_2 function groups and making band be broader than pristine PVDF copolymer. IR and XRD data confirm a dominant of β phase crystal structure of PVDF copolymer. The presence of CB in nanofiber composite also decreases their crystallinity. Besides, the hydrophobicity of CB/PVDF copolymer nanofiber composite changes to 105.2° and 117.3° for adding 1 and 5% (w/v) CB content, respectively, from 113.8° of pristine PVDF copolymer. After 130 and 240 minutes, CB5/PVDF copolymer nanofiber composite is faster to spread than pristine PVDF copolymer and CB1/PVDF copolymer.

References

[1] Faccini, M. – Vaquero, C. – Amantia, D. (2012): Development of Protective Clothing against Nanoparticle Based on Electrospun Nanofibers, *Journal of Nanomaterials*, Vol. 2012, Article ID 892894, pp 1-9. https://doi.org/10.1155/2012/892894

[2] Yoon, K. – Hsiao, B. S. – Chu, B. (2008): Functional Nanofibers for Environmental Applications, *Journal of Materials Chemistry*, Vol. 18, pp 5326-5334. https://doi.org/10.1039/b804128h

[3] Kawai, H. (1969): The Piezoelectricity of Poly(Vinylidene Fluoride), *Japanese Journal Applied Physics*, Vol. 8, pp 975-976. http://doi.org/10.1143/JJAP.8.975

[4] Rao, S. S. – Sunar, M. (1994): Piezoelectricity and Its Use in Disturbance Sensing and Control of Flexible Structures: A Survey, *Applied Mechanics Reviews*, Vol. 47, pp 113-123. https://doi.org/10.1115/1.3111074

[5] Sheikh, F. A. – Zargar, M. A. – Tamboli, A. H. – Kim, H. (2016): A Super Hydrophilic Modification of Poly(Vinylidene Fluoride) (PVDF) Nanofibers: By In Situ Hydrothermal Approach, *Applied Surface Science*, Vol. 385, pp 417-425. https://doi.org/10.1016/j.apsusc.2016.05.111

[6] Choi, S. S. – Lee, Y. S. – Joo, C. W. – Lee, S. G. – Park, J. K. – Han, K. S. (2004): Electrospun PVDF Nanofiber Web as Polymer Electrolyte or Separator, *Electrochimica Acta*, Vol. 50, pp 339-343. https://doi.org/10.1016/j.electacta.2004.03.057

[7] Hwang, K. – Kwon, B. – Byun, H. (2011): Preparation of PVDF Nanofiber Membranes by Electrospinning and Their Use as Secondary Battery Separators, *Journal of Membrane Science*, Vol. 378, pp 111-116. https://doi.org/10.1016/j.memsci.2011.06.005

[8] Widiyandari, H. – Purwanto, A. – Widyanto, S. A. (2017): Polyvinilidine Fluoride (PVDF) Nanofiber Membrane for Li-Ion Rechargeable Battery Separator, *Jurnal of Physics: Conference Series*, Vol. 817, 012013, pp 1-6. https://doi.org/10.1088/1742-6596/817/1/012013

[9] Zhu, Z. – Tang, S. – Yuan, J. – Qin, X. – Deng, Y. – Qu, R. – Haarberg, G. M. (2016): Effects of Various Binders on Supercapacitor Performances, *International Journal of Electrochemical Science*, Vol. 11, pp 8270-8279. https://doi.org/10.20964/2016.10.04

[10] He, T. – Jia, R. – Lang, X. – Wu X. – Wang, Y. (2017): Preparation and Electrochemical Performance of PVDF Ultrafine Porous Fiber Separator-Cum-Electrolyte for Supercapacitor, *Journal of The Electrochemical Society*, Vol. 164, pp E379-E384. https://doi.org/10.1149/2.0631713jes

[11] Zampetti, W. – Bearzotti, A. – Macagnano, A. (2014): Flexible Piezoelectric Transducer Based on Electrospun PVDF Nanofibers for Sensing Applications, *Procedia Engineering*, Vol. 87, pp 1509-1512. https://doi.org/10.1016/j.proeng.2014.11.585

[12] Sengupta, D. – Kottapalli, A. G. P. – Chen, S. H. – Miao, J. M. – Kwok, C. Y. – Triantafyllou, M. S. – Warkiani, M. E. – Asadnia, M. (2017): Characterization of Single Polyvinylidene Fluoride (PVDF) Nanofiber for Flow Sensing Applications, *American Institute of Physics Advances*, Vol. 7, 105205, pp 1-7. https://doi.org/10.1063/1.4994968

[13] Parker, A. – Ueda, A. – Marvinney C. E. – Hagrove, S. K. – Williamns, F. – Mu, R. (2018): Structural and Thermal Treatment Evaluation of Electrospun PVDF Nanofibers for Sensors, *Journal of Polymer Science and Applications*, Vol. 2, 1000109, p 1-4.

[14] Li, Z. – Kang, W. – Zhao, H. – Hu, M. – Ju, J. – Deng, N. – Cheng, B. (2016): Fabrication of A Polyvinylidene Fluoride Tree-Like Nanofiber Web for Ultra High Performance Air Filtration, *Royal Society of Chemistry Advances*, Vol. 6, pp 91243-91249. https://doi.org/10.1039/C6RA17097H

[15] Lolla, D. – Lolla, M. – Abutaleb, A. – Shin, H. U. – Reneker, D. H. – Chase, G. G. (2016): Fabrication, Polarization of Electrospun Polyvinylidene Fluoride Electret Fibers and Effect on Capturing Nanoscale Solid Aerosols, *Materials*, Vol. 9, 671, pp 1-17. https://doi.org/10.3390/ma9080671

[16] Wang, L. Y. – Yong, W. F. – Yu, L. E. – Chung, T. S. (2017): Design of High Efficiency PVDF-PEG Hollow Fibers for Air Filtration of Ultrafine Particles, *Journal of Membrane Sciences*, Vol. 535, pp 342-349. https://doi.org/10.1016/j.memsci.2017.04.053

[17] Dargaville, R. – Celina, M. C. – Elliott, J. M. – Chaplya, P. M. – Jones, G. D. – Mowery, D. M. – Assink, R. A. – Clought, R. L. – Martin, J. W. (2005): Characterization, Performance and Optimization of PVDF as A Piezoelectric Film for Advanced Space Mirror Concepts, *The United States Department of Energy, Sanda Corporation: Sandia National Laboratories, Sandia Report* SAND2005-6846

[18] Matsumoto, H. – Tanioka, A. (2011): Functionality in Electrospun Nanofibrous Membranes Based on Fiber's Size, *Surface Area, and Molecular Orientation, Membranes*, Vol. 1, pp 249-264. https://doi.org/10.3390/membranes1030249

[19] Cho, D. – Naydich, A. – Frey, M. W. – Joo, Y. L. (2013): Further Improvement of Air Filtration Efficiency of Cellulose Filters Coated with Nanofibers via Inclusion of Electrostatically Active Nanoparticles, *Polymer*, Vol. 54, pp 2364-2372. https://doi.org/10.1016/j.polymer.2013.02.034

[20] Hwang, J. – Muth, J. – Ghosh, T. (2007): Electrical and Mechanical Properties of Carbon-Black-Filled, Electrospun Nanocomposite Fiber Webs, *Journal of Applied Polymer Science*, Vol. 104, pp 2410-2417. https://doi.org/10.1002/app.25914

[21] Tarasova, E. – Byzova, A. – Savest, N. – Viirsalu, M. – Gudkova, V. – Martson, T. – Krumme, A. (2015): Influence of Preparation Process on Morphology and Conductivity of Carbon Black-Based Electrospun Nanofibers, *Fullerenes, Nanotubes and Carbon Nanostructures*, Vol. 23, pp 695-700. https://doi.org/10.1080/1536383X.2014.974090

[22] Shah, J. – Jan, M. R. – Mabood, F. – Shahid, M. (2006): Conversion of Waste Tyres Into Carbon Black and Their Utilization as Adsorbent, *Journal of the Chinese Chemical Society*, Vol. 53, pp 1085-1089. https://doi.org/10.1002/jccs.200600144

[23] Islam, A. K. M. M. – Hwang, J. I. – Lee, S. E. – Kim, J. E. (2016): Comparative Study of Carbon Black and Activated Carbon Adsorbents for Removal of Carbofuran from Aqueous Solution, *Desalination and Water Treatment*, Vol. 57, pp 1-12. https://doi.org/10.1080/19443994.2015.1124053

[24] Kalluri, S. – Asha, A. M. – Parvathy, S. – Kim, T. N. – Sivakumar, N. – Subramanian, K. R. V. – Nair, S. V. – Balakrishnan, A. (2013): Electrospun Nanofibers of Polyaniline-Carbon Black Composite for Conductive Electrode Applications, *Trends in Polyaniline Research: Chapter 8*, Nova Science Publishers, Inc

[25] Li, W. K. – Wong, Y. W. (2009): Electrical Properties of Electrospun Nanofibers of PEO/Carbon Black Composite, *Solid State Phenomena*, Vol. 151, pp 67-71. https://doi.org/10.4028/www.scientific.net/SSP.151.67

[26] Lawandy, S. N. – Wassef, M. T. (1990): Penetration of Oils Into Polychloroprene Rubber, *Journal of Applied Polymer Science*, Vol. 40, pp 323-331. https://doi.org/10.1002/app.1990.070400302

[27] Razzaz, A. – Ghorban, S. – Hosyani, L. – Irani, M. – Aliabadi, M. (2016): Chitosan Nanofibers Functionalized by TiO_2 Nanoparticles for The Removal of Heavy Metal Ions, *Journal of the Taiwan Institute of Chemical Engineers*, Vol. 58, pp 333-343. https://doi.org/10.1016/j.jtice.2015.06.003

[28] Nasikhudin Diantoro, M. – Kusumaatmaja, A. – Triyana, K. (2016): Preparation of PVA/Chitosan/TiO_2 Nanofibers Using Electrospinning Method, *AIP Conference Proceedings*, Vol. 1755, 150002, pp 1-6. https://doi.org/10.1063/1.4958575

[29] Moradi, R. – Sabet, J. K. – Niassar, M. S. – Koochaki, M. A. (2015): Preparation and Characterization of Polyvinylidene Fluoride/Graphene Superhydrophobic Fibrous Films, *Polymers*, Vol. 7, pp 1444-1462. https://doi.org/10.3390/polym7081444

[30] Huang, S. – Yee, W. A. – Tjiu, W. C. – Liu, Y. – Kotaki, M. – Boey, Y. C. F. – Ma, J. – Liu, T. – Lu, X. (2008): Electrospinning of Polyvinylidene Difluoride with Carbon Nanotubes: Synergistic Effects of Extensional Force and Interfacial Interaction on Crystalline Structures, *Langmuir*, Vol. 24, pp 13621-13626. https://doi.org/10.1021/la8024183

[31] Liu, Z. H. – Pan, C. T. – Lin, L. W. – Lai, H. W. (2013): Piezoelectric Properties of PVDF/MWCNT Nanofiber Using Near-Field Electrospinning, *Sensors and Actuators A: Physical*, Vol. 193, pp 13-24. https://doi.org/10.1016/j.sna.2013.01.007

Ref.:
Nasir, Muhamad – **Sugatri,** Rana Ida – **Asri,** Putri Putih Puspa – **Dara,** Fitri – **Ardeniswan**: *Nanostructure and Surface Characteristic of Electrospun Carbon Black/PVDF Copolymer Nanocomposite*
Építőanyag – Journal of Silicate Based and Composite Materials, Vol. 70, No. 6 (2018), 209–213. p.
https://doi.org/10.14382/epitoanyag-jsbcm.2018.36

GUIDELINE FOR AUTHORS

The manuscript must contain the followings: title; author's name, workplace, e-mail address; abstract, keywords; main text; acknowledgement (optional)**; references; figures, photos with notes; tables with notes; short biography** (information on the scientific works of the authors).

The full manuscript should not be more than 6 pages including figures, photos and tables. Settings of the word document are: 3 cm margin up and down, 2,5 cm margin left and right. Paper size: A4. Letter size 10 pt, type: Times New Roman. Lines: simple, justified.

TITLE, AUTHOR

The title of the article should be short and objective.

Under the title the name of the author(s), workplace, e-mail address.

If the text originally was a presentation or poster at a conference, it should be marked.

ABSTRACT, KEYWORDS

The abstract is a short summary of the manuscript, about a half page size. The author should give keywords to the text, which are the most important elements of the article.

MAIN TEXT

Contains: materials and experimental procedure (or something similar), results and discussion (or something similar), conclusions.

REFERENCES

References are marked with numbers, e.g. [6], and a bibliography is made by the reference's order. References should be provided together with the DOI if available.

Examples:

Journals:

[6] Mohamed, K. R. – El-Rashidy, Z. M. – Salama, A. A.: In vitro properties of nano-hydroxyapatite/chitosan biocomposites. *Ceramics International.* 37(8), December 2011, pp. 3265–3271, http://doi.org/10.1016/j.ceramint.2011.05.121

Books:

[6] Mehta, P. K. – Monteiro, P. J. M.: Concrete. Microstructure, properties, and materials. *McGraw-Hill*, 2006, 659 p.

FIGURES, TABLES

All drawings, diagrams and photos are figures. The **text should contain references to all figures and tables**. This shows the place of the figure in the text. Please send all the figures in attached files, and not as a part of the text. **All figures and tables should have a title**.

Authors are asked to submit color figures by submission. Black and white figures are suggested to be avoided, however, acceptable.

The figures should be: tiff, jpg or eps files, 300 dpi at least, photos are 600 dpi at least.

BIOGRAPHY

Max. 500 character size professional biography of the author(s).

CHECKING

The editing board checks the articles and informs the authors about suggested modifications. Since the author is responsible for the content of the article, the author is not liable to accept them.

CONTACT

Please send the manuscript in electronic format to the following e-mail address: femgomze@uni-miskolc.hu and epitoanyag@szte.org.hu or by post: Scientific Society of the Silicate Industry, Budapest, Bécsi út 122–124., H-1034, HUNGARY

We kindly ask the authors to give their e-mail address and phone number on behalf of the quick conciliation.

Építőanyag – *Journal of Silicate Based and Composite Materials*, Quarterly peer-reviewed periodical of the Hungarian Scientific Society of the Silicate Industry, SZTE.
http://epitoanyag.org.hu

EAGE

INCLUDING SPE International EUROPEC

EMBRACING CHANGE -
CREATIVITY FOR THE FUTURE

The EAGE Annual 2019, the 81st Conference & Exhibition, is the largest and most comprehensive multi-disciplinary geoscience event in the world. The event includes a large conference – in total over 1,000 technical oral and e-Poster presentations – and a technical exhibition presenting the latest developments in geophysics, geology and reservoir/petroleum engineering. More than 7,000 people from almost 100 different countries visit this event annually.

2019 EAGE ANNUAL

81ST CONFERENCE + EXHIBITION

LONDON | THE UNITED KINGDOM

3-6 JUNE 2019

WWW.EAGEANNUAL2019.ORG

European Society for Biomaterials

European Society for Biomaterials

Biomaterials are gaining importance in the development of the new treatments for many clinical applications.

The future of innovation in the field of medical devices and regenerative medicine depends on the deep understanding of the mechanisms of interaction between biomaterials and the host biological environment.

New chemistry and material engineering will need to emerge to produce biocompatible, bioactive, bioresponsive biomaterials.

The European Society for Biomaterials offers a multidisciplinary environment where scientific knowledge is promoted and technological solutions can be found.

www.esbiomaterials.eu